The effect of microalloying elements on Mg-Zn alloys

Tilak Bhattacharjee

June 2014

The effect of microalloying elements on Mg-Zn alloys

Tilak Bhattacharjee

Doctoral Program in Materials Science and Engineering

Submitted to the Graduate School of

Pure and Applied Sciences

in Partial Fulfillment of the Requirements

for the Degree of Doctor of Philosophy in Engineering

at the

University of Tsukuba

Acknowledgements

The work in this thesis was performed throughout the doctoral course at the University of Tsukuba under the joint program between National Institute for Materials Science and University of Tsukuba.

First and foremost, I would like to express my sincerest appreciation to Professor Kazuhiro Hono for suggesting this investigation and constant guidance in the course of the work.

I am immensely grateful to Dr. Chamini Lakshi Mendis, Dr. Taisuke Sasaki and Dr. Tadakatsu Ohkubo for helping me to learn the techniques of scanning electron microscopy, transmission electron microscopy and atom probe tomography and their useful advices and encouragement.

I am very thankful to Professor Shigeharu Kamado and Mr. Taiki Nakata at Nagaoka University of Technology for extrusion experiments.

I am also thankful to Professor Nack Joon Kim and Dr. Byeong-Chan Suh at POSTECH for providing the twin-roll cast hot rolled Mg-Zn alloys.

I would also like to profoundly thank the Graduate Research Assistantship of National Institute for Materials Science which provided financial assistance during the course of candidature.

I would like to express my humble gratitude to all the members of the Magnetic Materials Unit of National Institute for Materials Science for their support during the course.

Finally, to my family and friends for their support and encouragement during the course of the study.

Table of contents

Chapter 1. Introduction and literature review

1.1. History

The etymology of the name magnesium comes from the Greek word “Magnesia” based on the name of a district in Thessaly, ancient Greece. The element magnesium was first identified in 1755 by Joseph Black when he performed calcination of Magnesia Alba (presently known as magnesium carbonate) [1]. In 1808, Sir Humphrey Davy isolated magnesium for the first time by electrolysis of magnesium sulphate [2]. Later, Frenchman Antoine Bussy isolated magnesium metal by fusing dehydrated magnesium chloride with potassium at high temperatures. In 1852, a German scientist, Robert-Wilhelm Bunsen was successful in producing metallic magnesium through his newly developed carbon-zinc electric cell. Bunsen also used fused and dehydrated magnesium chloride as the starting material to produce magnesium [2]. Magnesium was initially used in its powdered form or in ribbon form for flashlights and pyrotechnical purposes. It also found use as a reducing agent in the aluminium metal industry. The demand for magnesium grew in the period of World War I for its use as a structural metal for military purposes. Before 1915, Germany was the only source of magnesium but due to World War I seven magnesium plants were built in United States (US) [3]. After the war, the production declined as many of the companies left the business, barring few such as Dow. After 1928 Dow was the only magnesium producing company in US till World War II. During World War II Germany not only expanded their old magnesium plants but also built new ones in Austria and Norway. In the US fifteen new magnesium plants were built during 1941-1943 [3]. Magnesium was used in airplanes for military purpose such as the Northrop XP-56 and the B36 Bomber which contained around 8700 kg of magnesium [2]. The US production capacity for magnesium reached its peak which was around 184,000 tons in 1943. Then there was a decline in magnesium production after the end of the war and it became only 5,300 tons in 1946 [3]. Recent years have seen renewed interest in magnesium in the automobile industry due to the need for reducing global warming by improving fuel efficiency of automobiles.

1.2. Properties

Magnesium is the lightest of the presently used structural metals having the density of 1.74 g/cm^3 which is around 2/3 rd that of aluminium and 1/4 th that of steel. This makes magnesium alloys one of the most sought after alloys to be used in the transportation sector, such as automobiles, trains and aircraft, where it has potential to replace the currently used structural metals such as steel, aluminium for further weight reduction of vehicles. The following are the some of the physical properties of pure magnesium.

1.2.1 Atomic properties

Magnesium has an atomic number of 12 in the periodic table of elements. It has isotopes with mass number 24, 25, 26 which occur naturally in the proportions of around 7:1:1. Thus, the atomic weight of magnesium is around 24.32. The electronic configuration of magnesium is $1s^2 2s^2 2p^6 3s^2$ [4]

1.2.2 Structural properties

Magnesium has a hexagonal crystal structure consisting of alternating ABAB close-packed layers (Fig.1). The lattice parameters are a= 3.2 A° and c= 5. 21A° and has a c/a ratio of 1.624.

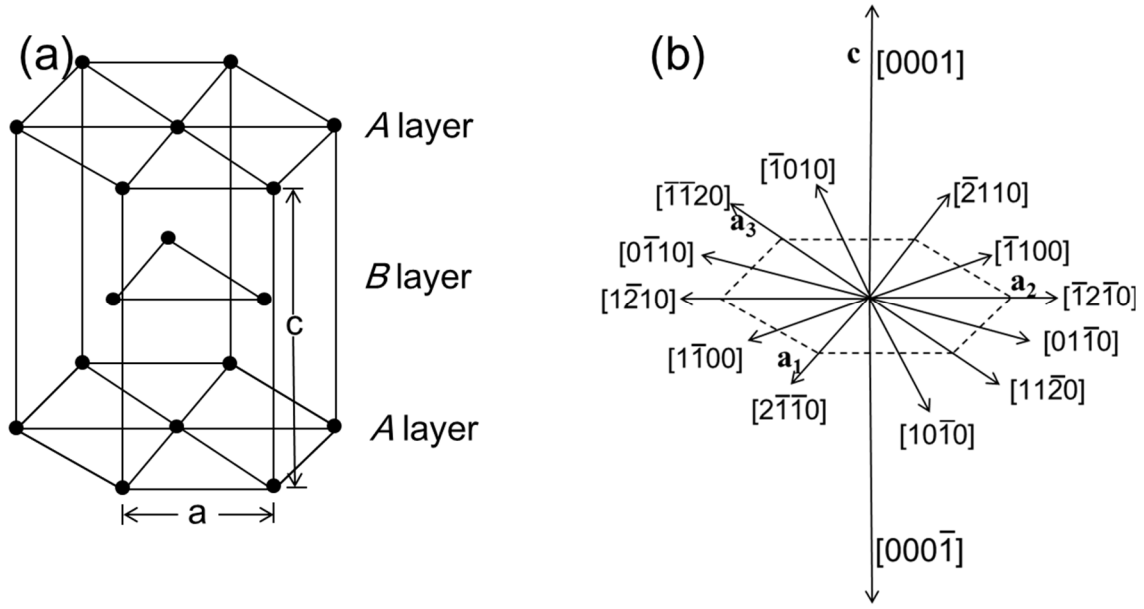

Figure 1: (a) crystal structure of magnesium (b) principal directions.

1.2.3 Deformation behavior

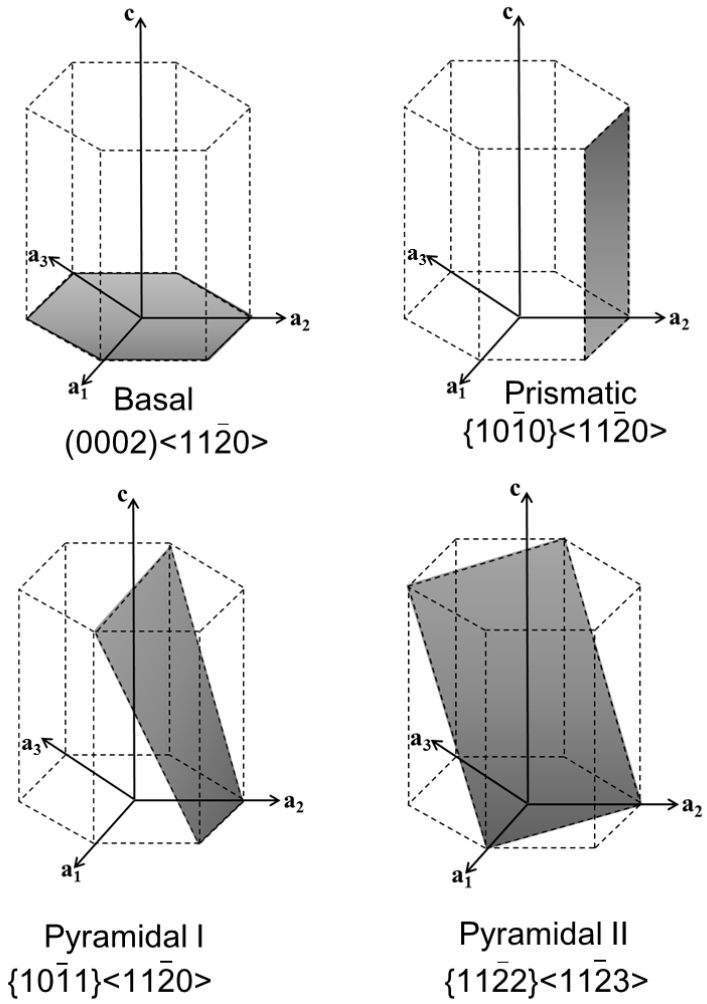

Figure 2. Deformation modes in hcp Mg: basal, prismatic and pyramidal slip systems.

Magnesium has 3 basal (0001)<11$\bar{2}$0>slip systems operating at room temperature. Since five independent slip systems are required at room temperature for homogeneous deformation as per the Von Mises or Taylor criterion additional deformation mechanisms such as twinning occur to accommodate the strain [references from book]. At higher temperatures, prismatic slip system such as {10$\bar{1}$0}<11$\bar{2}$0> and pyramidal slip system such as {10$\bar{1}$1}<11$\bar{2}$0> also takes place in magnesium. This is because at higher temperatures the critical resolved shear stress for non-basal systems becomes lower.

The three types of twinning which are observed in magnesium are as follows:

(a) Extension twinning:

This occurs commonly along the {10$\bar{1}$2}<10$\bar{1}$1> slip system. Since it results in an extension along the

c-axis in magnesium these twins are also called “tension twins”. The basal plane in the twin gets reoriented through 86.3 º as shown in Fig. 3(a).

(b) Contraction (or compression) twinning:

This type twin commonly occurs along the $\{10\bar{1}1\}<10\bar{1}2>$ and results in an contraction of the c-axis of magnesium. The basal planes gets rotated by 56.2 º along the $<11\bar{2}0>$ direction as shown in Fig. 3(b).

(c) Double-twinning

This type of twin takes place when a primary twin undergoes secondary twinning within the primary twins. Double twinning generally occurs when a primary $\{10\bar{1}1\}$ or $\{10\bar{1}3\}$- compression twin undergoes a secondary $\{10\bar{1}2\}$- tension twinning and produces a rotation about the same $<11\bar{2}0>$ direction. The most commonly observed $\{10\bar{1}1\}$-$\{10\bar{1}2\}$ double twinning results in a rotation of ~38 º of the basal planes from their original position as shown in Fig. 3(c). The $\{10\bar{1}3\}$-$\{10\bar{1}2\}$ results in a basal plane rotation of 22 º.

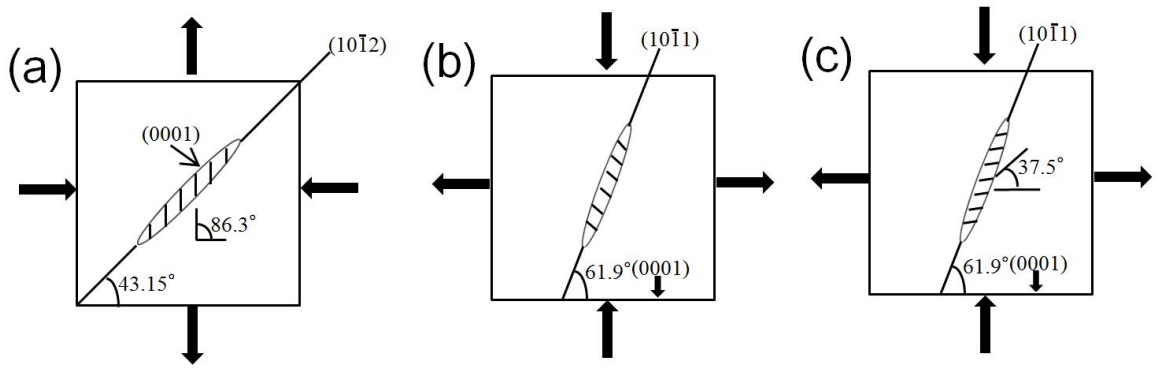

Figure 3. (a) Extension twinning on **(**$10\bar{1}2$); (b) Compression twinning on **(**$10\bar{1}1$); (c) Retwinning on **(**$10\bar{1}2$) after compression twin on **(**$10\bar{1}1$) [5]

1.3. Production process of magnesium

Magnesium is generally found in their combined form in the ores such as magnesite ($MgCO_3$) , dolomite ($MgCO_3.CaCO_3$), seawater ($MgCl_2$,$MgSO_4$), carnallite ($MgCl_2.KCl.6H_2O$) and serpentine ($3MgO.2SiO_2.2H_2O$). Some of the processes used for magnesium metal production as described below:

1.3.1 Pidgeon process: This process is based on silicothermic reduction of magnesium oxide [6]. A

schematic flow chart for the this process is shown in Fig. 4.

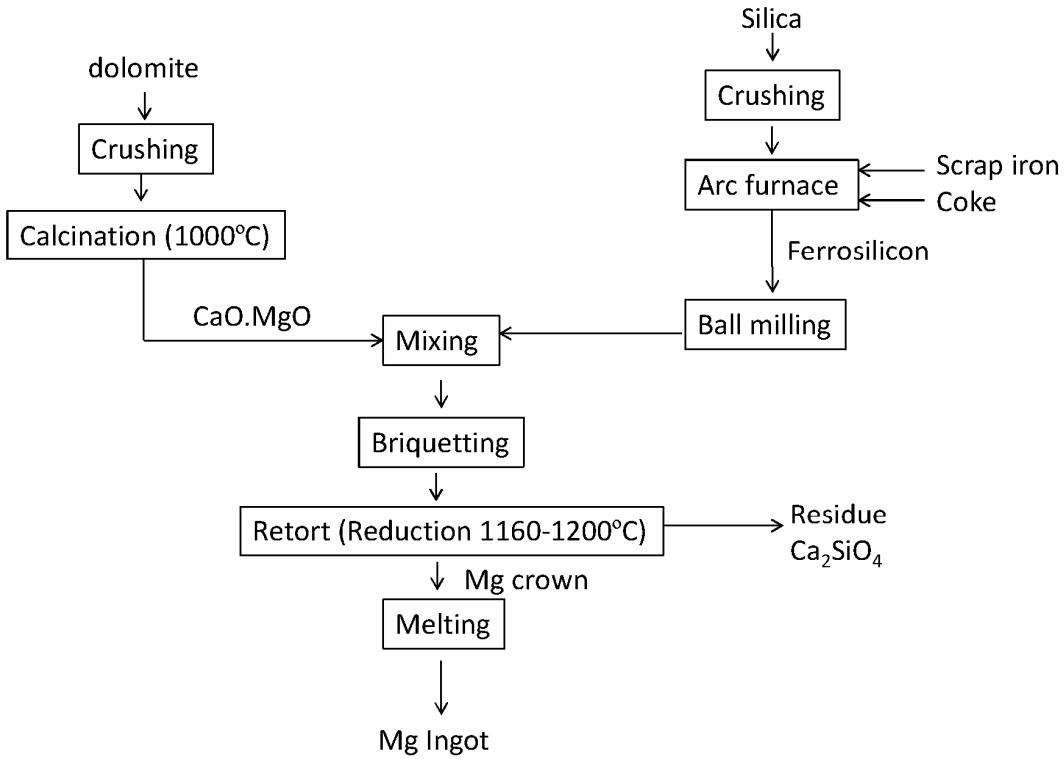

Figure 4. Schematic flowsheet of the Pidgeon process [7]

Firstly the calcination of dolomite ($MgCO_3.CaCO_3$) is done in a rotary kiln at 1000 to 1300ºC to get a mixture of MgO and CaO. The reduction of the above mixture of CaO and MgO is done by ferrosilicon. The ferrosilicon is produced by the carbothermic reaction of quartz sand, coke and iron oxide using an electric arc furnace at around 1600°C. After that the calcined dolomite and ferrosilicon are mixed and briquetted and then placed in horizontal stainless steel retorts. Then the retorts are heated to temperatures around 1160°C and pressures around 13-67Pa. The reduction of calcined dolomite by ferrosilicon produces magnesium vapour given by the equation given below [8]:

$$2\ CaO.MgO(s) + (x\ Fe)\ Si(s) \longrightarrow 2\ Mg(s) + 2\ Ca_2SiO_4(s)$$

This process is vastly used in China for the production for magnesium metal although it has drawbacks such as it causes lot of pollution due to CO_2 emissions during calcination of dolomite and is energy/labor intensive.

1.3.2 Electrolytic process

The electrolytic process involves reduction of magnesium chloride ($MgCl_2$) in an electrolytic cell. The initial procedure involves chlorination of magnesium oxide (MgO). The chlorination is done by heating the MgO mixed with carbon in a stream of chlorine at a high temperature in an electric furnace. After this step the dehydration of aqueous magnesium chloride is done before transferring it to the electrolytic cell. Electrolysis of magnesium chloride is then done at temperatures around 700 to 800°C inside brick-lined vessels. The following electrolytic reaction occurs at the cathode and anode of the electrolytic cell [8]:

Cathode: $Mg^{2+} + 2e^- \longrightarrow Mg(l)$ $E^o = -2.38$ V

Anode: $2\ Cl^- \longrightarrow Cl_2(g) + 2e^-$ $E^o = 1.36$ V

1.4. Magnesium alloys

Magnesium metal is generally alloyed to improve mechanical properties of pure magnesium such as its tensile strength, creep resistance properties, formability etc., depending upon its application. The mechanical properties of unalloyed magnesium from reference [9] are shown in Table 1.

Table 1: Mechanical properties of unalloyed magnesium [9]

Form and section	0.2% tensile yield strength (MPa)	Ultimate tensile strength (MPa)	0.2% compressive yield strength (MPa)	Elongation in 50mm (%)
Sand cast	21	90	21	2-6
Extruded	69-105	165-205	34-55	5-8
Hard rolled sheet	115-140	180-220	105-115	2-10
Annealed sheet	90-105	160-195	69-83	3-15

From Table 1 we can see that tensile yield strength of unalloyed magnesium is low, thus alloying is done to increase the mechanical properties to be used for structural applications. Although standard international system for designating magnesium alloys does not exist there has been a trend of adopting the naming method used by American Society for Testing and Materials (ASTM) [9]. This method has a three-part

letter-number-letter sequence. The first part consists of code letters indicating the principal alloying elements. The code letters generally used are listed in Table 2. The second part indicates the weight percentages of the alloying elements. The third part may have letters such as A, B, C etc. which indicates the variation in composition within the specified range. The letter X indicates that the alloy is experimental. The heat-treated conditions or tempers of the alloys are shown in Table 3.

Table 2: Code letters system used for magnesium alloys designation

Letter	Alloying element	Letter	Alloying element
A	Aluminium	N	Nickel
B	Bismuth	P	Lead
C	Copper	Q	Silver
D	Cadmium	R	Chromium
E	Rare earth metals	S	Silicon
F	Iron	T	Tin
H	Thorium	W	Yttrium
J	Strontium	X	Calcium
K	Zirconium	Y	Antimony
L	Lithium	Z	Zinc
M	Manganese		

Table 3: The temper designation used for magnesium alloys [9]

Letter	Temper
F	As fabricated
O	Annealed, recrystallized (wrought products only)
H	Strain hardened
T4	Solution heat treated
T5	Artificially aged
T6	Solution heat treated and artificially aged

1.5. Strengthening mechanisms

In order to develop high strength formable Mg alloys which could be used for structural applications, the combined effect of a number of different strengthening mechanisms have to be considered. These could include strengthening mechanisms such as:

1. grain size strengthening
2. solid solution strengthening
3. precipitation hardening

Brief descriptions of the above mechanisms are as follows:

(a) Grain size strengthening

The strengthening due to grain size is defined by the Hall-Petch relationship, $\sigma = \sigma_0 + kd^{-1/2}$, where σ is yield strength of the material, σ_0 is materials constant for the starting stress for dislocation movement, k is the Hall-Petch coefficient and d is the average grain size of the material [10]. As per the above Hall-Petch relation when there is a decrease in the grain size there is an increase in the strength of the alloy. The Hall–Petch coefficient for magnesium was reported to be around 0.7 MPa $m^{-1/2}$ for coarse grains (30–87 μm) and 0.13 MPa $m^{-1/2}$ for fine grains (17–30μm) [11]. These are significantly higher than the Hall–Petch

coefficient for aluminum alloys (0.07 MPa $m^{-1/2}$) [12]. Thus the grain size strengthening can be more effective for magnesium alloys compared to aluminium alloys. Grain size refinement can be achieved through processes such as chemical inoculation, wrought processing (rolling, extrusion, equal channel angular pressing, high pressure torsion, etc.) and also by controlling solidification rate. In magnesium alloys Zr is added as a grain refiner for obtaining small grain size distribution. SiC particles have also been reported to refine grain size of AZ31 magnesium alloy [13].

(b) Solid solution strengthening

This method relies on the solute elements present in the metal matrix which forms either substitutional or interstitial solid solution to strengthen the metal. The solute atoms vary in size, stiffness and electric charge from the solvent atoms. Due to these differences the randomly distributed solute atoms interact with dislocations impeding their motion. A larger mismatch or higher concentration of solute would induce larger strain field interactions between dislocations and solute atoms and hence would be more effective in strengthening the alloy. The solid solution strengthening contribution can be evaluated by the following equation $\sigma_{ss} = CX^{2/3}$ where X is the atomic fraction of solute concentration and C=197(MPa $X^{2/3}$) [14].

(c) Precipitation hardening

Precipitation hardening, also called age hardening relies on changes in solid solubility at different temperatures in order to produce fine sized particles (precipitates). These precipitates impede the dislocation movement and thus contribute to strengthen the alloy. The precipitation hardening method is briefly explained below with the help of Figure 5.

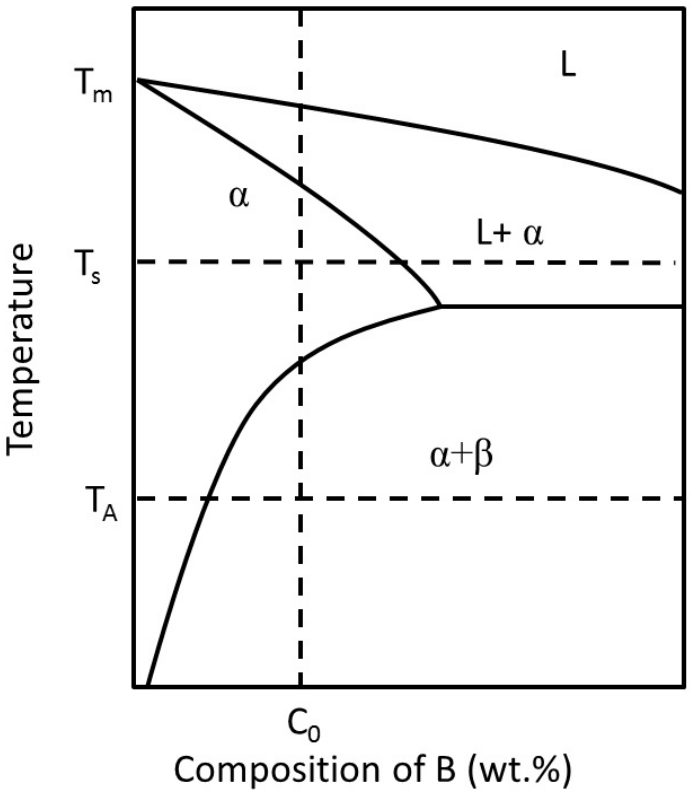

Figure 5. Schematic of a precipitation hardenable system.

In Figure 5 the temperatures T_A, T_s, T_m represent aging temperature, solution treatment temperature and melting temperature of element A. C_0 represents the chosen alloy composition. To age harden an alloy it is first solution treated to temperature T_s to get into the single phase region, α. Then the alloy is rapidly cooled by quenching into cold water. Finally the alloy is kept at a suitable temperature $<T_s$ in the two phase region for a given time (aging). During aging the supersaturated solid solution α transforms into an equilibrium mixture of $\alpha+\beta$ due to high driving force which comes from the supersaturation giving rise to fine precipitates inside the grains of the alloy and thereby increasing the strength of the alloy.

The mechanisms associated with precipitation hardening are shearing of precipitates by dislocations as well as looping of precipitates by dislocation (Orowan looping). The cutting stress of the precipitates tends to increase with aging time. When the precipitates are far apart dislocations bow between the particles. Upon aging the precipitate spacing tends to increase from 10 nm to 1 μm and beyond [15].

The stress increment due to the bowing of dislocations between precipitates can be approximated by

$$\sigma_{orowan} = \frac{MGb}{2\pi\sqrt{1-\nu}}\frac{1}{\lambda}\ln\left(\frac{d_A}{r_0}\right)$$

where M is the Taylor factor; G is the shear modulus of the matrix; b is the Burgers vector of the dislocation; ν is Poisson's ratio; λ and d_A are, respectively, the mean spacing and mean diameter of particles in the slip plane; and r_o is the inner cut-off radius of the dislocation taken equal to b [16].

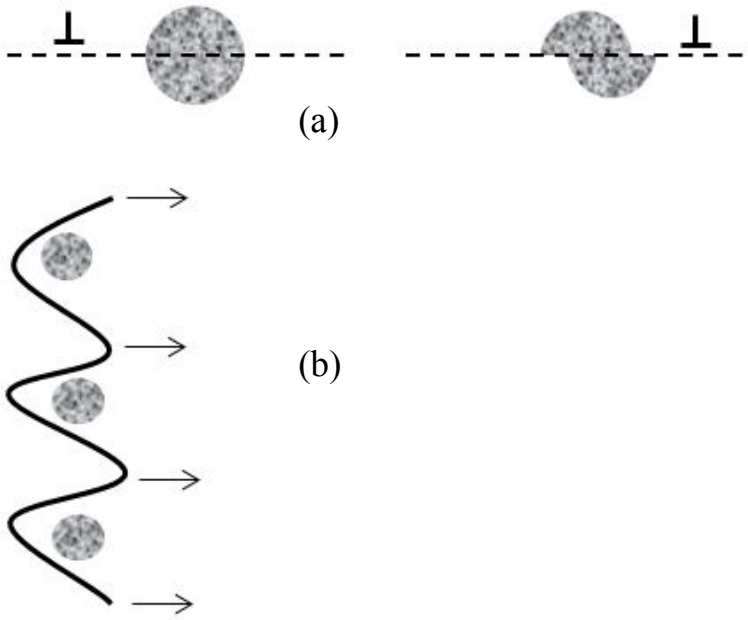

Figure 6. (a) cutting of precipitate by dislocation (b) bowing of dislocation between precipitates.

The precipitate shape and orientation also plays a major role in increasing the strength of a precipitation hardened alloy. For magnesium alloys containing precipitates that are resistant to dislocation shearing, Nie predicted that high strength is associated with a microstructure that have an high density of strong plate shaped precipitates with prismatic habit planes and large aspect ratios [17]. The relationship between effective inter-particle spacing, λ and precipitate number density are shown in Figure 7, showing that the most effective precipitates in lowering λ and increasing the critical resolved shear stress of magnesium alloys are the prismatic plates against basal slip.

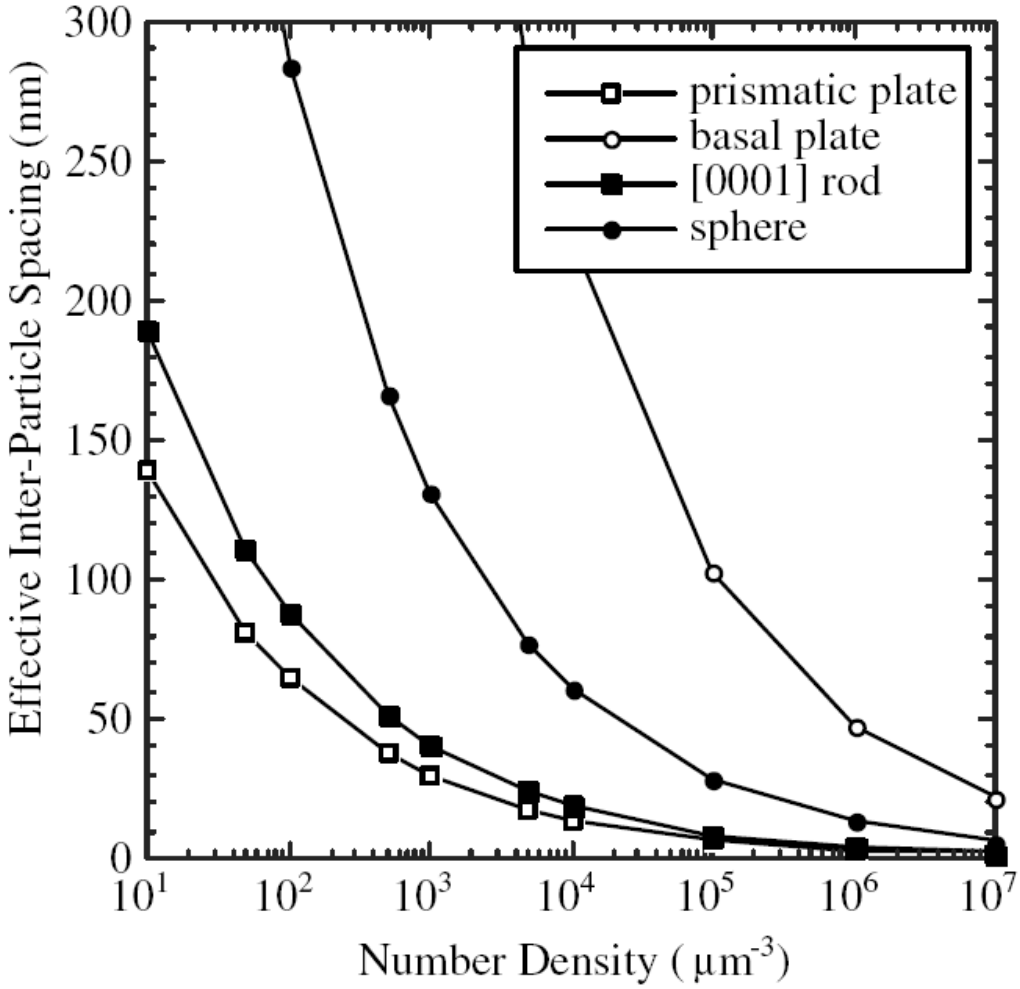

Figure 7. Comparsion of effective inter-particle spacing with number density of precipitates per volume in the magnesium matrix at a precipitate volume fraction of 0.04 for different shaped precipitates [17].

A similar study by Robson et al has also reported from their calculations that basal plates are poor strengtheners and prismatic plates are best strengtheners against basal slip [18]. Furthermore their calculations for prismatic slip suggest that c-axis rods provide the most strengthening as shown in Fig. 8.

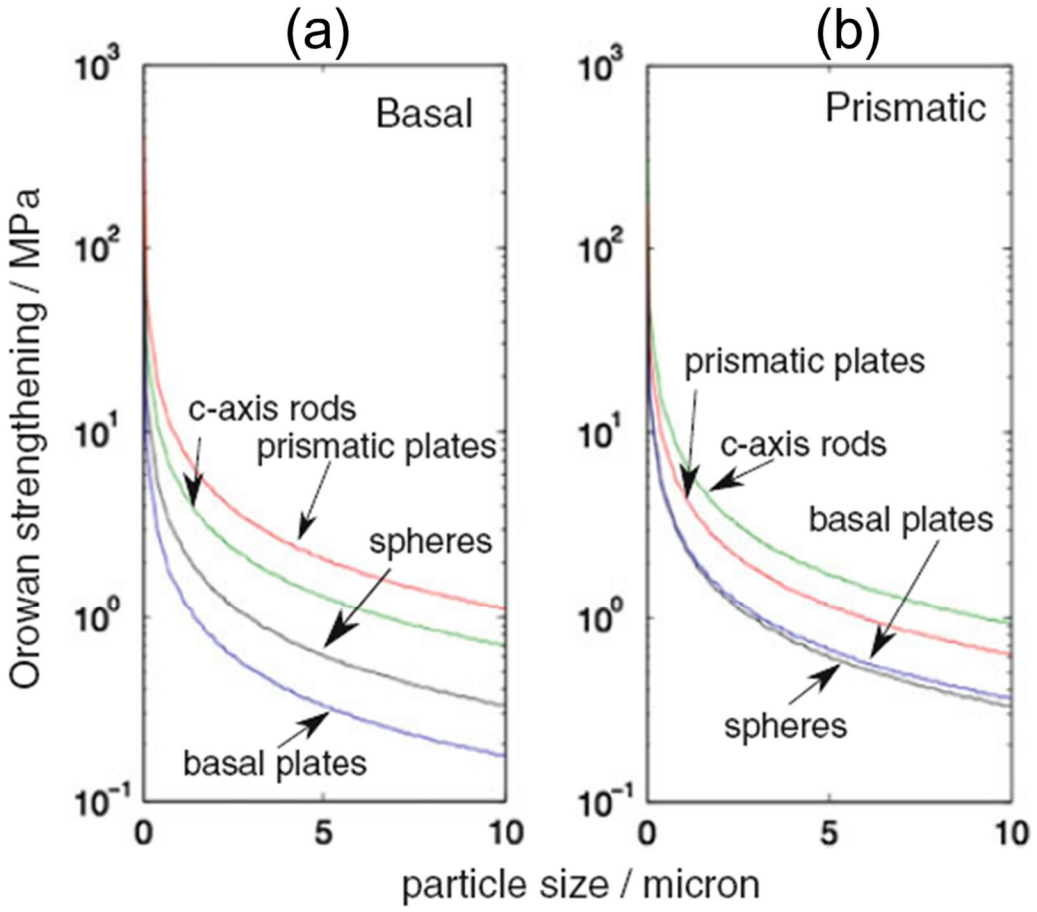

Figure 8. Calculation of the Orowan stress required to bypass basal plates, prismatic plates, c-axis rods and spherical precipitates for a) basal slip b) prismatic slip (particle volume fraction =5%, aspect ratio =0.10 for plates /10 for rods)[18]

1.6. Alloy system

In this section a literature review of the alloy systems related to the present research work are briefly described.

1.6.1 Mg-Zn alloy

The binary phase diagram of Mg-Zn system is shown in Fig. 9. The eutectic temperature is ~340ºC. The maximum solubility at the eutectic temperature is 6.2 wt.% (or 2.4 at.%). The solubility decreases to ~0.3 at.% Zn at room temperature. This makes this system a potent age hardenable system. The G.P. zones solvus for the Mg–5.5wt.%Zn alloy tends to lie between 70 and 80 °C [19], and pre-aging below this solvus results

in formation of G.P. zones prior to formation of $\beta'_1(MgZn_2)$ and $\beta'_2(MgZn_2)$ metastable precipitates. This is a metastable phase formed during isothermal aging and is not an equilibrium phase. The reported equilibrium phase is a MgZn phase with rhombohedral crystal structure and lattice parameters of a=2.55 nm and c=1.81 nm [20]. The metastable β'_1 and β'_2 have a hexagonal crystal structure with lattice parameters of a=5.2 A° and c=8.5A° [21-23]. The β'_1 have a rod shape and grows along the [0001] direction of the magnesium matrix and β'_2 have a plate-like morphology and lies along (0001) plane of the magnesium matrix as shown schematically in Fig. 10.

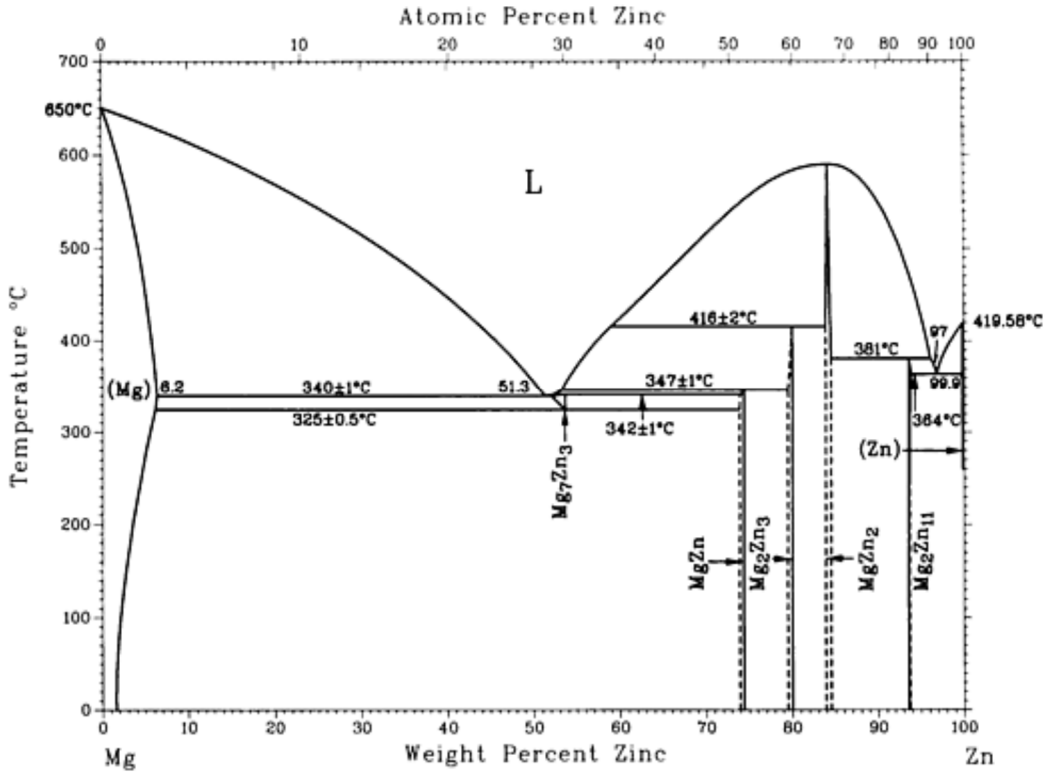

Figure 9. Binary phase diagram of the Mg-Zn system [24].

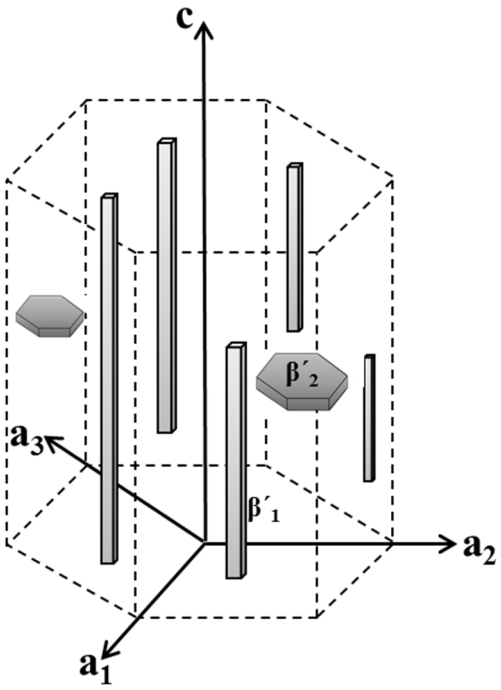

Figure 10. Schematic representation of β'_1 and β'_2 precipitates of Mg-Zn system.

The age hardening response of Mg-Zn alloy during isothermal aging for a temperature range from 50°C-185°C is shown in Fig. 11. For all the temperatures initially there is an incubation period followed by rapid increase in hardness. The incubation period decreases with increasing aging temperature. After reaching peak hardness there is a slight decrease in the hardness. The hardening response of Mg-Zn has shown improvement by trace addition of Au [25], Ca [26] and combined additions of Ag and Ca [27].

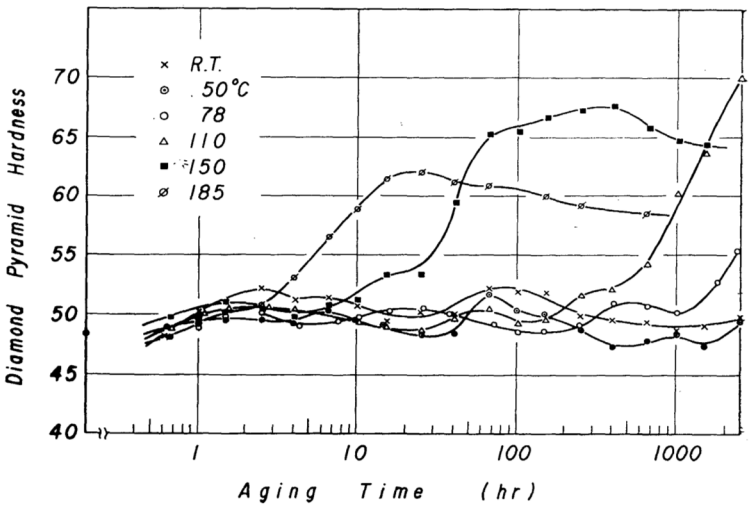

Figure 11. Age hardening curves of Mg-Zn aged in the temperature range 50-185°C [28].

1.6.2 Mg-Zr alloy

The binary phase diagram of Mg-Zr system is shown in Fig. 12 and the Mg-rich corner of the Mg-Zr system is shown in Fig. 13.

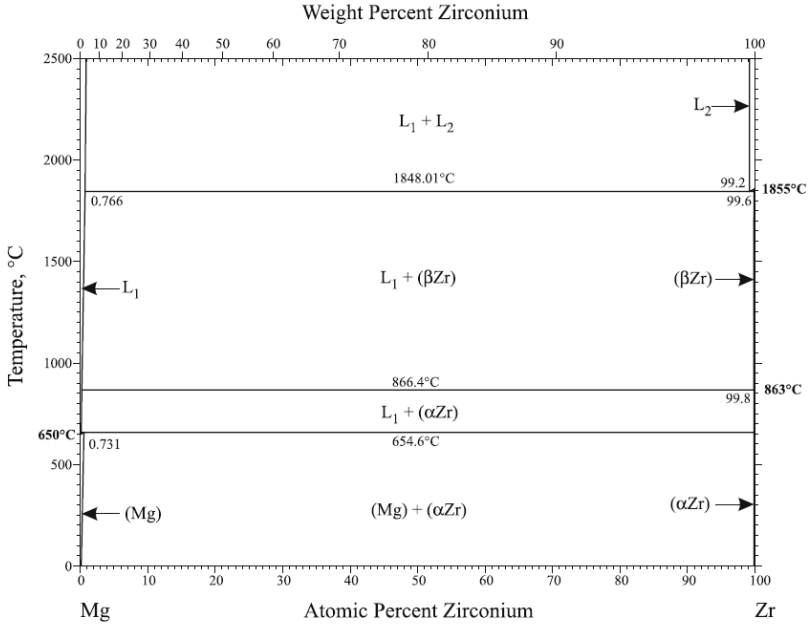

Figure 12. Binary phase diagram of the Mg-Zr system [29].

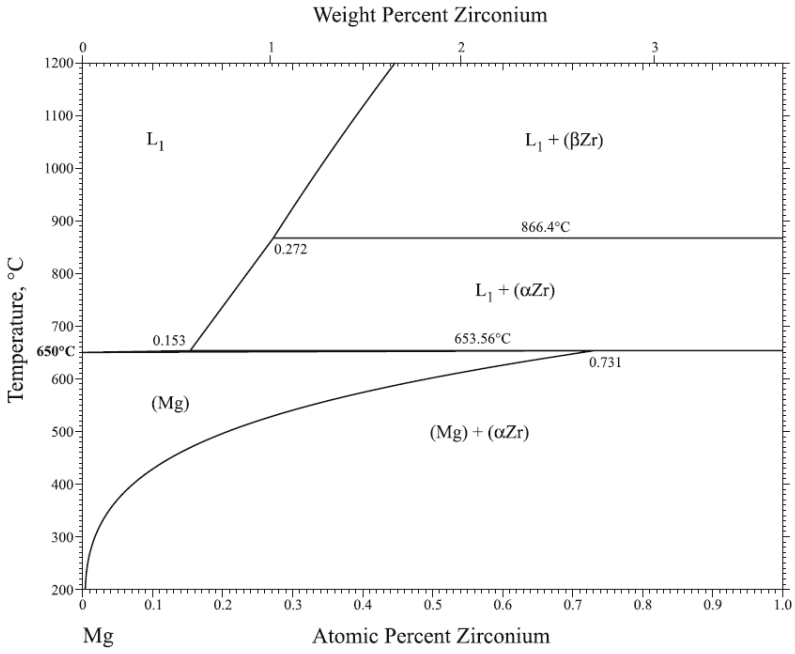

Figure 13. Mg-rich corner of the binary phase diagram of the Mg-Zr system [29].

Zr is a very effective grain refiner in the magnesium alloy systems which do not contain Al, Si, Mn, Fe, Ni, Co, Sn and Sb [30]. The maximum solubility of Zr in molten pure magnesium at 654°C is ~0.6 wt.% (Fig. 13). As per the literature survey by Saunders and Strieter, the powerful grain-refining effect of zirconium on pure magnesium was discovered in the 1930's [31]. Figure 14 shows the effect of Zr addition to magnesium alloy. Emley reported that Zr-rich coring is present in the centre of most of the grains in the microstructure of Zr containing cast magnesium alloys. The intensity of coring in binary Mg-Zr alloy tends to vary as a function of degree of chill [30]. Although the mechanism of grain refinement by Zr in magnesium is not well understood, it is generally attributed to the Zr particles. Since the lattice parameters of α−Zr (a=3.23 Aº, c=5.14 Aº) are similar to that of Mg (a=3.23 Aº, c=5.14 Aº) the Zr particles could provide effective nucleation sites [32]. The Zr-rich cores which tend to form due to the result of peritectic solidification have also been proposed as a mechanism for the grain refinement [30]. Earlier report by Sauerwald suggested that only the Zr which gets dissolved in the liquid magnesium at the time of pouring during casting is effective for grain refinement [33]. Insoluble Zr comprising of undissolved Zr particles were believed to be not useful for grain refinement. But recent work by Tamura et al., reported that even the undissolved Zr particles play an important role in grain refinement [34]. Qian et al studied the effect of stirring, holding time and restirring on the grain refinement of pure magnesium by Zr. They reported that stirring plays an important role in aiding the dissolution of Zr particles by suspending the Zr particles in the melt and reducing the grain size as shown in figure 15 [35]

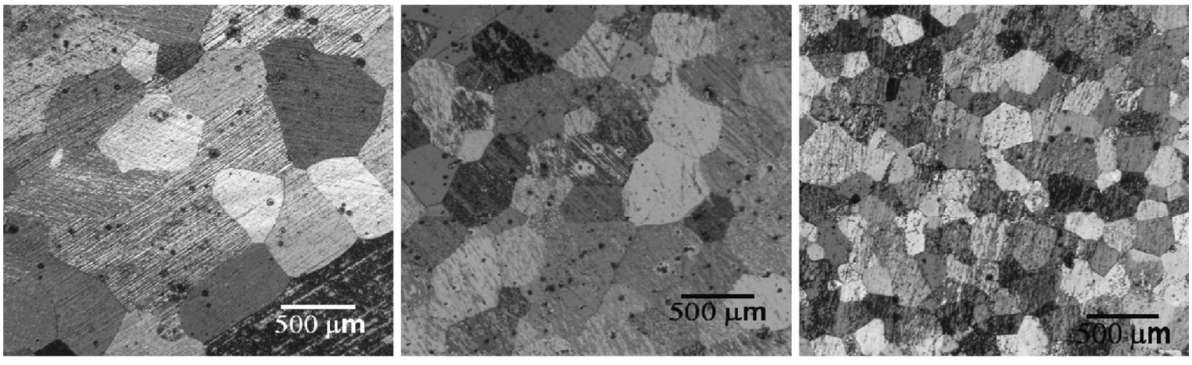

Mg-0.04 wt% Zr Mg-0.15 wt% Zr Mg-0.32 wt% Zr

Figure 14. (b) micrographs of samples with Zr additions showing dramatic decreases in grain size [32].

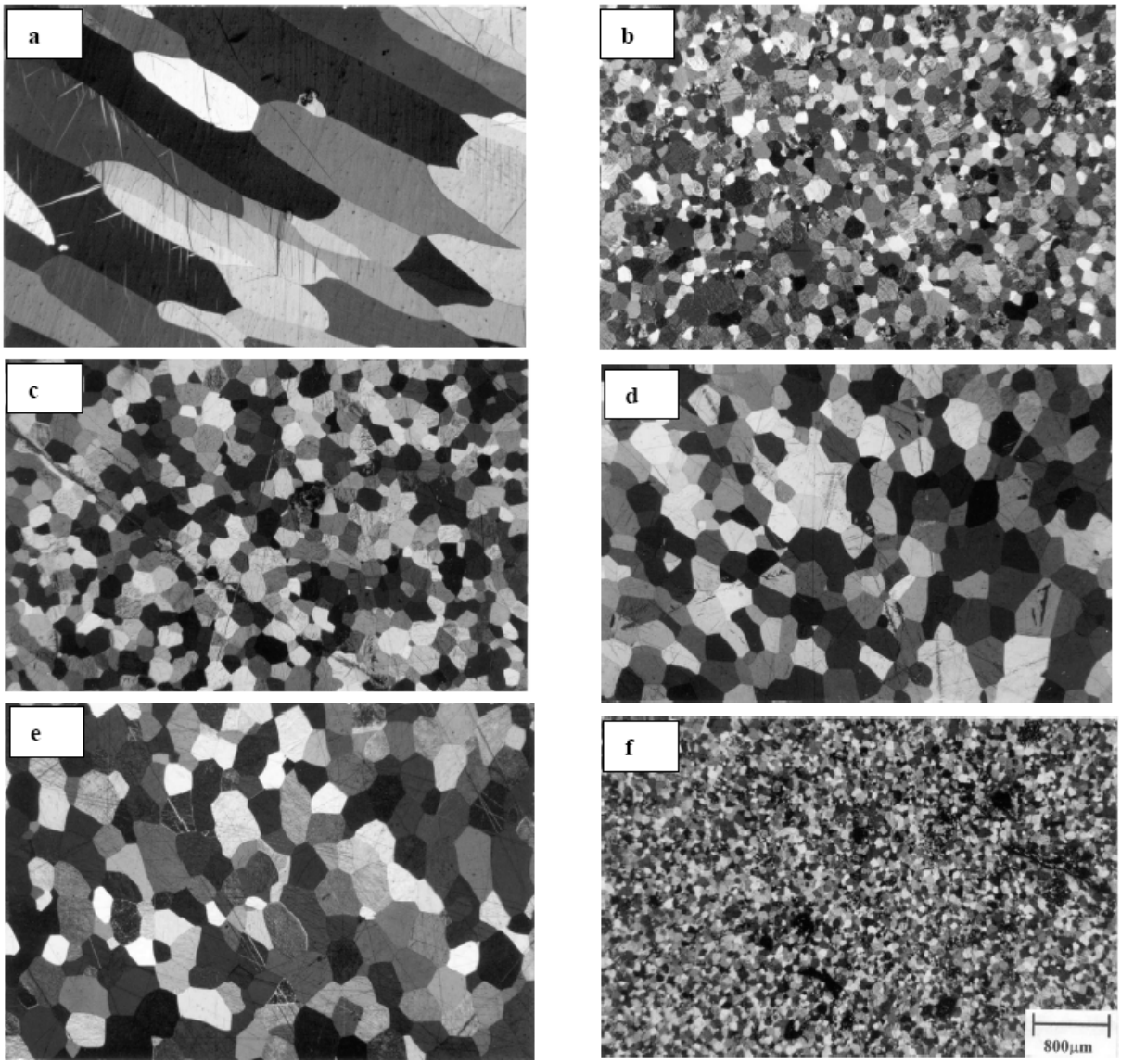

Figure 15. Effect of stirring, holding time and restirring on the grain refinement of pure magnesium by zirconium at 780ºC: (a) before alloying, (b) after 2 min manual stirring following the 1% zirconium addition, (c) 60 min holding after (b), (d) 120 min holding after (b), (e) 360 min holding after (b), and (f) restirring for 60 seconds after (e) [35].

1.6.3 Mg-Zn-Zr alloy

The Mg-Zn-Zr system is the most used system after Mg-Al-Zn alloy system as it shows good mechanical properties. The ZK60 alloy has also been used for commercial applications [9,19]. Zr plays the role as a grain refiner in this system. Earlier work by Doan and Ansel reported that Zr addition to the Mg-Zn alloy tends to increase the solidus temperature (Fig. 16.) which could be useful for wrought processing at higher temperatures [36].

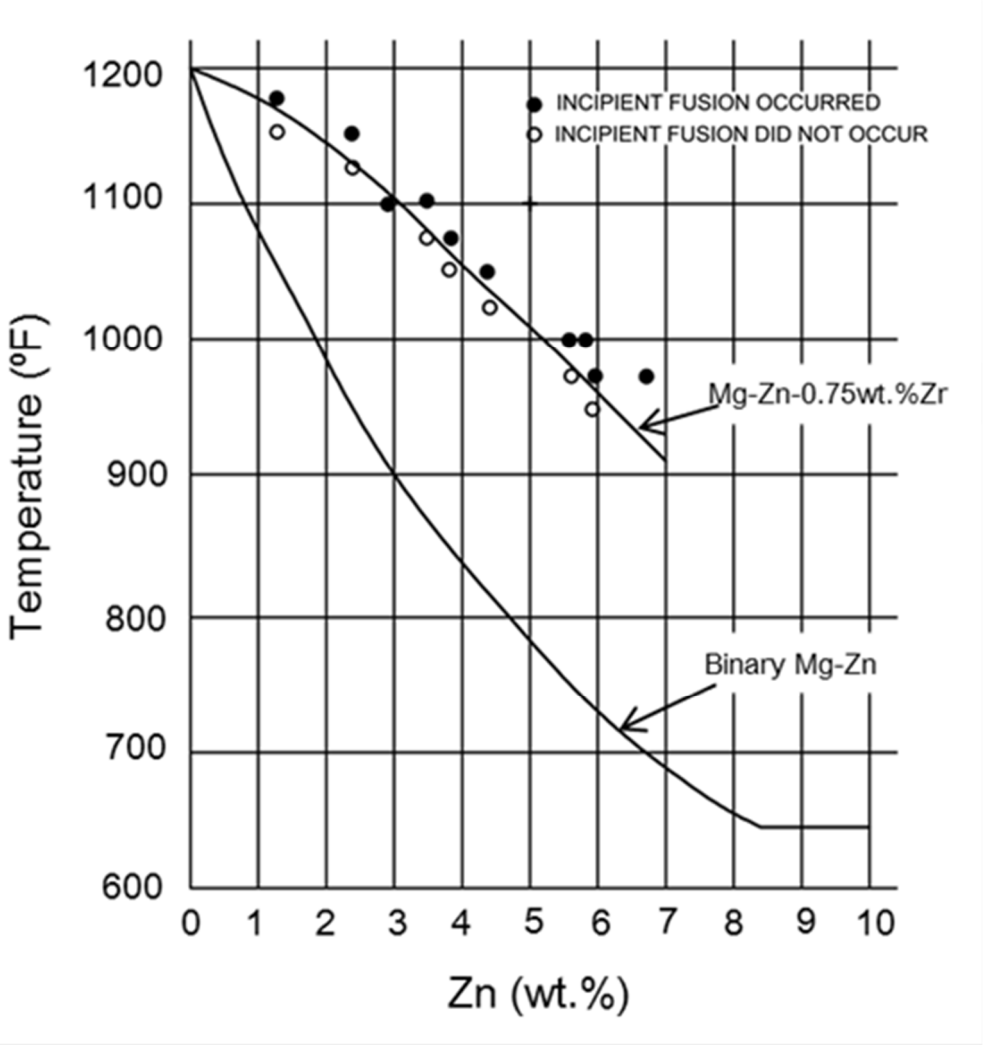

Figure 16. Solidus of Mg-Zn and Mg-Zn-0.75 Zr vs. Zn content [36]

The ability of Zr in cast alloys had also been extended to generate even more enhanced grain refinement in extruded profiles [36]. Recently, Arroyave et al., based on their thermodynamic calculation of a Mg-Zn-Zr alloy explained that since the solubility of Zr in the liquid phase decreases with the decrease in temperature, supercooling can lead to a high density of Zr or Zr-rich nucleus giving rise to grain refinement [37]. However, the effects of other secondary phases on mechanical properties are not well understood in the cast as well as wrought Mg–Zn–Zr alloys. Watanabe et al., reported phases such as Mg(Zn,Zr) and $Mg_7(Zn,Zr)_3$ in their study on ZK60 alloy [38]. It was suggested that $Mg_7(Zn,Zr)_3$ phase could be effective in pinning of grain boundaries. Ren et al., reported in a recent investigation [39] on the isothermal section of Mg-Zn-Zr phase diagram at 345°C (Fig. 17), that in alloys with high concentration of Zr compared to Zn, Zn_2Zr_3 phase is observed while in Zr lean alloys $(MgZr)_2Zn$ phase is detected. Since this system is a commercially important system an understanding of the type of phases formed and their effect of the mechanical properties and texture is important for further development of the Mg-Zn-Zr alloy system.

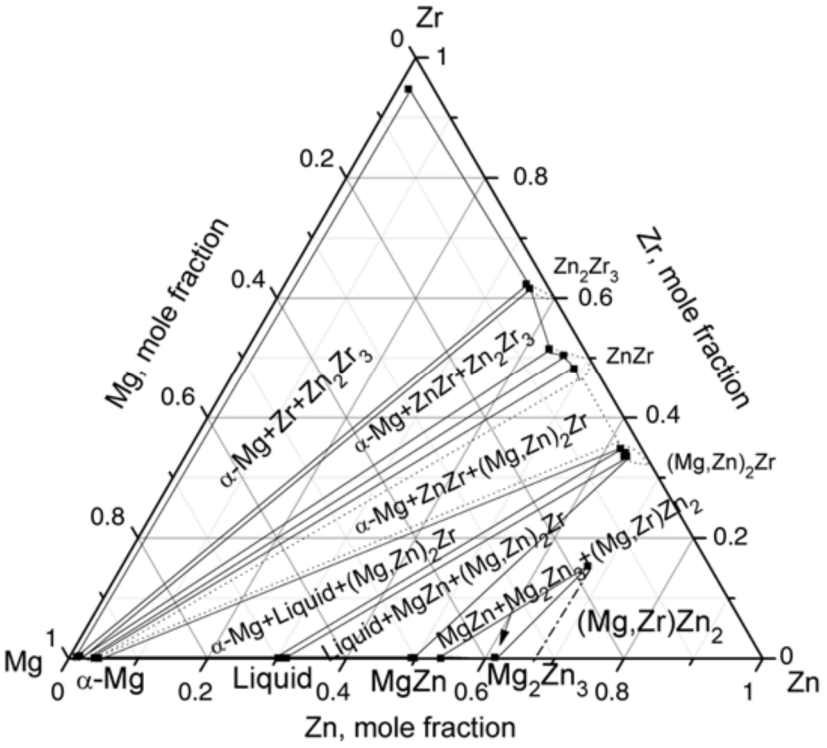

Figure 17. Isothermal section of Mg–Zn–Zr ternary system at 345 °C [39]

1.7. Wrought processes

In this section a general introduction of the following wrought processes used in the present research work are briefly described.

1.7.1 Extrusion

Extrusion is defined as the process by which a block of metal is reduced in cross-section by forcing it to flow through a die orifice under high pressure [40]. There are two basic types of extrusion

(a) Direct extrusion: In this type of extrusion a metal billet is place on a container. The billet is then driven through the die by the ram. A pressure plate is placed at the end of the ram which is in contact with the billet. Figure 18(a) shows a schematic of the direct extrusion process

(b) Indirect extrusion: In this type of extrusion a hollow ram carries the die while the other end of the container is kept closed with a closure plate. Alternately, the ram containing the die could also be kept stationary and container with the billet can also be moved. Figure 18(b) shows a schematic of the indirect extrusion process.

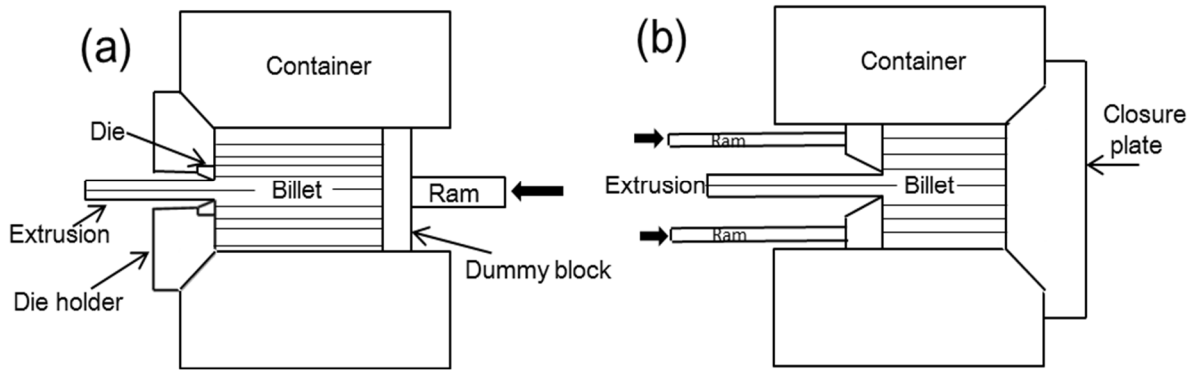

Figure 18. Schematic of (a) direct extrusion and (b) indirect extrusion [40].

1.7.2 Twin roll casting-hot rolling (TRC-HR)

This process combines the process of twin roll casting followed by hot rolling to obtain sheet products. This process eliminates the intermediate reheating steps to obtain the sheet products compared to conventional rolling which makes it a very cost effective process. In this process molten alloy kept in ladle is transferred into a tundish. The liquid metal is then passed through two water cooled rolls rotating at a constant speed to obtain a thin cast strip of thickness less than 3mm. Then the thickness of this twin roll cast strip is further reduced by conventional hot rolling process to obtain a thin sheet. A schematic of this process is shown in Fig. 19.

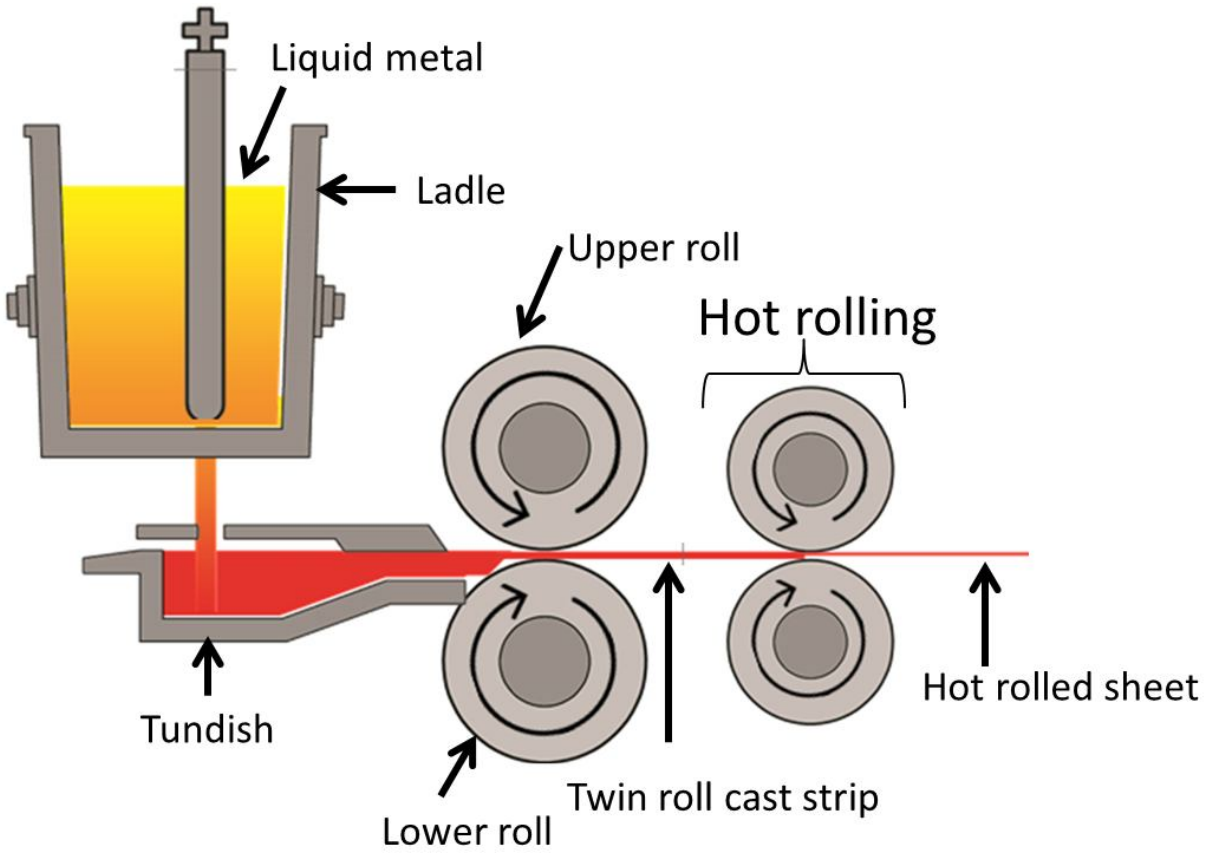

Figure 19. Schematic of combined twin roll casting and hot rolling processes.

References

[1] R. Myers, The basics of chemistry, Greenwood publishing group, 2003.

[2] H. E. Friedrich, B. L. Mordike, Magnesium Technology, Metallurgy, Design Data, Applications, Springer-Verlag Berlin Heidelberg, 2006.

[3] M. B. Lieberman, The Magnesium Industry in Transition, August 17, 2000.

[4] C. S. Roberts, Magnesium and its Alloys, Wiley, 1960.

[5] B. C. Wonsiewicz and W. A. Backofen. Trans. Metall. Soc. AIME, 1967; 239:1422.

[6] L. M. Pidgeon, 'New Methods for the Production of Magnesium', The Canadian Institute of Mining and Metallurgy, 1944; 47:16.

[7] Mayer, A., 'Plant for Production of Magnesium by the Ferrosilicon Process', Trans. AIME, 1944; 159: 363.

[8] W Wulandari, G. A. Brooks, M. A. Rhamdhani, B. J. Monaghan, Magnesium: current and alternative production routes, 2010.

[9] M. M. Avedesian, and H. Baker, Magnesium and Magnesium alloys, ASM speciality handbook, ASM International Metals Park Ohio, 1999.

[10] W. D. Callister, Materials Science and Engineering: An Introduction, 5th edition, John Wiley and sons, 2000.

[11] J. Koike, Met. Mater. Trans A 2005; 36A:1689.

[12] T. Mukai, K. Higashi, Scripta Mater. 2001; 44: 1493.

[13] R. Günther, C. Hartig, and R. Bormann, Acta Mater. 2006;54: 5591.

[14] C. R. Hutchinson, J. F. Nie, S. Gorsse , Met Mater Trans A 2005;36A:2093.

[15] D. R. H. Jones, M. F. Ashby, Engineering Materials 2: An Introduction to Microstructures, Processing and Design, Butterworth-Heinemann, 2005.

[16] L. M. Brown and R. K. Ham, Strengthening Methods in Crystals, A. Kelly and R.B. Nicholson, eds., Elsevier, London, 1971, 12.

[17] J. F. Nie, Scripta Mater. 2003; 48:1009

[18] J. D. Robson, N. Stanford, M. R. Barnett, Metallurgical and Materials Transactions A 2013; 44: 2984.

[19] I. J. Polmear, Light Metals, fourth ed., Butterworth Heinemann, Oxford, 2006.

[20] P. Villars and L. D. Calvert, Pearson's handbook of crystallographic data for intermetallic phases. 2nd edition, ASM international , Materials park, Ohio, (1991)

[21] J. Gallot, K. Lal, R. Graf, A. Guinier, Comptes. Rendus. Acad. Sci. 1964; 258: 2818.

[22] J. Gallot, R. Graf. Comptes. Rendus. Acad. Sci. 1965; 261: 728.

[23] J.S. Chun and J.G. Byrne: J. Mater. Sci. 1969; 4: 861–72.

[24] J. B. Clark, L. Zabdyr and Z. Moser, Phase Diagrams of Binary Magnesium Alloys, ASM International, Metals Park, OH, 1988, 353.

[25] E. O. Hall, J. Inst. Met. 1968; 96: 21.

[26] C. Bettles, M. A. Gibson, K. Venkatesan, Scripta Mater. 2004; 51: 193.

[27] C. L. Mendis, K. Oh-ishi, K. Hono, Scripta Mater 2007; 57: 485.

[28] G. Mima, and Y. Tanaka, Trans Jap Inst Met 1971; 12:71.

[29] H. Okamoto, J. Phase Equilibria and Diffusion 2007; 28: 305.

[30] E. F. Emley, Principles of Magnesium Technology, Pergamon press, Oxford 1966.

[31] W. P. Saunders and F. P. Strieter, Trans. American Foundrymen's Society 1952; 60: 581.

[32] Y. C. Lee, A. K. Dahle, D. H. StJohn, Metall. Mater. Trans. A 2000; 31: 2895.

[33] F. Sauerwald, Z. Metallkd. 1949; 40: 41.

[34] Y. Tamura, N. Kono, T. Motegi, E. Sato, J. Japan Inst. Light Metals 1997; 47: 679.

[35] M. Qian, D. H. StJohn and M. T. Frost: Magnesium Technology 2003, ed. by H. I. Kaplan, TMS, Warrendale PA, USA, 2003, 209.

[36] J. P. Doan, G. Ansel, Trans. AIME 1947; 171: 286.

[37] R. Arroyave, Z.K. Liu, Magnesium Technology 2005,ed. by N. R. Neelameggham, H. I. Kaplan, B. R. Powell, TMS, San Francisco, California, USA, 2005, 203.

[38] H. Watanabe, K. Moriwaki, T. Mukai, T.Ohsuna, K. Hiraga, K. Higashi, Mater. Trans. 2003; 44: 775.

[39] Y.P. Ren, Y. Guo, D.Chen, S. Li, W.L. Pei, G.W. Qin, CALPHAD 2011; 35: 411.

[40] G. E. Dieter, Mechanical Metallurgy, Mc Graw-Hill, 1988.

Chapter 2. The effect of Ag and Ca additions on the age hardening response of Mg-Zn alloys

2.1 Introduction

The Mg-Zn based ZK60 (Mg-6.2Zn-0.6Zr (mass %) or Mg-2.4-0.2Zr (at.%) hereafter all alloy compositions are shown in at.%) alloy, has the best combination of yield strength and ductility among commercial wrought magnesium alloys. Although the Mg-Zn alloys are age hardenable [1-5], ZK60 is not usually age-hardened after wrought processing due to the relatively low age hardening response compared to work hardening. If the age hardening of the Mg-Zn alloys could be enhanced substantially, additional heat treatment after the wrought process would increase yield strength in the final product [6]. Recently we reported that the sole addition of 0.1 at.% Ag as well as the combined trace addition of Ag and Ca to the Mg-2.4Zn alloy refined the dispersion of the β'_1 precipitates, thereby enhancing the age hardening response by 2.5 times higher than that of the binary Mg-2.4Zn alloy [7]. The Mg-2.4Zn-0.1Ag-0.1Ca-0.16Zr alloy was demonstrated to be a good wrought alloy for both extrusion [8] and twin roll casting [9]. The twin roll cast and hot rolled (TRC-HR) Mg-2.4Zn-0.1Ag-0.1Ca-0.16Zr alloy showed a high stretch formability in the solution treated condition (T4), then showed enhanced yield strength of 320 MPa and an ultimate tensile strength of ~342 MPa with an elongation to failure of 17% after an artificial aging (T6) [9]. The extruded Mg-2.4Zn-0.1Ag-0.1Ca-0.16Zr alloy also showed a yield strength of 325 MPa and an ultimate tensile strength of 360 MPa with an elongation of 15% after a T6 treatment [8]. These investigations have shown that this alloy has significant potential as a heat treatable wrought magnesium alloy with a balanced combination of formability, strength and ductility.

The refinement of the precipitate microstructure and the resulting enhancement in the age hardening response in the Mg-2.4Zn-0.1Ag-0.1Ca alloy have been attributed to the association of Ag and Ca with the β'_1 $MgZn_2$ precipitates [8]. However, the role of the Ag and Ca additions in refining the peak-aged microstructure is not well understood. In particular, the individual role of Ag and Ca on the precipitation kinetics has not been investigated yet. The aim of this work is to clarify the role of the trace additions of Ag and Ca on the precipitation process of the Mg-2.4Zn alloy by detailed microstructure investigations using

transmission electron microscopy (TEM) and three-dimensional atom probe (3DAP).

2.2. Experimental

The alloys were prepared by induction melting high-purity Mg, Zn, Ag and Mg-33.3at.% Ca in a steel crucible and casting them into a steel mold in an Ar atmosphere. The chemical compositions of the alloys used in this work are summarized in Table 1 in both atomic and mass percent with the nomenclatures of the alloys. Hereafter, the sample types are shown using the nomenclatures. The ingots were encapsulated in Pyrex tubes filled with high purity He and homogenized for 48 h at 340°C. The alloy samples were solution treated for 1 h at 400°C in He filled quartz tubes, quenched in water and then aged in an oil bath at 160°C. The Z6 alloy was additionally aged at a lower temperature of 70°C. The Vickers hardness with a 1 kg load was measured for all the samples with 10 individual indentations.

Thin foil specimens for transmission electron microscopy (TEM) were prepared by punching 3 mm diameter discs and twin jet electro-polishing using a solution of 300 ml 2-butoxy ethanol, 15.9 g lithium chloride, 33.5 g of magnesium perchlorate in 1500 ml methanol at a temperature of ~ -45°C. The microstructure was examined using FEI Tecnai 20 and Philips CM200 TEM operating at 200 kV. The number density of precipitates was calculated using the stereographical methods described by Underwood [10] using the formula $N_V = \frac{N_A}{t + \overline{D}}$, where N_A is the number density of the precipitates in the projected volume, t is the thickness of the TEM specimen and $\overline{D}$ is the average projection length of the precipitates. $\overline{D}$ is given by $c/2$ for square rods where c is the length of the precipitates. The thickness of the thin foil was determined using the convergent beam electron diffraction (CBED) pattern analysis where the 0002 reflection was excited as described by Williams and Carter [11].

Square bars of ~15 × 0.5 × 0.5 mm^3 were electro-polished in a solution of 5 vol% perchloric acid in 2–butoxy ethanol to prepare sharp needle-like specimens for atom probe analysis. The atom probe analyses were conducted with a locally built laser assisted 3D atom probe. A femto-second laser with a wave length of 343 nm was used to irradiate the specimen to assist field evaporation. All the measurements were conducted under ultra-high vacuum ($<1\times10^{-8}$ Pa) at a base temperature of 20-30 K in the flux range of 0.001–0.01 atom/pulse.

2.3. Results

2.3.1. Precipitation in Mg-Zn alloy

The age hardening curves of the binary the Z6 alloy, at 70°C and 160°C are shown in Fig. 1. At 70°C, the hardness starts to increase after a long incubation time of 100 h, whereas at 160°C, the hardness starts to increase after 1 h of aging and reaches the peak hardness at 120 h.

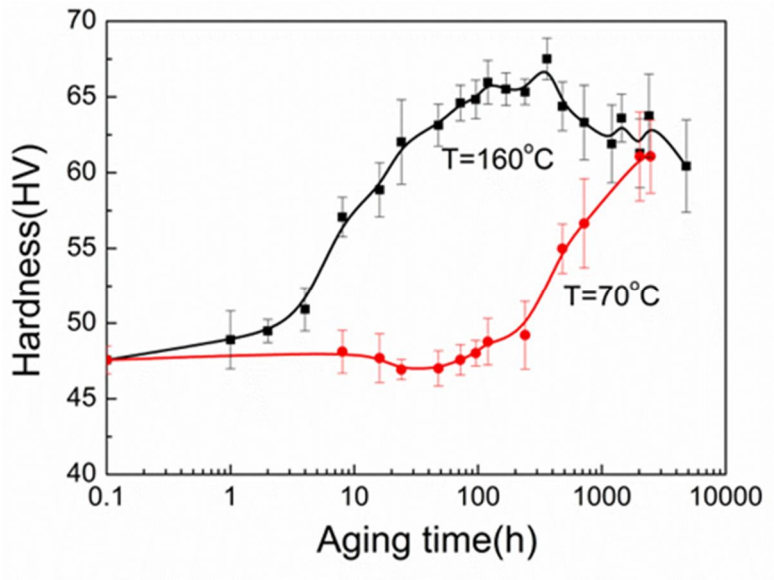

Figure 1: Age hardening response of the Z6 alloy at 70°C and 160°C.

The TEM micrographs of the alloy aged at these two temperatures in Fig. 2 and 4 show the precipitates that are responsible for the age hardening. At 160°C, only dislocations are observed up to 2 h (Fig. 2(a)) but rod-like precipitates are observed after 8 h of aging (Fig. 2(b)). The selected area electron diffraction (SAED) pattern observed from this stage indicates that the precipitates are the β'_1 that are commonly observed in Mg-Zn based alloys having an orientation relationship of $\{2\bar{1}\bar{1}0\}\ \beta'_1 // (0001)_{Mg}$ and $[0001]\ \beta'_1 // \langle 2\bar{1}\bar{1}0\rangle_{Mg}$ with the matrix [12,13]. In addition, plate-like precipitates (β'_2) are observed after aging for 24 h and above. The β'_2 precipitates have an orientation relationship of $\{2\bar{1}\bar{1}0\}\ \beta'_2 // \{10\bar{1}0\}_{Mg}$ and $[0001]\ \beta'_2 // [0001]_{Mg}$ with the matrix as previously reported [8]. The number density and the size of the rod-like β'_1 precipitates after aging for 8, 24 and 120 h are shown in Table 2. The size (length and diameter) of the β'_1 precipitates increases with aging time. The number density of the precipitates also increases with an increase in aging time. The series of the TEM images indicate that the precipitation sequence in the Z6 alloy at 160°C is :

α′ (supersaturated α-Mg solid solution) → α + β'_1 → α + β'_1 + β'_2 (at 160°C)

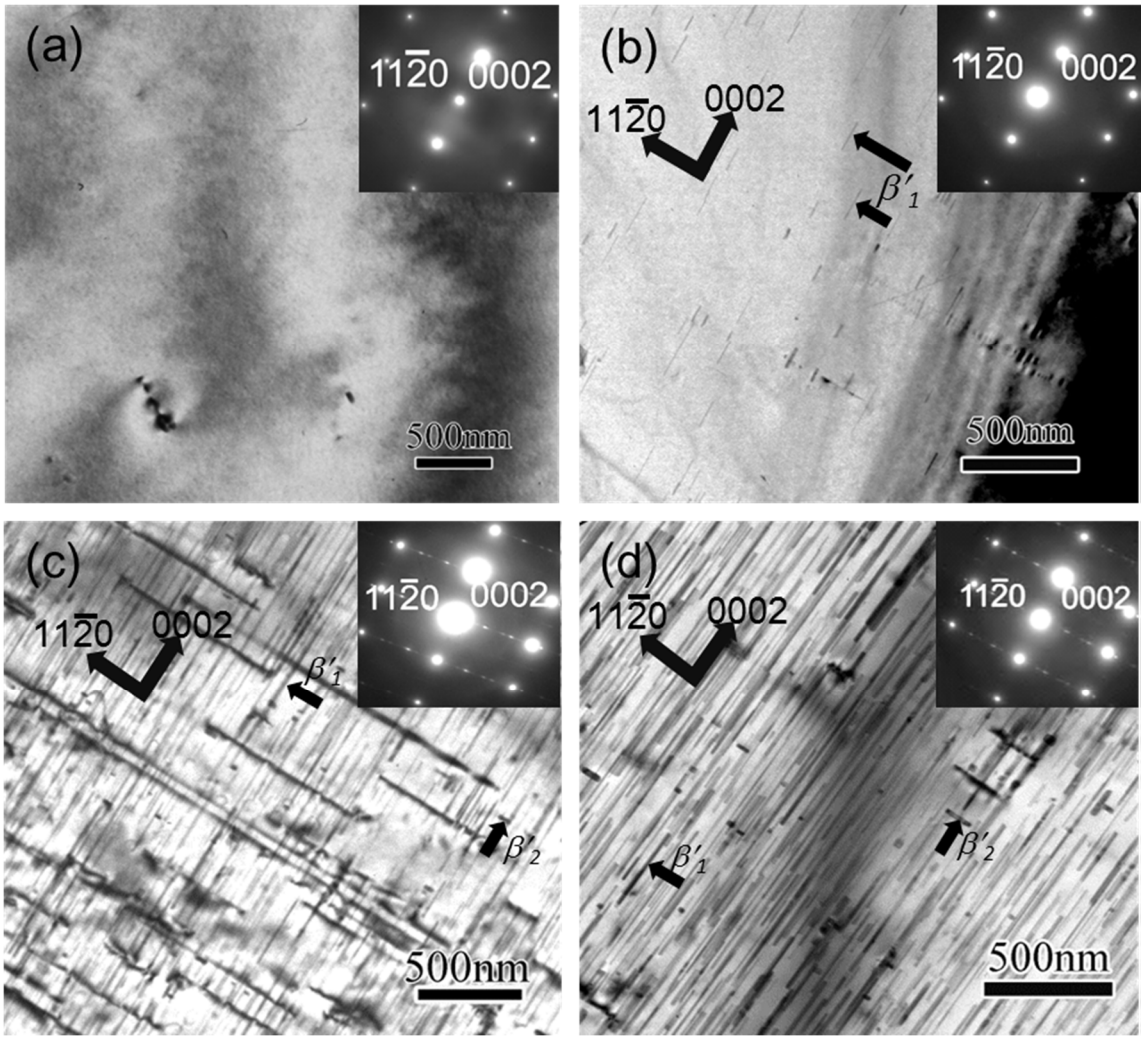

Figure 2: Bright field TEM images of the Z6 alloy at different aging times at 160°C. (a) 2 h, (b) 8 h, (c) 24 h and (d) 120 h (peak-aged). Electron beam is approximately parallel to the <10$\bar{1}$0> direction.

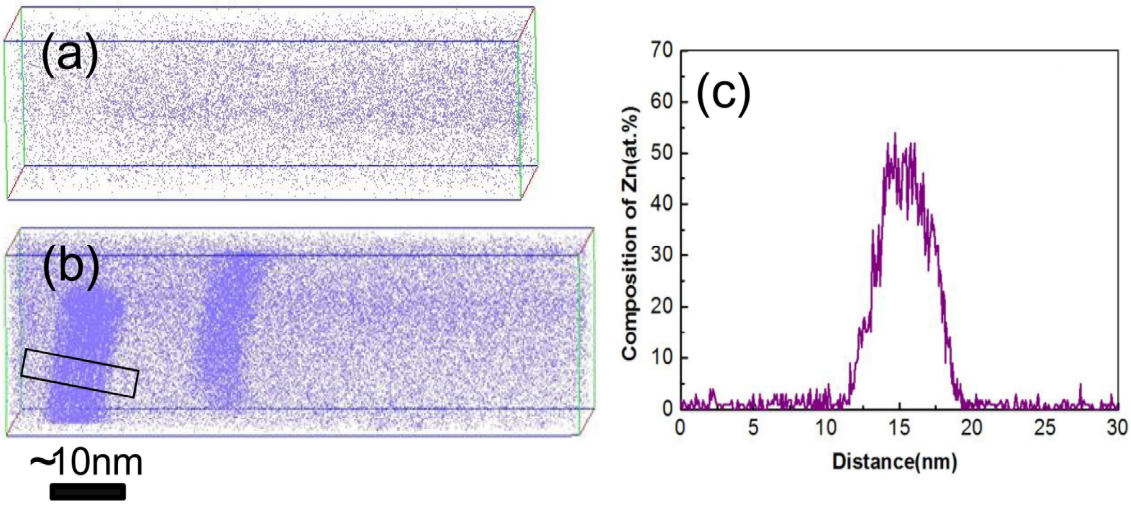

Figure 3: 3DAP map of Zn for the Z6 alloy aged at 160°C for (a) 2 h, (b) 8 h; (c) the composition profile of Zn for the selected rod precipitate marked in (b).

The 3DAP Zn maps obtained from the Z6 alloy aged for 2 h and 8 h at 160°C are shown in Fig. 3 (a) and (b), respectively. No apparent clusters of Zn atoms are observed in the sample aged for 2 h; therefore, it is still a supersaturated solid solution, α′. However, Zn-rich rod-like precipitates (β'_1) appear after 8 h aging as shown in Fig. 3 (b). Fig. 3 (c) shows the composition profile calculated from the selected volume across the rod-like precipitate in Fig. 3 (b), indicating that the composition of the precipitate is close to MgZn.

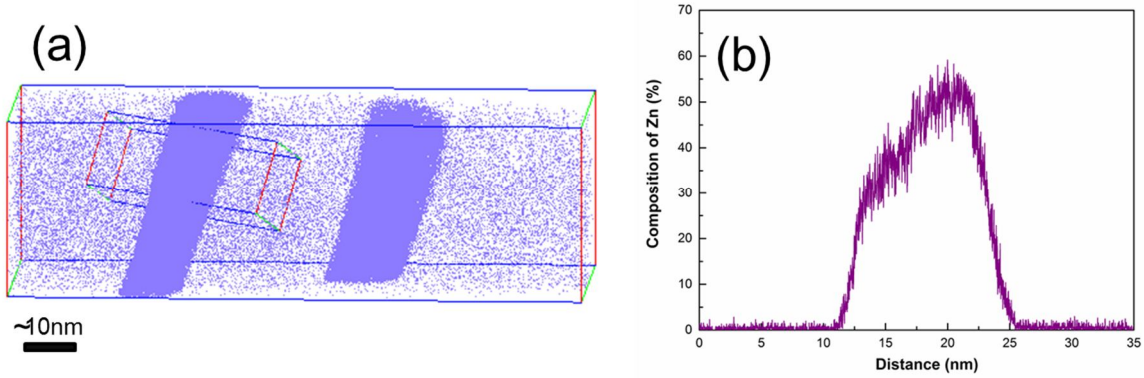

Figure 4: 3DAP map of Zn for the Z6 alloy aged at 160°C for 72 h (b) the composition profile of Zn for the selected rod precipitate marked in (a)

The 3DAP Zn maps obtained from the Z6 alloy aged for 72 h at 160°C (peak-aged) is shown in Fig. 4 (a). Fig. 4 (b) shows the composition profile of one of the Zn-rich rod-like precipitates (β'_1) from a selected volume across the rod-like precipitate in Fig. 4 (a). The precipitate composition is ~ MgZn and the thickness of the precipitates is around 15nm.

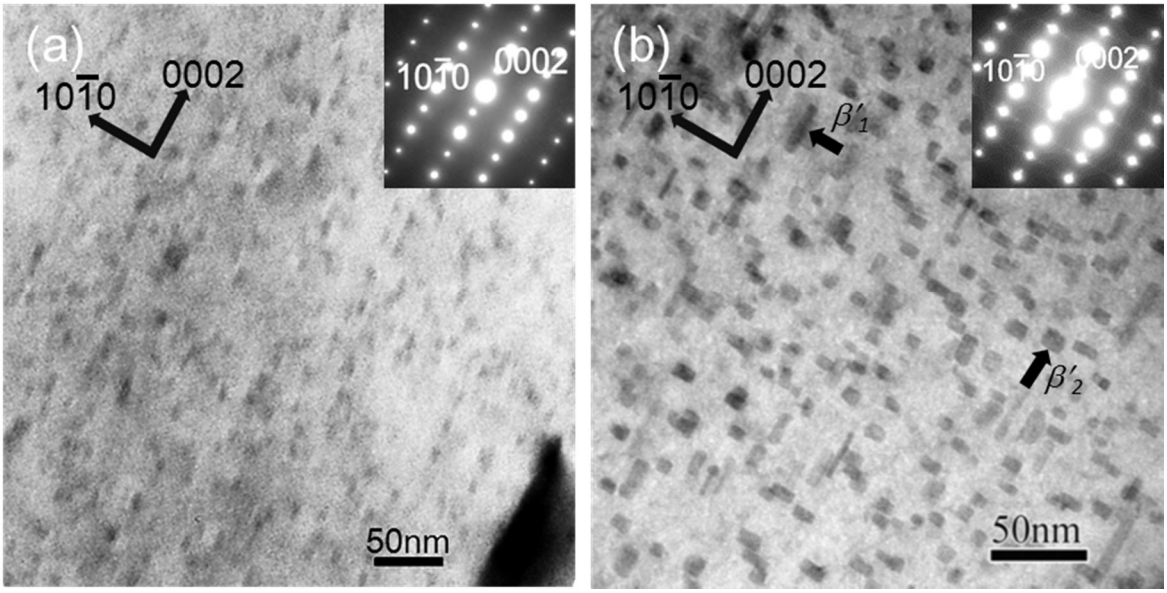

Figure 5: Bright field TEM images of the Z6 alloy aged at 70°C for (a) 100 h and (b) 1000 h. Electron beam is approximately parallel to the <11$\bar{2}$0> direction.

At 70°C, the hardness starts to increase after a long incubation period of 100 h as shown in Fig. 1. Fig. 5 (a) and (b) show TEM bright field images and a selected diffraction patterns taken from the Z6 alloy aged for 100 h and 1000 h at 70°C, respectively. Weak contrast indicating the presence of some fine precipitates is observed in the sample aged for 100 h. However, the SAED pattern does not show any extra diffraction spots from a secondary phase. The TEM image of the sample aged for 1000 h clearly show the presence of both β'_1 and β'_2 precipitates. Note that the relative number density of β'_2 precipitates with respect to β'_1 is larger than that of the sample aged at 160°C because of a larger driving force for the precipitation resulting from a larger supercooling.

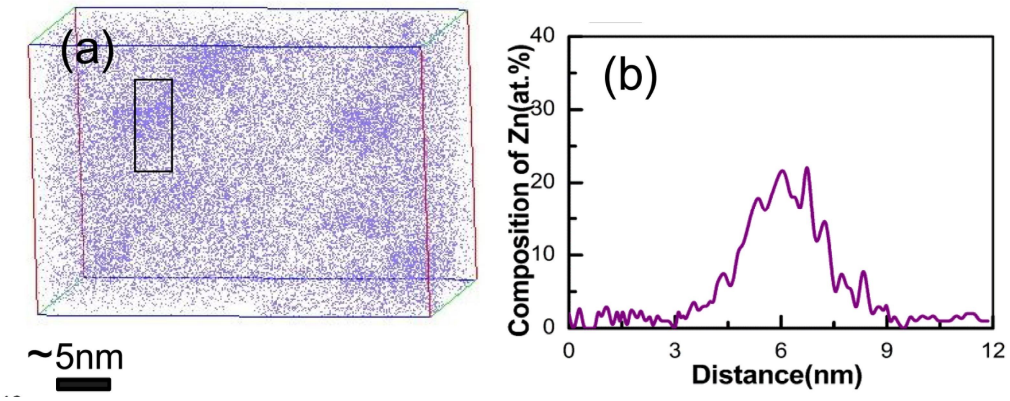

Figure 6: 3DAP map of Zn for the Z6 alloy aged at 70°C for (a) 100 h (b) the composition profile of Zn for the G.P. zone marked in (a).

The Zn distribution in the 100 h aged sample was analyzed by 3DAP, as shown in Fig. 6 (a), to see the initial precipitate that was responsible for the onset of the age hardening at 100 h at 70°C. It shows the presence of spherical clusters of Zn atoms or G.P. zones. The composition of Zn in the G.P. zones is at least ~20at.% as shown in Fig. 6 (b). This indicates that the precipitation sequence of the Z6 alloy at 70°C is

$$\alpha' \rightarrow \alpha + \text{G. P. zones} \rightarrow \alpha + \beta'_1 + \beta'_2 \text{ (at 70°C)}$$

Due to the large supersaturation and the high driving force for precipitation at low temperature, fully coherent Zn-rich clusters or G.P. zones form prior to the precipitation of the β'_1 phase at 70°C. Naturally, the G.P. zones serve as heterogeneous nuclei for the β'_1; therefore, the number density of the β'_1 precipitate increase substantially by pre-aging below 70°C, as reported previously by Oh-ishi et al. [14].

2.3.2. Microalloying Effect in Age Hardening

The age hardening curves of binary Z6, ZX60 microalloyed with Ca, ZQ60 microalloyed with Ag, and ZQX600 microalloyed with both Ca and Ag at 160°C are shown in Fig. 7. The initial hardness after the

solution heat treatment was nearly the same regardless of the microalloying additions at about 50 HV. The Z6 alloy shows only a small hardness increase of ΔHV ~18 after aging for 120 h. The sole addition of 0.2 mass% Ca to the Z6 alloy caused a hardness increase of ΔHV ~25 and also shortened the peak aging time from 120 h to 24 h. The sole addition of Ag leads to a hardness increase of ΔHV ~35 for peak aging at 72 h. The peak hardness of the alloy with the combined addition of Ag and Ca is much higher than those for the binary and ternary alloys with a hardness increment of 45 HV for the peak aging time of 72 h.

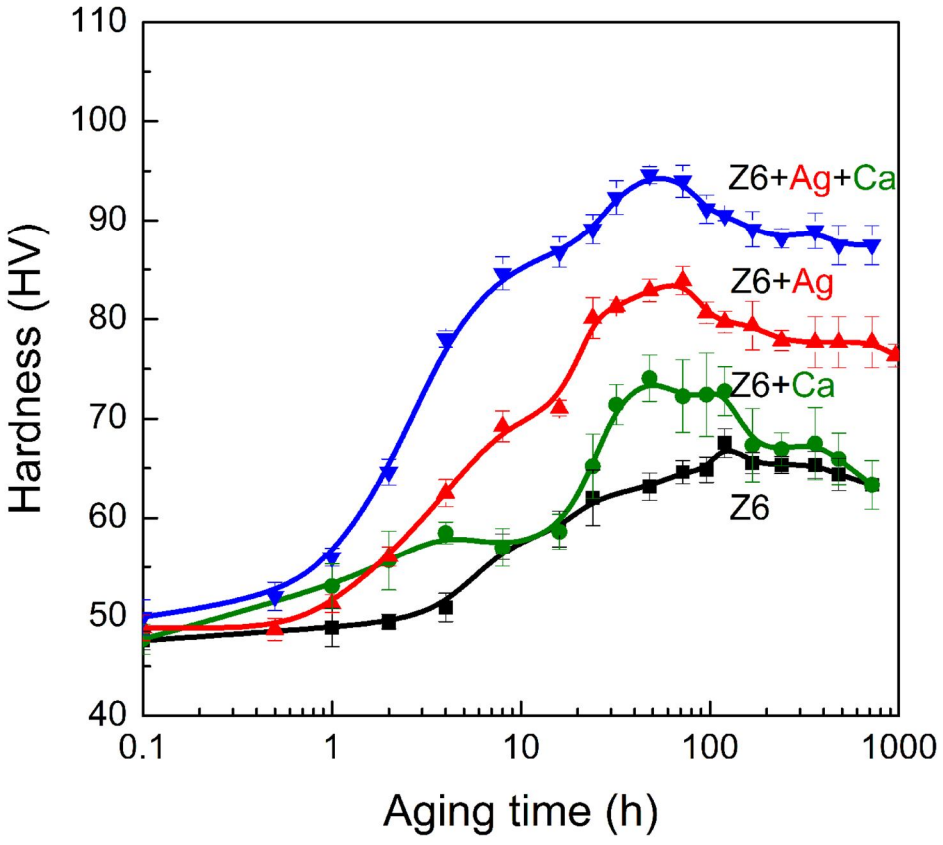

Figure 7: The age hardening response of the Z6, ZX60, ZQ60 and ZQX600 alloy at 160°C.

2.3.3. Microstructure Evolution of the ZX60 alloy

The bright field (BF) TEM images of the ZX60 alloy aged at 160°C for 30 min, 4 h, 8 h and 24 h (peak-aged) and the corresponding SAED patterns are shown in Fig. 8. The BF TEM image of the sample aged for 30 min, Fig. 8(a), shows only dislocations. No diffraction spots from a secondary phase are seen in the diffraction pattern. Rod-like precipitates are observed in the BF TEM images of the samples aged for over 4 h as shown in Fig. 8(b-d). The number density and the size of rod-like precipitates for various aging times are summarized in Table 2. As the aging time increased from 4 h to 24 h (peak-aged), the size (length and diameter) of the precipitates increased. The number density of β'_1 precipitates also increased in the peak-aged condition compared to that in the samples aged for 4 h and 8 h. The number density of the precipitates in the peak-aged condition is one order magnitude higher than that of the binary Z6 alloy.

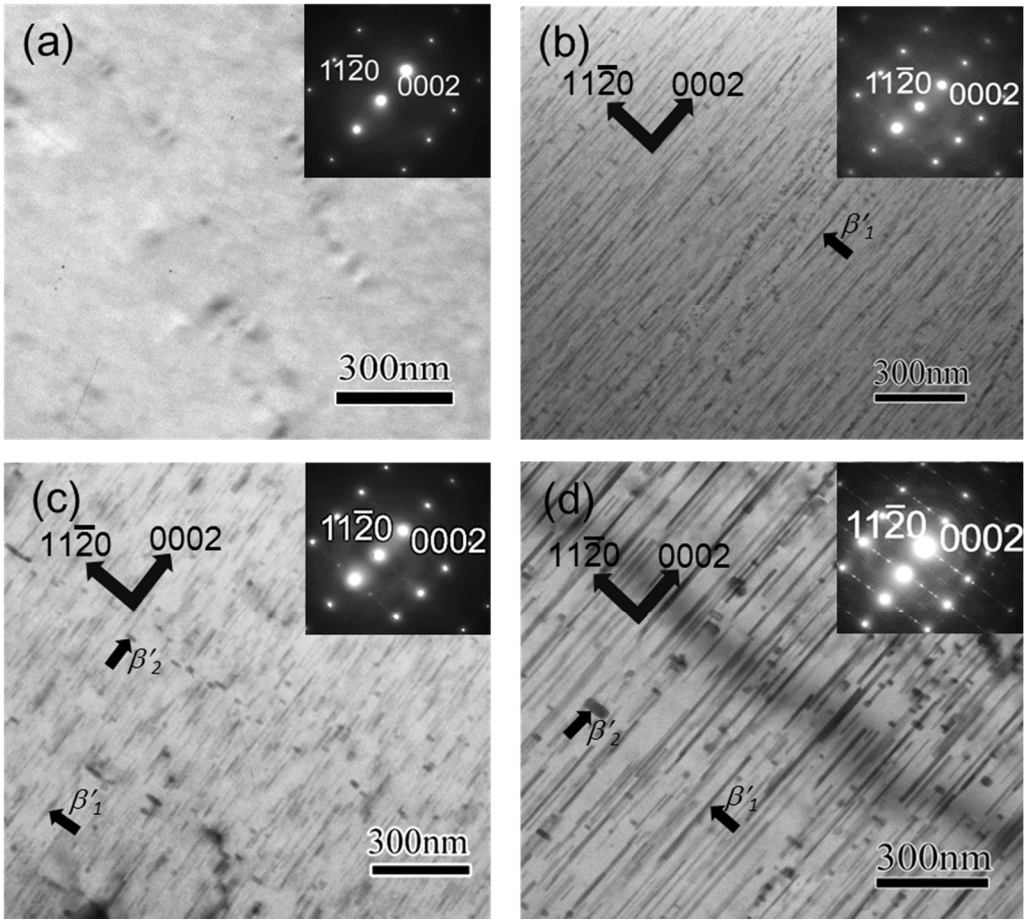

Figure 8: Bright field TEM images of the ZX60 alloy at different aging times at 160°C. (a) 30 min, (b) 4 h, (c) 8 h and (d) 24 h (peak-aged). Electron beam is approximately parallel to the $<10\bar{1}0>$ direction.

The 3DAP analysis results for the ZX60 alloy aged for 30 min and 4 h at 160°C are shown in Fig. 9. Ca and Zn atoms are uniformly distributed in the sample aged for 30 min as shown in Fig. 8(a). The contingency table for the ZX60 aged for 30 min is shown in Table 3. The rows and columns of these contingency tables represent the number of Zn and Ca atoms, respectively, in a block of 100 atoms. The test of independence between statistically random and experimentally observed distribution values were evaluated by using the χ^2 test [15], and the hypothesis that they are identical was tested at a significance level of 1%. The probability of the random distribution should be less than 1% to reject the null hypothesis. The experimentally observed χ^2 value of Zn-Ca was 3.2 with 4 degrees of freedom. Based on this result, the null hypothesis cannot be rejected, indicating that there is no tendency for Ca and Zn to co-cluster.

The sample aged for 4 h in Fig. 9(b) shows rod-like precipitates, which is consistent with the TEM results showing the presence of β'_1 precipitates. The atom maps and the concentration profiles obtained from the precipitate indicate that Ca is preferentially partitioned in the Zn-rich β'_1 precipitates. The composition profile of the selected volume containing the rod-like precipitate in Fig. 9 (c) shows ~40 at.% Zn and ~1 at.% Ca. Although the Zn content is slightly lower than MgZn, it is consistent with the β'_1 precipitate in the binary alloy within the accuracy of the atom probe analysis.

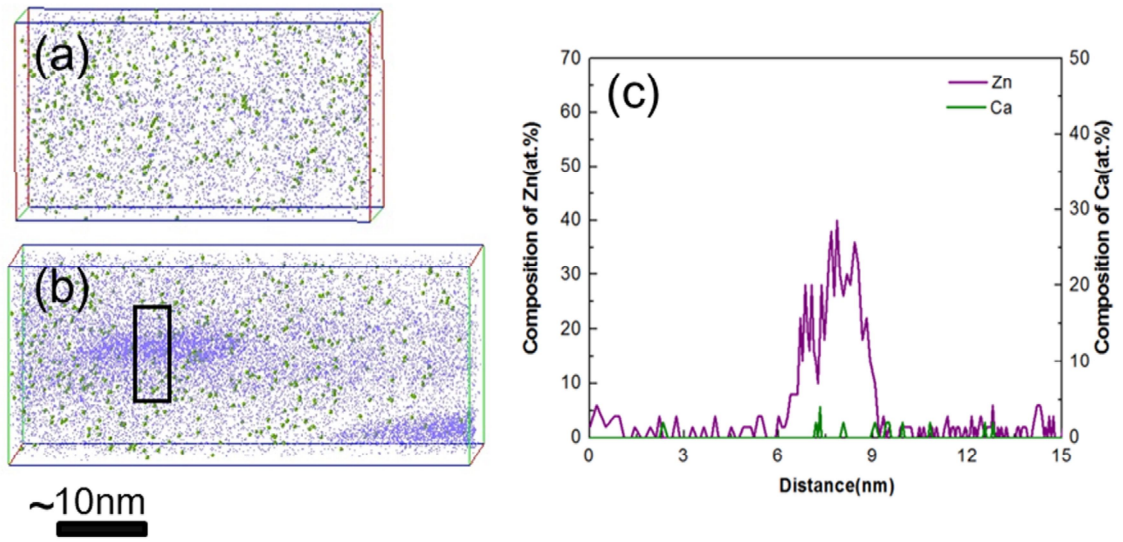

Figure 9: 3DAP map of Zn and Ca for the ZX60 alloy aged at 160°C for (a) 30 min, (b) 4 h; (c) the corresponding composition profile of Zn and Ca for the precipitate marked in (b).

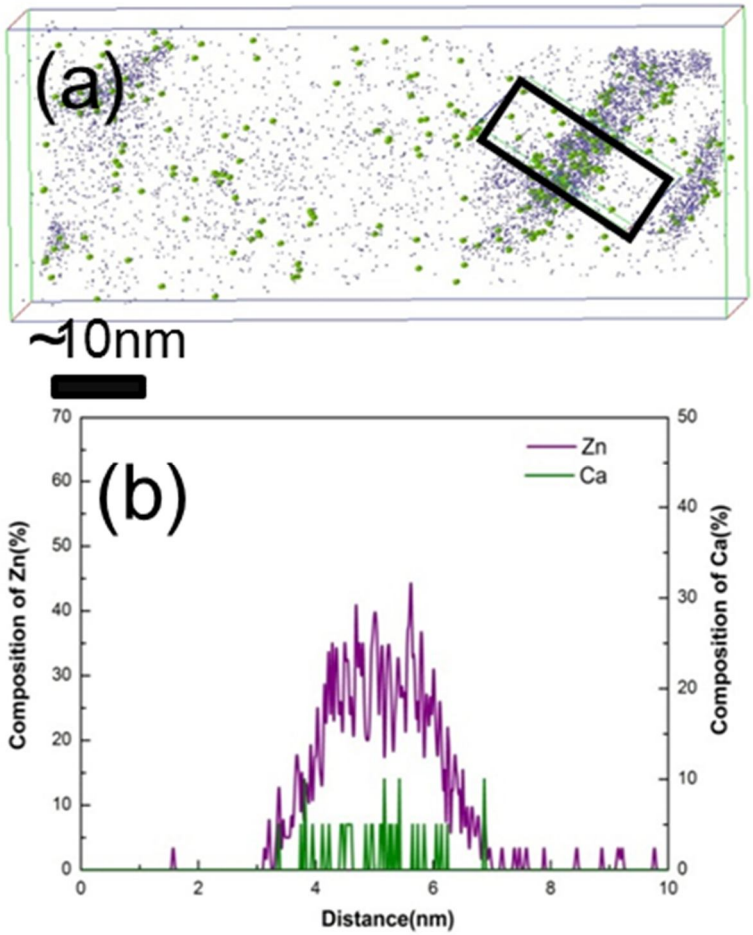

Figure 10: (a) 3DAP map of Zn and Ca for the ZX60 alloy aged at 160°C for 24 h (peak-aged); (b) the corresponding composition profile of Zn and Ca for the precipitate marked in (a).

Figure 10(a) shows the 3DAP map of ZX60 alloy sample aged for 24 h at 160^{o}C. In the analyzed volume of ~25×25×50 nm^3 rod like β'_1 precipitates can be seen. The composition details of one of the rod precipitate marked in Fig. 10(a) is shown in Fig. 10(b). The composition of the precipitate showed concentration of Zn at ~40at.% with Ca concentration being ~2 at.%.

2.3.4. Microstructure evolution of the ZQ60 alloy

The TEM BF images of the ZQ60 alloy aged at 160°C for 2h, 8 h, 24 h and 72 h (peak-aged) and the corresponding SAED patterns are shown in Fig. 11. The BF TEM images of the samples aged for 2 h shows only dislocations. The SAED pattern also does not show any reflections other than those due to the Mg matrix. Rod-like precipitates are observed in the sample aged for more than 8 h at 160°C. In addition to the rod-like precipitates, plate-like precipitates on $(0001)_{Mg}$ are also observed in the samples aged for 24 h and peak-aged for 72 h. The number density and the size of the rod-like precipitates after aging for 8 h, 24 h and 72 h are summarized in Table 2. As the aging time increases, the size (length and diameter) of the β'_1 precipitates increases. The number density of the β'_1 precipitates also increases by one order of magnitude in the peak-aged condition compared to that in the binary Z6 alloy (Fig. 2 (d)).

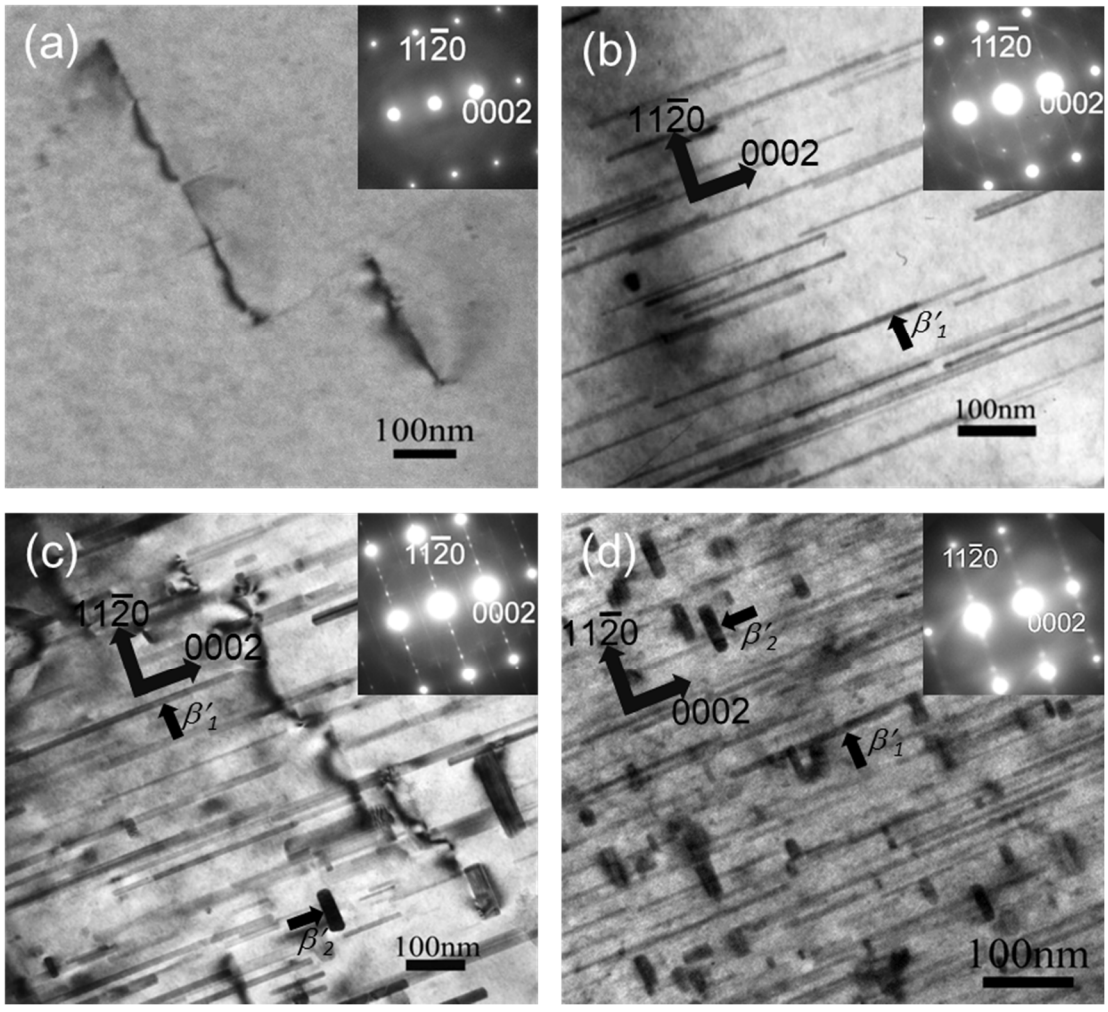

Figure 11: Bright field TEM images of the ZQ60 alloy at different aging times at 160°C. (a) 2 h, (b) 8 h, (c) 24 h and (d) 72 h (peak-aged). Electron beam is approximately parallel to the $<10\bar{1}0>$ direction.

The 3DAP analysis of the ZQ60 samples that were aged for 2 h and 8 h at 160°C are shown in Fig. 12. The sample aged for 2 h at 160°C shows a uniform distribution of Ag and Zn atoms, Fig. 12(a). The contingency table for the ZQ60 alloy aged for 2 h is shown in Table 4. The rows and columns represent the number of Zn and Ag, respectively, in a block of 100 atoms. The χ^2 value for the test of independence of these two tables was 10.0 with 5 degrees of freedom. Based on this result, the null hypothesis that the two tables are independent cannot be rejected, indicating that there is no tendency for Zn and Ag to co-cluster. The sample aged for 8 h, Fig. 12(b), shows rod like precipitates. The composition profile of the precipitate taken from the selected volume, Fig. 12(c), shows that the precipitate contains ~45 at.% Zn and ~1 at.% Ag, which is close to MgZn within the accuracy of the atom probe analysis. This indicates that the first precipitates that appear in the ZQ60 alloy are β'_1.

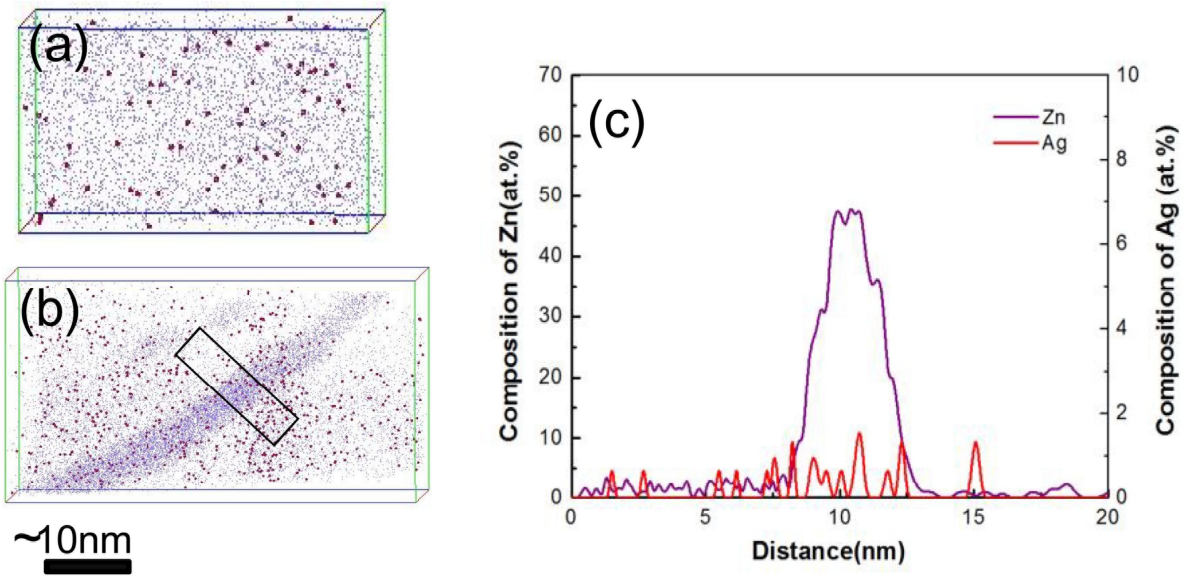

Figure 12: 3DAP map of Zn and Ag for the ZQ60 alloy aged at 160°C for (a) 2 h, (b) 8 h; (c) corresponding composition profile of Zn and Ag for the precipitate marked in (b).

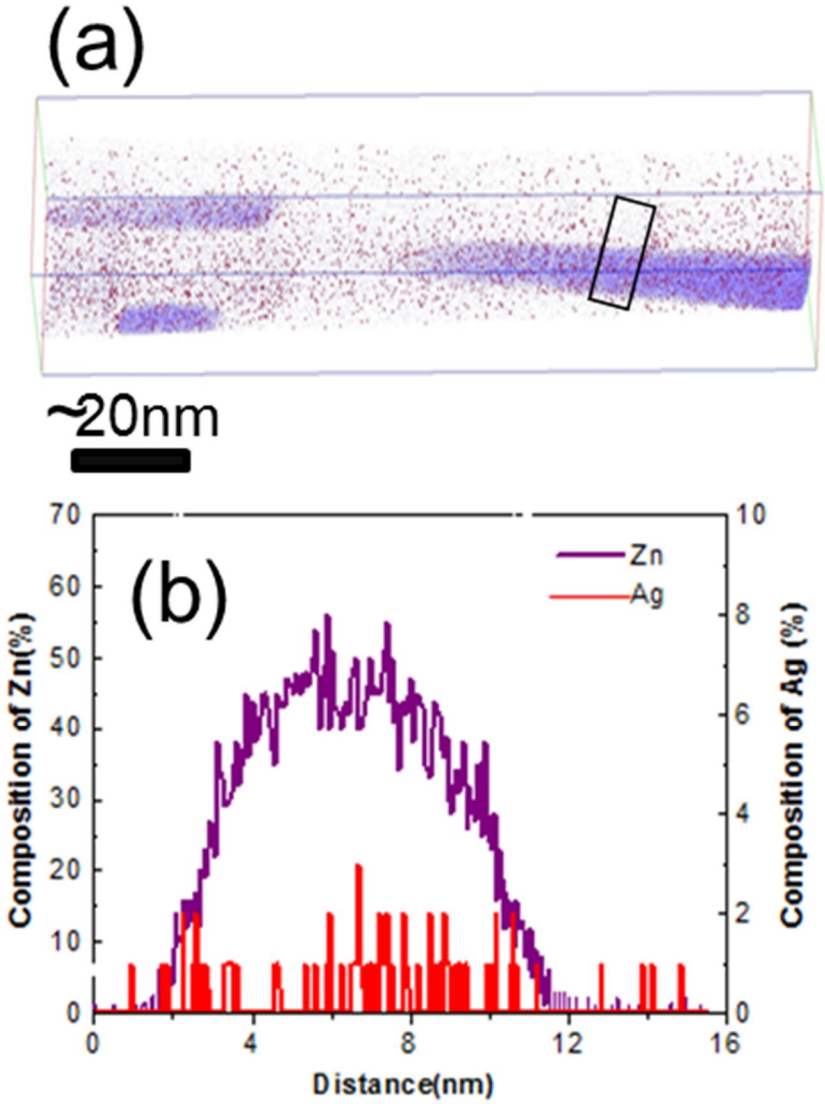

Figure 13: (a) 3DAP map of Zn and Ag for the ZQ60 alloy aged at 160°C for 72 h (peak-aged); (b) the corresponding composition profile of Zn and Ag for the precipitate marked in (a).

The 3DAP map of peak-aged ZQ60 sample (72 h at 160°C) sample also similar rod like precipitates as shown in the Figure 13(a). Composition profile of one of the selected rod-like β'_1 precipitate marked in Fig. 13(a) is shown in Figure 13(b). The composition profile of the rod like precipitate showed that the composition of the precipitate was approximately 50 at.% Zn and ~2 at.% Ag.

2.3.5. Microstructure evolution of the ZQX600 alloy

The TEM BF images of the ZQX600 alloy aged at 160°C for 10 min, 30 min, 2 h, 8 h, 72 h (peak-aged) and 1000 h (over-aged) and the corresponding SAED patterns are shown in Fig. 14. The sample aged for 10 min (Fig. 14 (a)) shows a high density of dislocations. The corresponding SAED pattern also does not show any reflections other than those due to the Mg matrix. The sample aged for 30 min also show dislocations but with some dotted contrast which may be due to the presence of Zn rich clusters, Fig. 14(b). Rod-like precipitates (β'_1) are observed in the samples aged for more than 2 h, Fig. 14(c-f). The number density and the size of the β'_1 precipitates after aging for 2 h, 8 h, 24 h, 72 h (peak-aged) and 1000 h (over-aged) are shown in Table 2. As the aging time increases, the size (length and diameter) of the precipitates increases. The number density of the precipitates increases with an increase in aging time till the peak aging time of 72 h and then decreases slightly on over aging due to the coarsening of the precipitates. There is a two order increment in the number density of β'_1 in ZQX600 compared to that of the peak-aged binary Z6 alloy, Table 2.

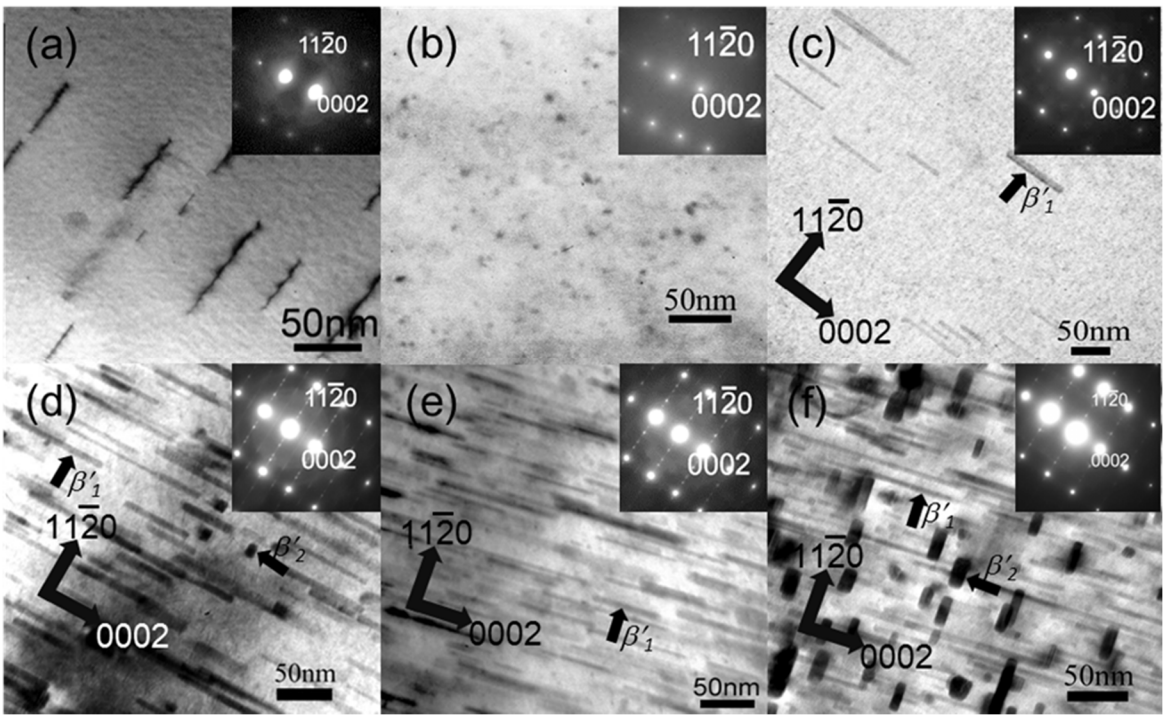

Figure 14: Bright Field TEM images of the ZQX600 alloy at different aging times at 160°C for (a) 10 min, (b) 30 min, (c) 2 h, (d) 8 h, (e) 72 h (peak-aged) and (f) 1000 h (over-aged). Electron beam is approximately parallel to the <10$\bar{1}$0> direction.

The ZQX600 samples that were aged for 10 min, 30 min, 8 h, and 72 h at 160°C, were investigated using 3DAP. The sample aged for 10 min at 160°C, Fig. 15(a) was statistically assessed to understand the clustering tendency between Zn and Ca/Ag atoms by performing the contingency analysis as shown in Table 5. Table 5(a-b) gives the correlation between Zn and Ca/Ag atoms where the rows and columns represent the number of Zn and Ca/Ag, respectively, in a block of 100 atoms. The χ^2 test value for the independence of the two contingency tables for Zn-Ca and Zn-Ag was 2.7 and 2.2 for 4 degree of freedom, which are lower than χ^2=13.2 for the significance level of 1%. Thus the null hypothesis that they are independent is rejected, which indicates the absence of clustering tendency between Zn-Ca and Zn-Ag atoms after aging for 10min at 160°C. The sample aged for 30 min at 160°C, showed that there were Zn rich G.P. zones, Fig. 15(b). It was also assessed statistically to test the existence of co-clustering tendency between Zn and Ca/Ag atoms, Table 6(a-b). The χ^2 test values for the independence of randomly distribution and experimentally observed categorical tables for Zn-Ca and Zn-Ag was 124.1 and 54.0 with 6 and 7 degrees of freedom, respectively. Based on this result, the probability of a random distribution is <0.1%. Since these values were lower than the specified significance level of 1%, the null hypothesis can now be rejected, indicating the co-clustering of Zn atoms with Ag and Ca atoms. The 3DAP analysis of such clusters also showed that in addition to Zn, Ag and Ca were also associated with the G.P. zones, Fig. 15(c) and their approximate compositions were ~20 at.% Zn, ~1 at.% Ag and ~1 at.% Ca, Fig. 15(d).

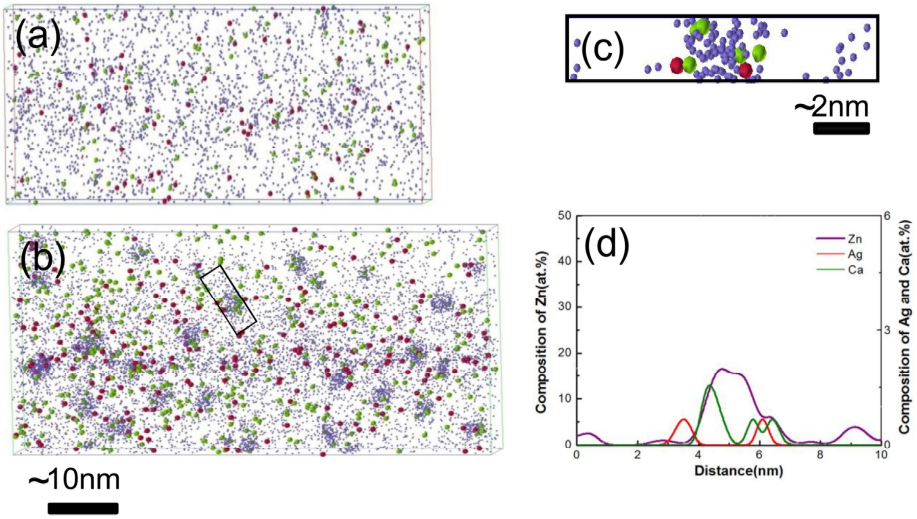

Figure 15: 3DAP map of Zn, Ag and Ca for the ZQX600 alloy aged at 160°C for (a) 10 min, (b) 30 min, (c) selected G.P. zone as marked in (b); (d) composition profile of Zn, Ag and Ca of the selected G.P. zone.

The 3DAP map of the sample aged for 8 h at 160°C shows both rod (β'_1) and plate-like precipitates (β'_2) as shown in Fig. 16(a). The concentration depth profiles were determined from the inset rectangular parallelepiped; one is from the rod-like β'_1 precipitate (Fig. 16 (b)) and the other is from the plate-like β'_2 precipitate (Fig. 16(c)). Both the rod like and plate like precipitates contains ~35 at.% Zn, ~1 at.% Ag and ~1 at.% Ca.

The peak-aged sample (72h at 160°C) also contained rod-like β'_1 and plate-like β'_2 precipitate as shown in the 3DAP map in Fig. 16(d). The approximate of the β'_1 and β'_2 precipitate is ~50 at.% Zn, ~1 at.% Ag and ~1 at.% Ca (Fig. 16(e) and (f)). This suggests that the concentration of Zn in the metastable β'_1 and β'_2 precipitates approaches the MgZn composition progressively from a lower Zn concentration.

These results have shown that the precipitation sequence of ZQX600 at 160°C can be described as

$$\alpha' \rightarrow \alpha + \text{G. P. zones} \rightarrow \alpha + \beta'_1 \rightarrow \alpha + \beta'_1 + \beta'_2 \text{ (at 160°C)}$$

Note that the G.P. zones do not form in the binary alloy at 160°C. The formation of the G.P. zones at the artificial aging temperature of 160°C is the unique feature of the microalloying of Ag and Ca in the Z6 alloy.

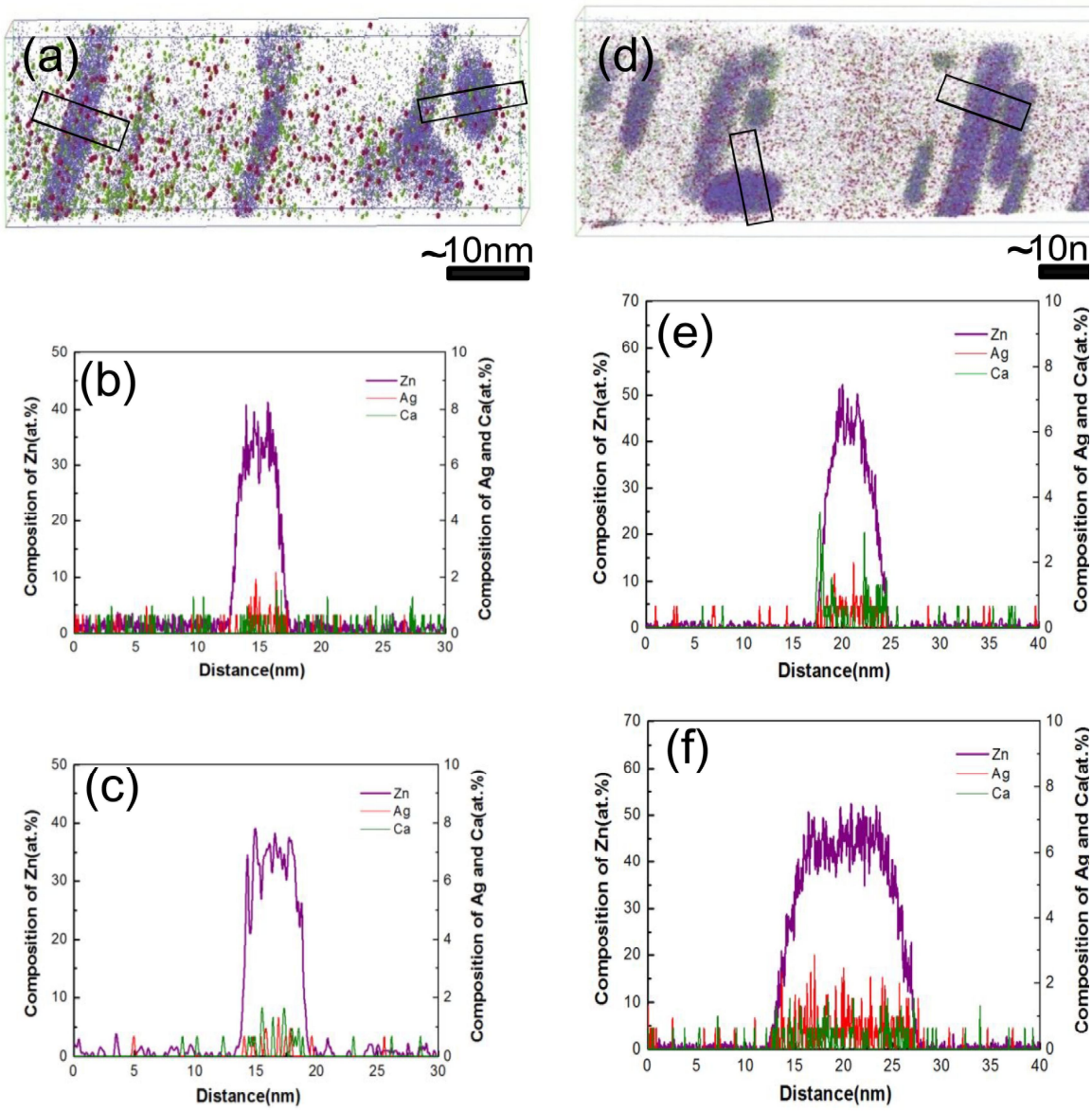

Figure 16: 3DAP map of Zn, Ca and Ag for the ZQX600 alloy aged for at 160°C for (a) 8 h, (d) 72 h (peak-aged); (b and e) shows the composition profile of Zn, Ag and Ca of a selected rod precipitate for 8 h and 72 h aged sample, respectively; (c and f) shows the composition profile of Zn, Ag and Ca of a selected plate precipitate for 8 h and 72 h aged sample respectively.

2.4. Discussion

This work has shown that the number densities of the rod-like β'_1 precipitates in Z6, ZX60, ZQ60 and ZQX600 alloys increases with increase in aging time as shown in Fig. 17. The individual microalloying of Ag and Ca with the Z6 alloy increases the number density of the β'_1 precipitates by one order of magnitude compared to the binary Z6 alloy at 160 °C at their respective peak-aged conditions. However, the combined addition of Ag and Ca increases the number density of the β'_1 precipitates substantially by two orders magnitude than that of Z6 alloy in the peak-aged condition. This is attributed to the formation of G.P. zones in the early stages of the precipitation sequence in the ZQX600 alloy, which act as heterogeneous nucleation sites for the β'_1 precipitates.

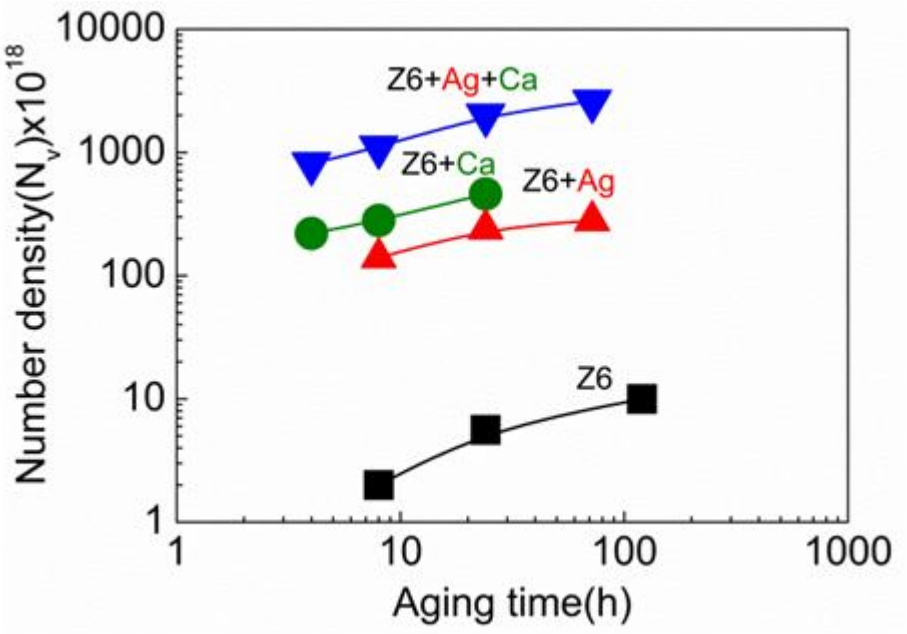

Figure 17: Variation of the number density (N_v) of the rod-like precipitates in Z6, ZX60, ZQ60 and ZQX600alloy as a function of aging time aged at 160°C.

Aging at a lower temperature of 70 °C showed Zn rich G.P. zones in the binary Z6 alloy. Although similar G.P. zones were reported in ZM61 and ZAM631 alloys [14], this is the first direct observation of the presence of G.P. zones in the binary Mg-Zn alloy. However, there had not been any reports of G.P. zone formation at 160°C, and this work showed that the combined addition of microalloying elements of Ag and Ca to the binary Mg-Zn caused the G.P. zone formation even at the elevated temperature of 160°C.

Recently a possibility of the existence of a metastable miscibility gap was reported in the Mg-Zn binary system based on thermodynamic assessment [16] but such miscibility gap in the Mg-Zn system has not been supported by other previous investigations [17, 18]. The observation of the G.P. zones in the Z6 alloy at 70°C indicates that the metastable miscibility gap or the G.P. zone solvus is slightly higher than 70°C for 2.4 at.% Zn. Therefore, the first precipitate expected for the binary alloy at 160°C is the β'_1 precipitates. However, since G.P. zones were confirmed in the early stages of aging in the ZQX600 alloy at 160°C, we can conclude that microalloying with both Ag and Ca shifts the G.P. zone solvus to a higher temperature as shown schematically in Fig. 18. The increased supersaturation and supercooling in the Ag and Ca containing alloy increase the driving force for the precipitation of the G.P. zones and subsequent β'_1 and β'_2 phases, which causes the refinement of the aged microstructure as well as the increased kinetics for precipitation as observed in Fig. 6.

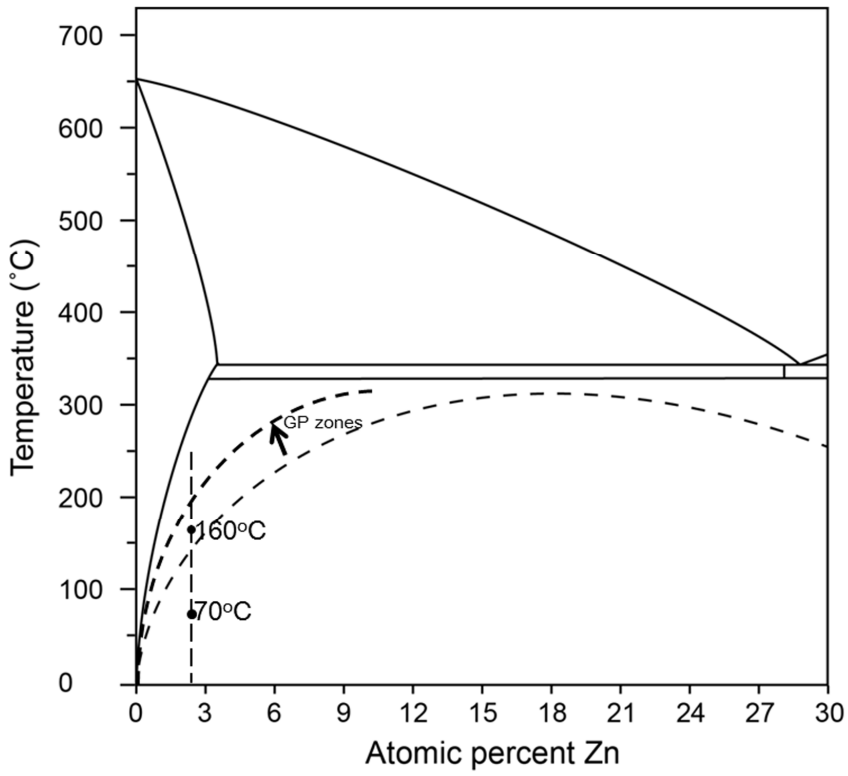

Figure 18: Mg-Zn phase diagram showing the shifting of metastable GP zone solvus to a higher temperature by combined addition of Ag and Ca. The binary diagram is based on reference [16].

The number density and size of the precipitate particles following various stages of isothermal aging at 160°C (Table 2) shows that there is no significant change in the number density or the particle size after aging for 72h or 1000h in ZQX600 alloy. Since the particle size of the main strengthening phase β'_1 remains relatively stable, we do not expect the mechanical properties of ZQX600 alloy to degrade faster. It also indicates that faster rate of nucleation does not overage the particles faster. Since there is a dense and uniform distribution of precipitates the driving force for over aging is not expected to be greater than that of the alloys not containing micro alloying additions.

Previously, we reported based on the electron microdiffraction patterns that the rod-like precipitates in the peak-aged condition at 160°C were the $MgZn_2$ phase ($P6_3/mmc$, a=0.522 nm, c=0.856 nm) [8]; however, the atom probe data from this work suggests that its composition is closer to that of the MgZn phase. The plate-like β'_2 precipitates were also found to have a composition close to 40-50 at.% and indexed according to the $MgZn_2$ phase in previous investigations [19-21]. Based on the TEM and atom probe analysis we propose that the metastable β'_1 and β'_2 phases are based on the $MgZn_2$ crystal structure; however, the composition of the phase is closer to that of MgZn. This is also consistent with our previous result where the β'_1 phase had a composition similar to MgZn in the Mg-2.4Zn-0.1Ag-0.1Ca-0.16Zr alloy [22].

2.5. Summary

G.P. zones enriched with Zn, Ag and Ca form as a precursor to β'_1 in the ZQX600 alloy at 160°C, which act as heterogeneous nucleation sites for the precipitation of β'_1 precipitates. This causes a significant increase in the number density of β'_1 precipitates, a major contributor to age hardening in the Mg-Zn based alloy, in the peak-aged condition. The composition of Zn in the G.P. zones are ~20 at.%, which increases to ~50 at.% when the zone evolves to the β'_1 and β'_2 precipitates. In the binary alloy, no G.P. zones were observed at 160°C and the β'_1 precipitates nucleated directly from the matrix without any precursor. However, the formation of the G.P. zones was also confirmed by aging the Z6 binary alloy below 70°C suggesting that the combined addition of Ag and Ca shifts the G.P. zone solvus to an elevated temperature, thereby forming G.P. zones as a precursor to β'_1 even at 160°C.

Table 1. The compositions of the alloys used in this work is summarized in both atomic and mass percent with the nomenclatures of the alloys.

nomenclature	atomic %				mass %			
	Mg	Zn	Ca	Ag	Mg	Zn	Ca	Ag
Z6	97.6	2.4	-	-	93.8	6.2	-	-
ZX60	97.5	2.4	0.1	-	93.6	6.2	0.2	-
ZQ60	97.5	2.4	-	0.1	93.4	6.2	-	0.4
ZQX600	97.4	2.4	0.1	0.1	93.2	6.2	0.2	0.4

Table 2. Quantitative microstructural measurement for rod like β'_1 precipitates observed in samples of Z6, ZX60, ZQ60 and ZQX600 at 160°C.

Alloy Condition	Number density (m^{-3})	Precipitate particle size (nm)		Aspect ratio (length/diameter)
		Length	Diameter	
Z6				
8 h	2.0×10^{18}	126.6±71.4	9.6±4.6	13
24 h	5.6×10^{18}	235.2±110.7	15.1±4.6	15
120 h (Peak aged)	1.0×10^{19}	401.9±142.2	25.3±5.2	16
ZX60				
4 h	2.2×10^{20}	83.4±43.7	7.9±1.9	10
8 h	2.8×10^{20}	85.3±33.2	8.1±2.3	10.5
24 h (Peak aged)	4.6×10^{20}	107.9±34.5	8.7±1.9	12
ZQ60				
8 h	1.4×10^{20}	245.5±111.1	7.8±1.9	31
24 h	2.4×10^{20}	287.8±77.5	10.1±2.8	28
72 h (Peak aged)	2.8×10^{20}	432.0±211.1	17.3±4.8	25
ZQX600				
2h	8.1×10^{20}	60.5±14.0	5.9±1.3	10
8h	1.1×10^{21}	62.6±21.6	6.1±1.4	11
24h	2.0×10^{21}	85.0±28.3	7.3±1.4	12
72 h (Peak aged)	2.6×10^{21}	133.5±39.5	10.5±2.7	13
1000 h (Over aged)	1.5×10^{21}	145.2±39.5	11.1±3.2	13

Table 3. Contingency table for Zn and Ca for 30 min aged condition ZX60 alloy at 160°C.

	Observed				Expected		
	Ca				Ca		
Zn	0	1-100	Total	0	1-100	Total	
0	5113	242	5355	0	5104	251	5355
1	4217	200	4417	1	4210	207	4417
2	1852	105	1957	2	1865	92	1957
3	648	33	681	3	649	32	681
4-100	213	13	226	4-100	215	11	226
Total	12043	593	12636	Total	12043	593	12636

Table 4. Contingency table for Zn and Ag for 2 h aged condition ZQ60 alloy at 160°C.

	Observed				Expected		
	Ag				Ag		
Zn	0	1-100	Total	0	1-100	Total	
0	1022	68	1090	0	1036	54	1090
1	1691	78	1769	1	1681	88	2358
2	1512	85	1597	2	1517	80	1769
3	871	44	915	3	869	46	915
4	418	22	440	4	418	22	440
5-100	246	5	251	5-100	238	13	251
Total	5760	302	6062	Total	5759	303	6062

Table 5. Contingency tables for (a) Zn and Ca and (b) Zn and Ag for 10 min aged condition ZQX600 alloy at 160°C.

(a)	Observed			Expected			
	Ca			Ca			
Zn	0	1-100	Total	0	1-100	Total	
0	1183	54	1237	0	1183	54	1237
1	1188	51	1239	1	1185	54	1239
2	722	40	762	2	729	33	762
3	333	15	348	3	333	15	348
4-100	230	7	237	4-100	227	10	237
Total	3656	167	3823	Total	3657	166	3823

(b)	Observed			Expected			
	Ag			Ag			
Zn	0	1-100	Total	0	1-100	Total	
0	1205	32	1237	0	1199	38	1237
1	1201	38	1239	1	1201	38	1239
2	736	26	762	2	738	24	762
3 -100	563	22	585	3-100	567	18	585
Total	3705	118	3823	Total	3705	118	3823

Table 6. Contingency tables for (a) Zn and Ca and (b) Zn and Ag for 30 min aged condition ZQX600 alloy at 160°C.

(a)		Observed					Expected			
		Ca					Ca			
Zn		0	1	2-100	Total		0	1	2-100	Total
	0	7454	374	13	7841	0	7406	413	22	7841
	1	8573	426	17	9016	1	8516	475	25	9016
	2	5474	262	9	5745	2	5426	303	16	5745
	3 -100	4920	412	38	5370	3-100	5072	283	15	5370
	Total	26421	1474	77	27972	Total	26420	1474	78	27972

(b)		Observed					Expected		
		Ag					Ag		
Zn		0	1-100	Total		0	1-100	Total	
	0	7628	213	7841	0	7607	234	7841	
	1	8737	279	9016	1	8747	269	9016	
	2	5605	140	5745	2	5573	172	5745	
	3	2604	87	2691	3	2611	80	2691	
	4	1114	42	1156	4	1121	35	1156	
	5	510	17	527	5	511	16	527	
	6	238	5	243	6	236	7	243	
	7-100	700	53	753	7-100	730	23	753	
	Total	27136	836	27972	Total	27136	836	27972	

2.6. References

1. L. Sturkey, J.B. Clark, J. Inst. Met. 88 (1959-1960) 177-181.
2. J.B. Clark, Acta Metall. 13 (1965) 1281-1289.
3. E.O. Hall, J. Inst. Met. 96 (1968) 21-27.
4. G. Mima, Y. Tanaka, Trans. Jap. Inst. Met. 12 (1971) 71-75.
5. G. Mima, Y. Tanaka, Trans. Jap. Inst. Met. 12 (1971) 76-81.
6. K. Hono, C.L. Mendis, T.T. Sasaki, K. Oh-ishi, Scripta Mater. 63 (2010) 710-715.
7. C.L. Mendis, K. Oh-ishi, K. Hono, Scripta Mater. 57 (2007) 485-488.
8. C.L. Mendis, K. Oh-ishi, Y. Kawamura, T. Honma, S. Kamado, K. Hono, Acta Mater. 57 (2009) 749-760.
9. C.L. Mendis, J.H. Bae, N.J. Kim, K. Hono, Scripta Mater. 64 (2011) 335-338.
10. E.E. Underwood, Quantitative stereology, Reading, MA, Addison Wesley, 1970.
11. D.B. Williams, C.B. Carter, Transmission Electron Microscopy, 2nd ed., Springer, 2009.
12. J.S. Chun, J.G. Byrne, J. Mater. Sci. 4(1969) 861-872.
13. C.J. Bettles, M.A. Gibson, K. Venkatesan, Scripta Mater. 51 (2004) 193-197.
14. K. Oh-ishi, K. Hono, K.S. Shin, Mater. Sci. Eng. A 496 (2008) 425-433.
15. M.K. Miller, Atom probe tomography, New York, Kluwer Academic, 2000.
16. C. Niu , M. Liu, C. Li, Z. Du, C. Guo, CALPHAD 34 (2010) 428-433.
17. R. Agarwal, S.G. Fries, H.L. Lukas, G. Petzow, F. Sommer, T.G. Chart, G. Effenberg, Z. Metallkd. 83 (1992) 216-223.
18. S. Wasiur-Rahman, M. Medraj, Intermetallics 17 (2009) 847-864.
19. X. Gao, J.F. Nie, Scripta Mater. 56 (2007) 645-648.
20. J. Gallot, K. Lal, R. Graf, A. Guinier, Comptes. Rendus. Acad. Sci. 258 (1964) 2818-2820.
21. J. Gallot, R. Graf, Comptes. Rendus. Acad. Sci. 261 (1965) 728-731.
22. K. Oh-ishi, C.L. Mendis, T. Honma, S. Kamado, T. Ohkubo, K. Hono, Acta Mater. 57 (2009) 5593-5604.

Chapter 3. Effect of Zr addition on the precipitation in Mg-Zn based alloy

3.1 Introduction

Magnesium alloys has received renewed interest due to its potential applications in automobiles to reduce the weight for better fuel efficiency. To satisfy the requirements for structural applications, wrought magnesium alloys with higher strength, ductility and formability have to be developed. One of the most widely used commercial alloys is the Mg-Zn based ZK60 alloy which contains a small amount of Zr in the Mg-6Zn (wt.%) alloy. ZK60 is widely used in both cast and wrought products due to its relatively high yield strength of ~260 MPa, excellent damping capacity and high mechanical stability [1]. The major reason for the microalloying of Zr in the binary Mg-6Zn alloy is to refine the grain size of cast alloys [2]. Watanabe et al. [3] reported the development of fine grained microstructure by hot working ZK60 alloy after solution treatment and overaging. They attributed the fine grained structure to the pinning of the grain boundaries by fine dispersoids of $Mg_7(Zn,Zr)_3$ that precipitate during hot working. Shahzad and Wagner [4] reported a bimodally grained structure with unrecrystallized grain stringers with 10 - 20 μm grain sizes and pockets of very fine grains of 2 – 5 μm, and attributed this to the macrosegregation of Zr with Zr-rich cores and Zr-lean rims in the cast Mg-6Zn-0.5Zr alloy. However, such micro-segregated microstructure should be homogenized by a solution heat treatment which would not provide much influence on the extruded microstructure. Using the Mg-6Zn based alloy with minor additions of Ag and Ca to enhance the precipitation hardening, Oh-ishi et al. [5] reported large differences in the extruded microstructure of the Mg-6Zn-0.4Ag-0.2Ca alloys with and without 0.6Zr (ZQX600 and ZKQX6000); they reported a bimodally grained microstructure with fine dispersion of Mg(Zn,Zr) precipitates in the extruded ZKQX6000 while a uniform grain size distribution was observed in the extruded ZQX600 alloy. While the minor addition of Zr has been considered to be useful for refining the grain size of cast ingots, fine precipitates containing Zr appear to form during hot extrusion, which substantially influence the microstructure of wrought products. The aim of this work is to characterize the nature of the fine precipitates that appear at a relatively high temperature (350°C), a typical hot extrusion and rolling temperature for ZK60, to understand the nature of the precipitates that largely influence wrought microstructures.

3.2 Experimental

Alloy ingots with a composition of Mg-6.2Zn (Z6) and Mg-6.2Zn-0.6Zr (ZK60) were prepared by induction melting with high purity Mg, Zn and Mg-34.6 wt.% Zr master alloy in an Ar atmosphere using a steel crucible and casting into a mild steel mold. The alloy compositions and their nomenclatures are shown in Table 1 in both atomic and weight percent. Samples sectioned from the ZK60 ingot were then encapsulated in Pyrex tubes partially filled with high purity He and heat treated at 350 ºC for 10 h and 100 h and quenched into water. The Z6 ingot was heat treated for 10 h and quenched into water for comparison. The alloys were also heat treated at 350ºC for 48 h followed by solution heat treatment at 400ºC for 1 h and quenched into water, following the previous work [6], and subsequently the lower temperature artificial aging was done at 160ºC for 120 h in an oil bath (T6). Transmission electron microscope (TEM) foils of all the samples were prepared by twin-jet electropolishing using a solution of 5.3 g LiCl, 11.6 g $Mg(ClO_4)_2$, 500 ml methanol and 100 ml 2-butoxy-ethanol at approximately −50°C and 90 V. The microstructure was examined on a FEI Tecnai 20 TEM operating at 200 kV. Three dimensional atom probe (3DAP) analysis was carried out with a locally built laser assisted wide angle atom probe using a femtosecond laser pulse at a wavelength of 343 nm. Square bars with dimensions of ~0.5 × 0.5 × 15 mm^3 were cut from the bulk samples and electropolished to prepare sharp needle-like specimens for atom probe analyses. The 3DAP analyses were performed in an ultrahigh-vacuum condition ($<1\times10^{-8}$ Pa) at a temperature of 25 K.

3.3 Results

Figure 1 shows the TEM bright field image of ZK60 aged at 350ºC (a) for 10 h and (b) for 100 h observed along the $<10\bar{1}0>$ zone axis. There are fine precipitates of ~35± 21 nm in length and ~8± 2 nm in width. The types of the precipitates in the sample aged for 100 h were identified with microbeam diffraction patterns (MBED). The majority of the precipitates (marked **A** in Fig. 1 (b)) are β'_1 phase with the $MgZn_2$ structure ($P6_3/mmc$, a=0.522nm, c=0.856nm) (Fig. 1 (c)) as previously reported [7,8] but no rod-like precipitates of Mg_4Zn_7 monoclinic phase as reported by Gao and Nie [9] were observed following heat treatment at 350°C. The Gibbs energy for the formation of Mg-Zn intermetallic phases was found to be similar in the temperature range investigated [10]. It is suggested that the higher aging temperature and

presence of Zr may stabilize $MgZn_2$ rather than Mg_4Zn_7 phase at 350°C. In addition, a few plate-like β'_2 precipitate as marked **B** are observed in Fig. 1 (b). The corresponding microbeam diffraction pattern along with the simulated diffraction patterns in Fig. 1 (d) indicates that the precipitate is the β'_2 phase as previously reported [7,8]. The size of the β'_1 precipitates did not change much after aging for 100 h while the number density of the precipitates increased slightly. The Zn_2Zr_3 phase observed in a Mg-1Ca-1Zn-1Zr alloy [11] was not found in the present alloy. In a recent investigation [12] on the isothermal section of Mg-Zn-Zr phase diagram at 345°C, it was shown that in alloys with high concentration of Zr compared to Zn, Zn_2Zr_3 phase is observed while in Zr lean alloys $(MgZr)_2Zn$ phase is detected. The ZK60 alloy contain very small amount of Zr compared to Zn, thus Zn_2Zr_3 phase is not expected to form during heat treatment.

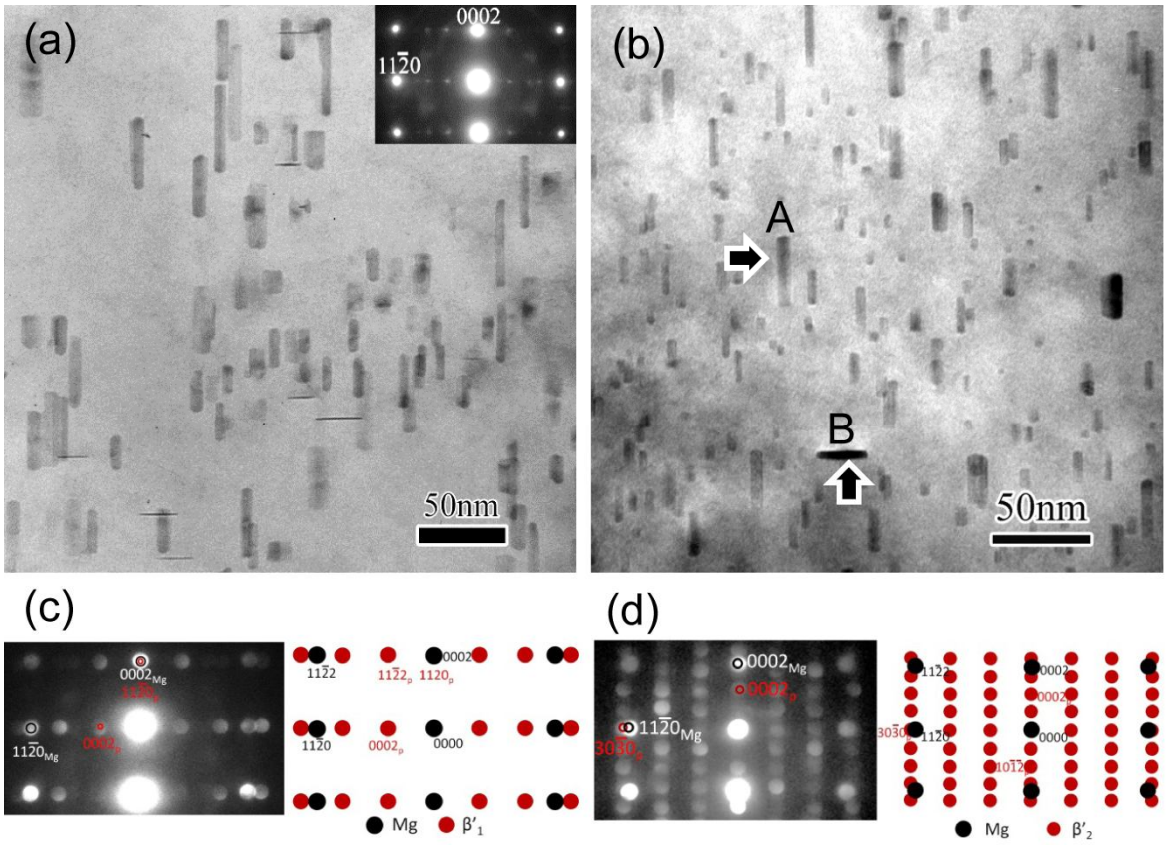

Figure 1: TEM bright field image of the 350ºC heat treated ZK60 alloy for (a) 10 h and (b) 100 h from the <10$\bar{1}$0> direction; MBED and its simulated representation of (c) β'_1 precipitate and (d) β'_2 precipitate.

The 3DAP map of Zn and Zr taken from the sample heat treated for 350ºC for 10 h is shown in Fig. 2(a). The two types of precipitates consisting mainly of the β'_1 type fine precipitates with a length of about ~20 nm and the β'_2 type precipitates marked by an arrow are observed in Fig. 2(a). One of the β'_1 type precipitates marked by a rectangle in Fig. 2(a) is enlarged and shown in Fig. 2(b). The composition profile of the selected precipitate in Fig. 2(c) clearly shows the enrichment with Zr. The composition of the precipitate was found to be ~55 at.% Mg, ~25 at.% Zn and ~20 at.% Zr close to Mg(Zn,Zr). The triangular morphology of the precipitates is due to the higher evaporation field of Zr compared to that for Mg and Zn, which causes the preferential retention of Zr atoms on the atom probe tip surface.

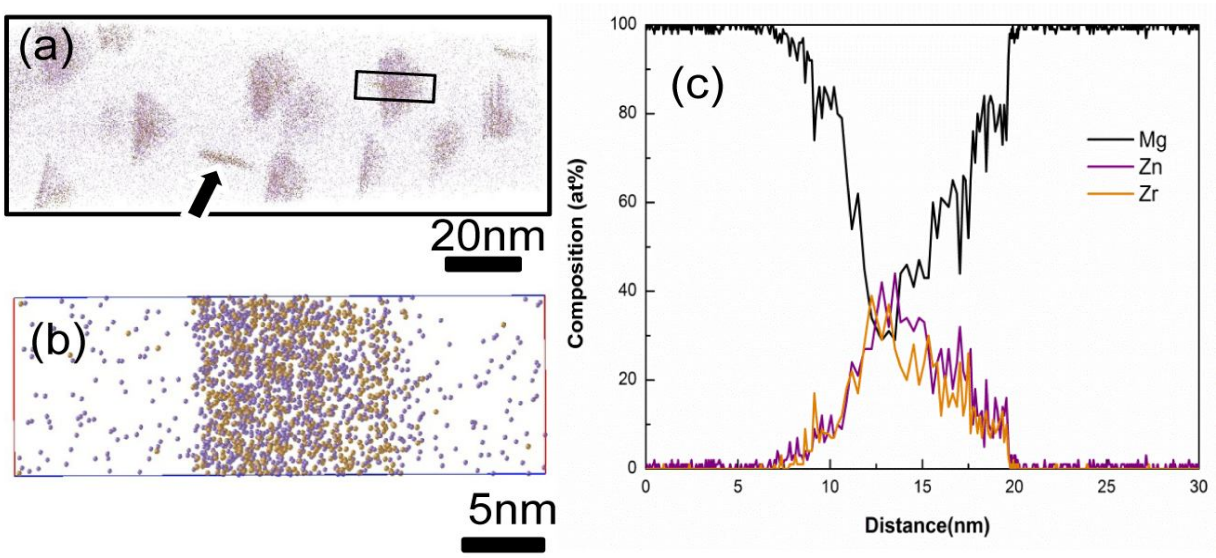

Figure 2: (a) 3DAP map of 350ºC heat treated ZK60 alloy for 10 h (b) a selected section of a β'_1 type precipitate (c) composition profile of the the selected precipitate.

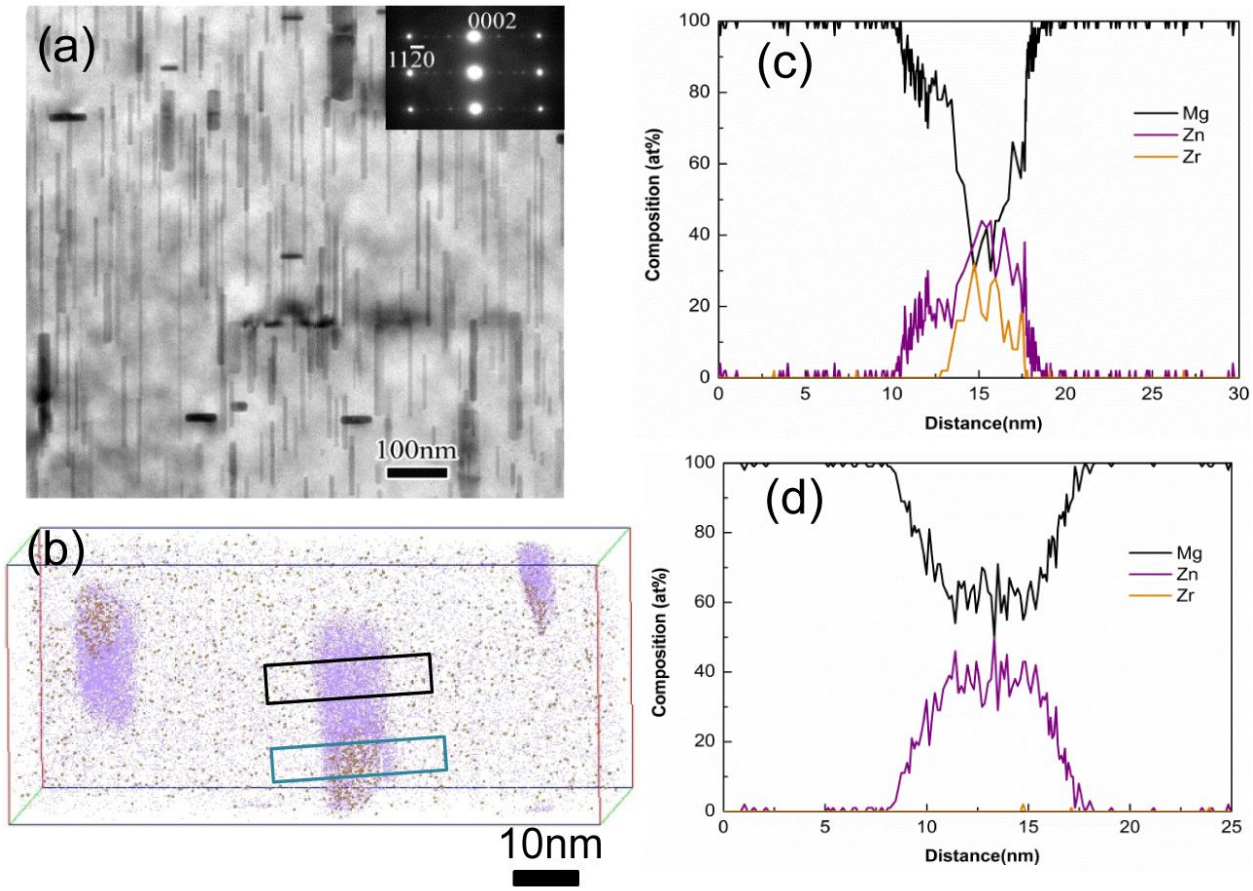

Figure 3: (a)TEM image of the low temperature aging heat treated ZK60 alloy at 160ºC for 120 h from the <10$\bar{1}$0> direction and its corresponding 3DAP map (b); (c and d) show the composition profile of the Zr and Zn rich regions of a selected β'_1 type precipitate indicated in (b) by a blue and black rectangle respectively.

To observe how the precipitation for age hardening occurs, a solution heat treated ZK60 alloy was aged at 160ºC for 120 h to get the peak aged condition as per the hardness curve from the previous report [6]. The bright field TEM image in Fig. 3(a) shows that the precipitates become rod-like, typical for the β'_1 precipitate as generally seen in Mg-Zn based alloys [13,14]. 3DAP maps of Zn and Zr atoms in Fig. 3(b) reveal that there is a Zr rich region at the beginning of the β'_1 precipitates. The composition profiles of the Zr rich and Zn rich region of the precipitates taken from the blue and black rectangles are shown in Fig. 3 (c) and (d). The approximate composition of the Zr-rich region is Mg(Zn,Zr), while that of the Zn-rich region is MgZn. The presence of such Zr rich region at one end of the Zn rich β'_1 rods suggests that the Zr-rich β'_1

particles that form at elevated temperature (350 -400°C) act as the heterogeneous nucleation sites for the β'_1 to grow in the [0001] direction. The MgZn precipitates grow to be of similar diameter as the Mg(Zn,Zr) nuclei as the two crystal structures are the same and continued growth occurs without an energy penalty. This is analogous to the θ′ plates in Al-Cu-Sn alloys having a similar thickness to the Sn rich nuclei [15]. This feature is only observed in the Zr-containing ZK60 alloy, not in the binary Z6 alloy as described below. It is noted that the number density of the Mg(Zn,Zr) precipitates after the aging at 350°C is low and do not provide sufficiently high density of nuclei to enhance the number density of precipitates in the ZK60 alloy as compared to Z6 alloy. Therefore the age hardening response and the number density of the precipitates [6] in ZK60 and Z6 alloys are similar after aging at 160°C.

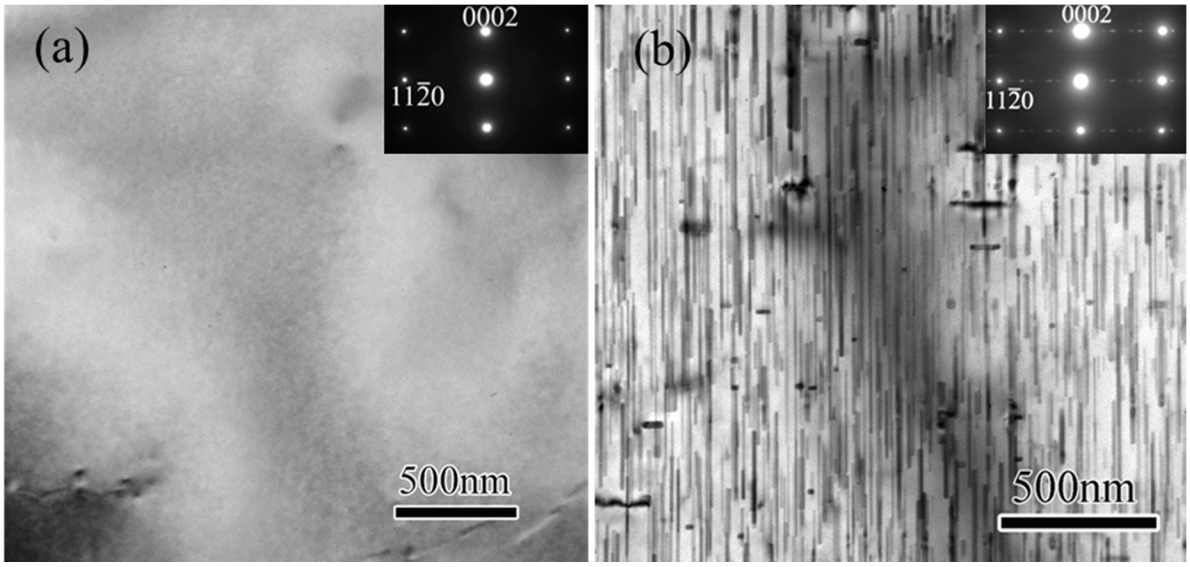

Figure 4: TEM bright field image of Z6 alloy (a) aged for 10 h at 350°C and (b) aged for 120 h at 160°C (peak aged).

Fig. 4 shows the TEM bright field image of the Z6 alloy aged for 10 h at 350°C and the one aged for 120 h at 160°C (peak aged). Neither the bright field image nor the selected area diffraction pattern taken from the Z6 sample aged at 350°C show any evidence for precipitates. This suggests that the precipitation of the β'_1 phase partitioned with Zr is unique to the Zr-containing Mg-Zn-Zr alloy. The absence of the precipitates in this condition agrees with that of the binary Mg-Zn phase diagram [16]. Therefore, we conclude that Zr stabilizes the β'_1 slightly at the elevated temperature of around 400 - 350°C. When the Z6

alloy is aged at 160°C to the peak aged condition, β'_1 and β'_2 precipitates as shown in Fig. 4 (b). A comparison of this microstructure with that of the peak aged ZK60 (Fig. 3 (a)) indicates that the Zr addition does not alter the precipitate phases and their morphologies. The only effect that the Zr addition has is to stabilize the β'_1 phase at the elevated temperature by partitioning in it.

3.4 Discussion

The above results indicate that the Zr in Mg alloys, along with its role as a grain refiner [17,18], has the additional role of stabilizing the metastable β'_1 $MgZn_2$ phase when heat treated at an elevated temperature. Homma et al. [19] suggested the possibility of Zr acting as a microalloying element in a heat treated and extruded Mg-6Zn-0.2Ca-0.8Zr (wt.%) (ZKX610) alloy. They reported that the β'_1 $MgZn_2$ phase has a Ca and Zr association. Oh-ishi et al. [5] also found a similar type of fine precipitates associated with Zr and Ca in a homogenized and extruded ZKQX6000 alloy. They also reported that the Mg(Zn,Zr) precipitates that form during extrusion are dissolved by the solution heat treatment (T4). Then β'_1 precipitates without Zr appear by the subsequent artificial aging at 160°C, which increase the yield strength. The present study indicates that such fine precipitates also appear in a ternary ZK60 alloy when heat treated at 350ºC. This is a feature of the Mg-Zn-Zr ternary system, not of the ZKQX quinary system. The importance of the presence of such Zr containing β'_1 for the microstructure development during extrusion and hot rolling by dynamic recrystallization has long been overlooked but this work together with the previous investigations on the extruded microstructure of ZKQX6000 alloy [5] indicate that micoralloyed Zr plays a critical role in the microstructure evolution that involves dynamic precipitation and recrystallization.

Note that only the β'_1 formed at an elevated temperature (350°C) contains Zr although the structure of the phase is exactly the same as the β'_1 formed at an artificial aging temperature (160°C). Since the structure of the Zr-containing and Zr-free β'_1 is the same, the β'_1 rods grow from the Zr-containing β'_1 as nuclei at low temperature. However, since the diffusivity of Zr is thought to be sluggish at 160°C, the β'_1 that grows at 160°C does not contain Zr. Thus, the β'_1 growth at low temperature is similar to the para-equilibrium growth of cementite observed in Fe-C-Mn steels in which the diffusivities of C and Mn are orders of magnitude different [20].

3.5 Summary

In summary, the microstructural studies show that heat treatment of the ZK60 alloy at 350ºC for 10 h or longer leads to the precipitation of very fine particles of the order of ~20 nm with the β'_1 $MgZn_2$ type structure, whereas the Z6 alloy is completely solution treated. On lower temperature aging of the ZK60 alloy at 160ºC for 120 h, the the β'_1 precipitates grow in the [0001] direction without Zr partitioning. Thus, the Zr is partitioned only one end of the β'_1 rods. The β'_1 stabilized with the partitioning of Zr play critical role in the development of recrystallized microstructure in wrought alloys.

Table 1.The compositions and the nomenclatures of the alloys used in this work

nomenclature	atomic %			mass %		
	Mg	Zn	Zr	Mg	Zn	Zr
Z6	97.6	2.4	-	93.8	6.2	-
ZK60	97.4	2.4	0.2	93.2	6.2	0.6

3.6 References

1. M. M. Avedesian, H. Baker (Eds.). Magnesium and magnesium alloys ASM International Materials Park, OH: 1999.
2. E. F. Emley, Principles of Magnesium Technology, Pergamon press, Oxford 1966.
3. H. Watanabe, K. Moriwaki, T. Mukai, T.Ohsuna, K. Hiraga, K. Higashi, Mater. Trans. 44 (2003) 775.
4. M. Shahzad, L. Wagner, Scripta Mater. 60 (2009) 536.
5. K. Oh-ishi, C. L. Mendis, T. Homma, S. Kamado, T. Ohkubo, K. Hono, Acta Mater. 57 (2009) 5593.
6. C. L. Mendis, K. Oh-ishi, Y. Kawamura, T. Honma, S. Kamado, K. Hono, Acta Mater. 57 (2009) 749.
7. J. Gallot, K. Lal, R. Graf, A. Guinier, Comptes. Rendus. Acad. Sci. 258 (1964) 2818.
8. J. Gallot, R. Graf. Comptes. Rendus. Acad. Sci. 261 (1965) 728.
9. X. Gao, J.F. Nie, Scripta Mater. 56 (2007) 645.
10. M. Morishita, H. Yamamoto, S. Shikada, M. Kusumoto, Y. Matsumoto, Acta Mater. 54 (2006) 3151.
11. X. Gao, B.C. Muddle, J.F. Nie, Phil. Mag. Lett. 89 (2009) 33.
12. Y.P. Ren, Y. Guo, D.Chen, S. Li, W.L. Pei, G.W. Qin, CALPHAD 35 (2011) 411.
13. C. J. Beetles, M. A. Gibson, K. Venkatesan, Scripta Mater. 51 (2004) 193.
14. C. L. Mendis, K. Oh-ishi, K. Hono, Scripta Mater. 57 (2007) 485.
15. L. Bourgeois, J.F. Nie, B.C. Muddle, Phil. Mag. 85 (2005) 3487.
16. A. A. Nayeb-Hashemi, J. B. Clark (Eds.), Phase diagrams of binary magnesium alloys, ASM International (1988) 353.
17. C. S. Roberts, Magnesium and its Alloys, Wiley, New York, 1960.
18. Y. C. Lee, A. K. Dahle, D. H. StJohn, Metall. Mater. Trans. A 31 (2000) 2895.
19. T. Homma, C.L. Mendis, K. Hono, S. Kamado, Mater. Sci. Eng. A 527 (2010) 2356.
20. S. S. Babu, K. Hono, T. Sakurai, Metall. Mater. Trans. A, 44 (1994) 499.

Chapter 4. Effect of Zr on the microstructure and mechanical properties of an extruded Mg-6.2Zn alloy

4.1 Introduction

The importance of the use of light weight alloys with high specific strength in the transportation sector which contribute to reduce the CO_2 emissions have led to the renewed interest in magnesium alloys in recent years. Since magnesium has a hexagonal close packed structure with few slip systems, it makes deformation processes difficult at room temperature. Recently, addition of rare earth elements to magnesium have been shown to have a beneficial effect on the deformation behavior as well as in increasing the ductility of the magnesium alloys [1]. Since rare earth elements are costly we need to focus on the low cost systems such as Mg-Al, Mg-Zn and Mg-Ca systems. Among the low cost magnesium alloys Mg-Zn system which generally shows low age hardening response, has shown enhanced age hardening characteristics upon additions of Ag and Ca [2-6]. Mg-Zn based ZK60 alloy has also been used for industrial applications. The role of Zr as a grain refiner is well known in cast Mg-Zn alloys [7]. Recent report by Oh-ishi et al. showed large differences in the extruded microstructure of the Mg-6Zn-0.4Ag-0.2Ca alloys with and without 0.6Zr (ZQX600 and ZKQX6000) [8]. The ZKQX6000 had a bimodally grained microstructure with fine dispersion of Mg(Zn,Zr) precipitates whereas ZQX600 alloy had a uniform grain size distribution. The ZQX600 alloy in the above work contained Ag and Ca, but without any Zr it showed an extruded tensile yield strength of only 153 MPa whereas the Zr containing ZKQX6000 alloy showed an extruded tensile yield strength of 289 MPa. The above result shows that the addition of Zr is playing a major role in the increment of tensile strength of Mg-Zn system compared to addition of Ag and Ca. More, recently it has been found that these Mg(Zn,Zr) precipitates are formed in a heat treated cast ZK60 alloy without Ag and Ca [9]. Therefore we performed an extrusion of a Mg-6.2Zn-0.6Zr (ZK60) alloy without Ca and expensive Ag with an aim to show the effect of the Mg(Zn,Zr) precipitates on the mechanical properties and recrystallization behavior by comparing it with an binary Mg-6.2 wt.%Zn (Z6) extruded alloy.

4.2 Experimental

Alloy ingots with a composition of Mg-6.2Zn (Z6) and Mg-6.2Zn-0.6Zr (ZK60) were prepared by

induction melting with high purity Mg, Zn and Mg-34.6 wt.% Zr master alloy in an Ar atmosphere using a steel crucible and casting into a mild steel mold. The alloy compositions and their nomenclatures are shown in Table 1 in both atomic and weight percent. The ingots were homogenized at 350ºC for 48 h and then extruded at 350ºC with an extrusion ratio of 20:1 and a ram speed of 0.1mm s^{-1}. The extruded bar samples were heat treated at 400ºC for 1 h and quenched into water (T4), and artificially aged at 160ºC in an oil bath (T6). Tensile tests of the as extruded and T6 heat-treated samples were conducted at room temperature at an initial strain rate of 1×10^{-3} s^{-1}. Electron back scattered diffraction (EBSD) analyses were carried out by using Carl Zeiss CrossBeam 1540EsB field-emission scanning electron microscope equipped with a HKL EBSD detector. Transmission electron microscope (TEM) foils of all the samples were prepared by twin-jet electropolishing using a solution of 5.3 g LiCl, 11.6 g $Mg(ClO_4)_2$, 500 ml methanol and 100 ml 2-butoxy-ethanol at approximately −50°C and 90 V. The specimens were surface cleaned by ion milling using a Gatan Precision ion Polishing System (PIPS) at an operating voltage of 2kV. The microstructure was examined on a FEI Tecnai 20 TEM operating at 200 kV.

4.3 Results

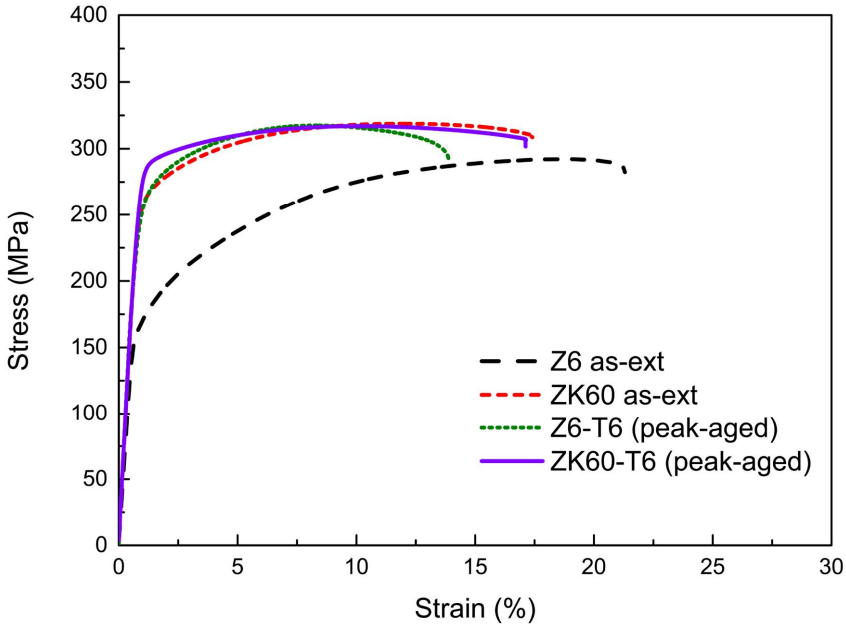

Figure 1: Tensile stress-strain curves of Z6 and ZK60 in as-extruded condition and T6 (peak-aged) condition.

Figure 1 shows the tensile stress strain curves of the Z6 and ZK60 alloys in as-extruded and peak-aged. The Z6 and ZK60 alloys reach their peak hardness after 72 h of aging at 160°C (not shown). The as-extruded Z6 alloy shows a yield strength (0.2% offset strength), σ_{ys} of 162 MPa, ultimate tensile strength, σ_{uts} of 290 MPa with an elongation to failure of 21.0%. ZK60 alloy shows a σ_{ys} of 254 MPa, σ_{uts} of 318 MPa in the as-extruded condition with an elongation to failure of 17.3%. Thus there is a difference of 92 MPa between σ_{ys} of Z6 and ZK60 alloys in as-extruded condition. Upon T6 treatment, Z6 alloy shows a σ_{ys} of 244 MPa and σ_{uts} of 317 MPa with an elongation to failure of 13.8%. T6 treated ZK60 alloy showed a σ_{ys} of 275MPa with a σ_{uts} of 318 MPa and had an elongation to failure of 17.1%. Thus even in the T6 treated ZK60

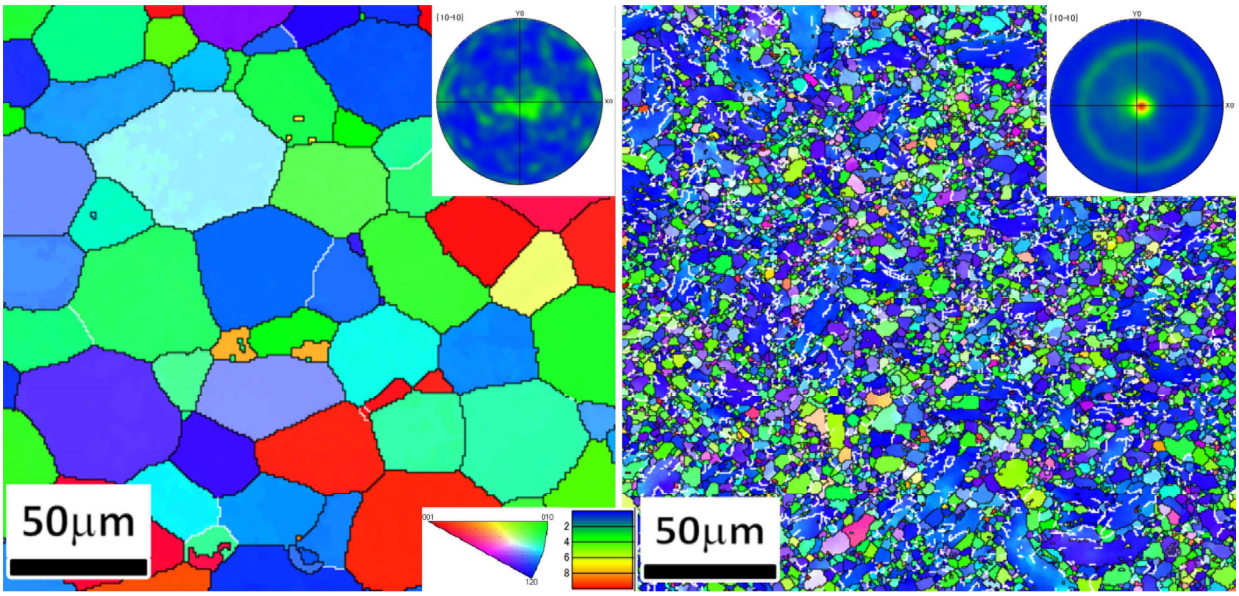

Figure 2: EBSD map of as-extruded (a) Z6 and (b) ZK60 alloy. The observed plane is normal to extrusion direction.

alloy shows better yield strength compared to Z6 alloy.

Figure 2 shows the inverse pole figure (IPF) maps of the Z6 and ZK60 alloy in the as-extruded condition from the surface perpendicular to the extrusion direction (ED). The black lines indicates grain boundaries having misorientation greater than 15° and the white lines represents the sub-grain boundaries between 5-15°. Z6 alloy shows equiaxed dynamically recrystallized grains of size 36.0 ± 10.0 μm (Fig. 2(a))

whereas ZK60 alloy shows bimodal microstrcucture. ZK60 alloy consists of fine dynamically recrystallized grains of 3.2 ± 1.0 μm along with unrecrystallized grains of 40-50 μm (Fig. 2(b)). In the unrecrystallized regions lot of sub-grain boundaries are also observed. The $\{10\bar{1}0\}$ pole figure has a weaker intensity in the Z6 alloy whereas in the ZK60 alloy it has a stronger intensity (Fig. 2(a) and (b)). This can be attributed to the presence of the unrecrystallized grains in the ZK60 alloy which have a strong basal texture along the ED.

Figure 3 shows the bright field TEM images of Z6 and ZK60 alloy in the as-extruded condition. Z6 alloy did not show any fine precipitates inside the grains (Fig. 3(a)), whereas ZK60 alloy showed a fine dispersion of precipitates in the matrix as well as along the grain boundaries (Fig. 3(b)). Some of the precipitates along the grain boundary are marked by black arrows. The sizes of the precipitates were 48.9 ± 25.8 nm in length and 11.6 ± 5.6 nm in width. Similar precipitates were also reported in a heat treated cast ZK60 alloy in our previous work which are the Zr-rich Mg(Zn,Zr) precipitates [9].

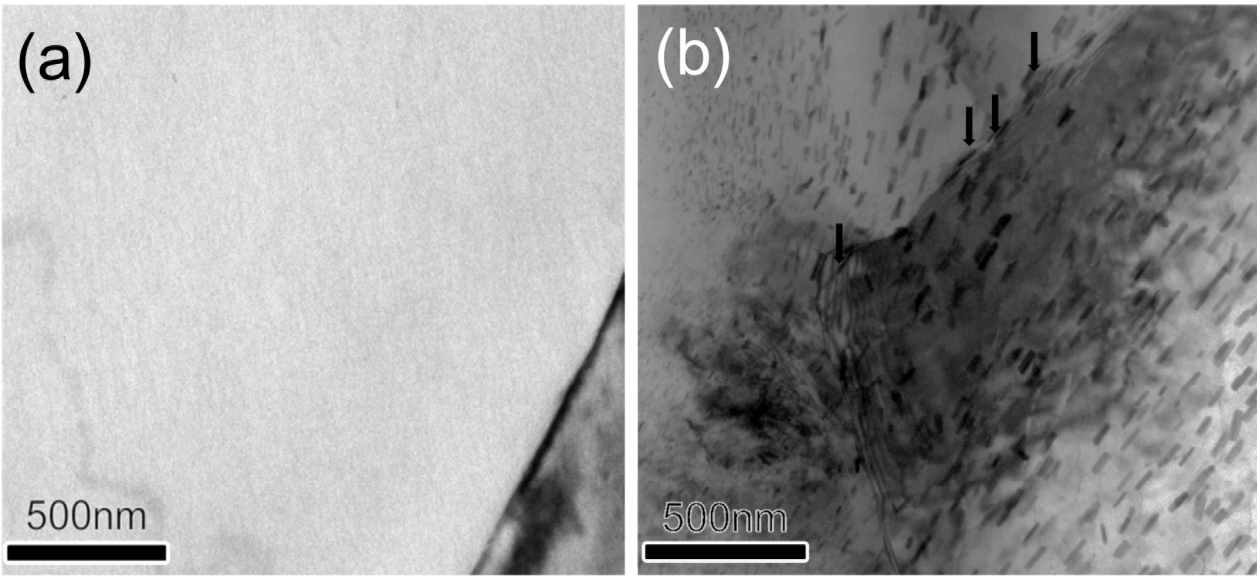

Figure 3: Bright field TEM images of as-extruded (a) Z6 and (b) ZK60 alloy.

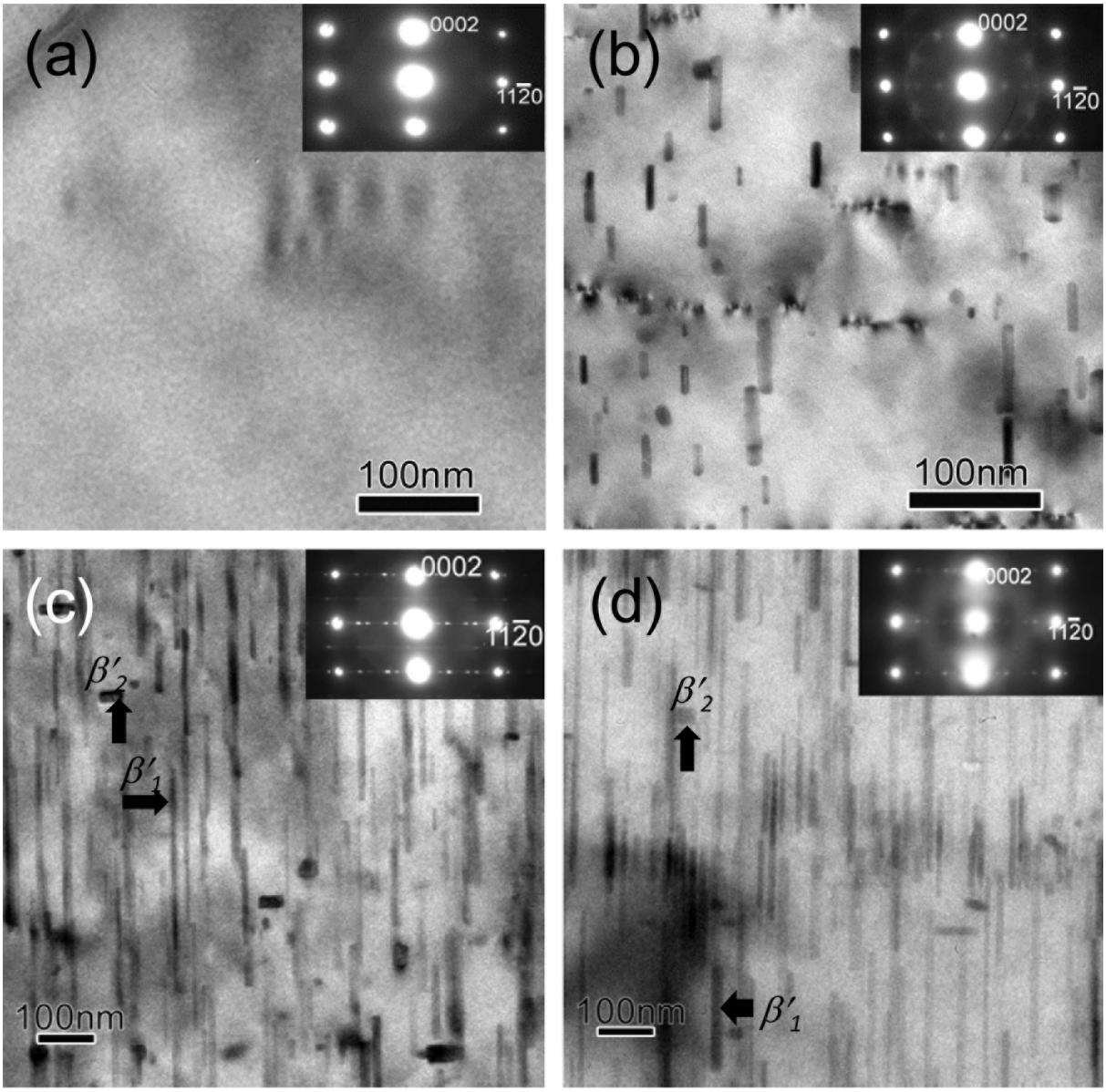

Figure 4: Bright field TEM bright field image of T4- treated (a) Z6 alloy (b) ZK60 alloy; peak-aged (c) Z6 alloy (d) ZK60 alloy.

Figure 4 (a-d) shows the TEM bright field images of the Z6 and ZK60 alloys aged in the T4-treated and T6-treated (peak-aged) condition. T4-treated Z6 alloy did not show any evidence for precipitates (Fig. 4(a)) whereas ZK60 alloy shows fine Mg(Zn,Zr) precipitates (Fig. 4(b)) similar to that present in the as-extruded condition. Therefore, we can conclude that Zr stabilizes these fine precipitates even at the elevated temperature of 400°C. Upon artificial aging at 160°C for 72 h (peak-aged condition), rod-like β'_1

and plate-like β'_2 precipitates form in both Z6 and ZK60 alloy as shown in Fig. 4 (c,d). The β'_1 precipitates grow along the [0001] direction of the matrix from the Mg(Zn,Zr) precipitates as they have same $MgZn_2$ -type crystal structure ($P6_3/mmc$, a=0.522nm, c=0.856nm) [9]. The selected area electron diffraction (SAED) patterns indicate that the β'_1 precipitates have an orientation relationship of $(0001)\,\beta'_1 // (11\bar{2}0)_{Mg}$ and $[11\bar{2}0]\,\beta'_1 // [0001]_{Mg}$ and the plate-like β'_2 precipitates have an orientation relationship of $(0001)\,\beta'_2 // (0001)_{Mg}$ and $[11\bar{2}0]\,\beta'_2 // [10\bar{1}0]_{Mg}$ as previously reported [8,10]. The addition of Zr to Z6 alloy did not alter the precipitate phases and their morphologies in the peak- aged condition.

4.4 Discussion

The above results show that in the as-extruded condition there is a difference of greater than 90 MPa in the tensile yield strength between Z6 and ZK60 alloy. As seen from Fig. 2(a) and (b) that there are coarse equiaxed grains in Z6 alloy whereas in ZK60 alloy it consists of fine recrystallized grains as well as unrecrystallized grains. The unrecrystallized grains having a strong basal texture along the ED tend to have higher resistance against yielding during tensile test [11]. Thus the bimodal microstructure in ZK60 alloy gives rise to its higher tensile strength compared to Z6 alloy in the as-extruded condition. Bright field TEM micrographs shows that there are fine Mg(Zn,Zr) precipitate present in the extruded state of ZK60 alloy. Previous work reported the presence of these precipitates in a heat treated cast ZK60 alloy at 350ºC [9]. Since these precipitates are present before extrusion they tend to affect the flow behavior of ZK60 alloy while being extruded by pinning dislocation and promoting sub-grain formation in the interior of the grains. This can be seen by the formation of unrecrystallized grains in the microstructure which have misorientation of less than 15 º marked by white lines in Fig. 2(b). These precipitates also tend to prevent grain growth of the recrystallized grains [8]. This gives rise to their characteristic bimodal microstructure. Although earlier work by Doan and Ansel reported fine grain microstructure in an extruded ZK60 alloy but it had not been linked due to presence of fine precipitates [12]. Some recent works linked the bimodal microstructure to the presence of fine precipitates but since the alloys in those works also contained Ca and Ag along with Mg-Zn-Zr alloy, there was an association of Ca with the fine Mg(Zn,Zr) precipitates [8,11]. Therefore the

significance of this work is that it confirms that Zr is main element for the formation of these precipitates which are playing a major role in the recrystallization behavior and tensile strength increment. Upon peak aging at 160ºC, tensile yield strength further increases to 275 MPa in the ZK60 alloy due to the increase in the aspect ratio of the β'_1 precipitates compared to the Mg(Zn,Zr) precipitates in the as-extruded condition.

The role of Zr in recrystallization behavior is very significant for the high yield strength as seen from this work and previous works by Oh-ishi et al. and Homma et al. [8,11]. Homma et al. reported that their extruded Mg-6.6Zn-0.19Ca (ZX) alloy has only a tensile yield strength of 148 MPa whereas Oh-ishi et al. reported an extruded tensile yield strength of 153 MPa in their ZQX600 alloy. The extruded Z6 alloy in the present work also shows similar tensile yield strength of 162 MPa. These results show that addition of Ag and Ca without Zr to binary Mg-Zn alloy is not effective in increasing the as-extruded tensile yield strength. The addition of Zr is very important for the stabilization of the $MgZn_2$ precipitates by incorporation of Zr which helps to attain the tensile yield strength of above 250 MPa in Mg-Zn-Zr systems. Once these Mg(Zn,Zr) precipitates are stabilized, only then the effect of Ca and Ag for the refinement of these precipitates is effective to further increase the strength of ZK60 alloy in the as-extruded condition.

4.5 Summary

In summary, the microstructural studies show that extruded as well as T4 treated ZK60 alloy shows fine Mg(Zn,Zr) precipitates whereas the Z6 alloy does not show fine precipitates. The addition of Zr play a critical role in stabilization of Mg(Zn,Zr) precipitates giving rise to the bimodal microstructure in the ZK60 alloy and the corresponding difference of 92 MPa in the tensile yield strength in the as-extruded condition compared to Z6 alloy. On peak aging of the ZK60 alloy at 160ºC for 72 h, a tensile yield strength of 275 MPa can be obtained due to the increase in the aspect ratio of the β'_1 precipitates compared to the Mg(Zn,Zr) precipitates in the as-extruded condition.

Table 1.The compositions and the nomenclatures of the alloys used in this work

nomenclature	atomic %	mass %
Z6	Mg-2.4Zn-	Mg-6.2Zn
ZK60	Mg-2.4Zn-0.16Zr	Mg-6.2Zn-0.6Zr-

4.6 References

1. N. Stanford, M. R. Barnett, Mater. Sci. Eng. A 496 (2008) 399.
2. L Sturkey, J. B. Clark, J. Inst. Met. 88 (1959) 177.
3. J. B. Clark, Acta Met. 13 (1965) 1281.
4. G. Mima, Y. Tanaka, Trans. Jap. Inst. Met. 12 (1971) 71.
5. G. Mima, Y. Tanaka, Trans. Jap. Inst. Met. 12 (1971) 76.
6. C. L. Mendis, K. Oh-ishi, K. Hono, Scripta Mater. 57 (2007) 485.
7. C. S. Roberts, Magnesium and its Alloys, Wiley, New York, 1960.
8. K. Oh-ishi, C. L. Mendis, T. Homma, S. Kamado, T. Ohkubo, K. Hono, Acta Mater. 57 (2009) 5593.
9. T. Bhattacharjee, C. L. Mendis, T. T. Sasaki, T. Ohkubo, K. Hono, Scripta Mater. 67 (2012) 967.
10. J. Gallot, R. Graf, Comptes. Rendus. Acad. Sci. 261 (1965) 728.
11. T. Homma, C.L. Mendis, K. Hono, S. Kamado, Mater. Sci. Eng. A 527 (2010) 2356.
12. J. P. Doan, G. Ansel, Trans. AIME 171 (1947) 286**.**

Chapter 5. Effect of Zr, Ca and Ag on the mechanical properties and texture of twin roll cast- hot

rolled Mg-Zn alloys.

5.1 Introduction

The use of light weight magnesium alloys as structural materials in the transportation sector is considered to be effective in improving fuel efficiency by weight reduction. The main barrier for the application of the wrought magnesium alloys is their limited room temperature formability. Recent investigation has shown that alloying with rare earth elements improves the formability by weakening the basal texture [1]. The next challenge is to develop low-cost high strength and formable wrought magnesium alloys by avoiding expensive rare earth metals. Among various rare earth free magnesium alloys, Mg-Zn based alloys are very promising for its good age hardening characteristics [2-6]. Mendis et al. reported high yield strength over 300 MPa in T6 aged Mg-6.1Zn-0.4Ag-0.2Ca-0.6Zr (wt.%) alloy (ZKQX6000) in the form of extruded bar and twin roll cast and hot rolled sheet [7,8]. The twin roll cast and hot rolled (TRC-HR) ZKQX6000 alloy sheets exhibited an excellent formability in the T4 condition, a high yield strength (σ_{ys}) of 320 MPa and an ultimate tensile strength (σ_{uts}) of ~342 MPa with an elongation to failure (ε_f) of 17% after an artificial aging (T6), which was expected to open up a possibility for the development of heat treatable wrought magnesium based alloy [8]. The T4 and T6 treated ZKQX alloys contain fine Mg(Zn,Zr) precipitates, which control the microstructure during wrought processing [7,9]. Our recent investigation has shown that the same precipitates can be observed in the T4 and T6 treated Mg-6.2Zn-0.6Zr or ZK60 alloy [10]. However, the formability appears to be improved by the addition of Ca to the binary Mg-Zn alloy [11]. Since the understanding of the role of individual alloying elements is important for alloy development, we investigated the microstructure and mechanical properties of twin roll cast and hot rolled (TRC-HR) Mg-6.2Zn (wt.%) (Z6), Mg-6.2Zn-0.5Zr (wt.%) (ZK60), Mg-6.2Zn-0.5Zr-0.2Ca (wt.%) (ZKX600) and Mg-6.2Zn-0.5Zr-0.4Ag-0.2Ca (wt.%) (ZKQX6000) alloys in order to understand the effect of individual microalloying elements.

5.2 Experimental

Alloy ingots with nominal compositions (in wt.%) of Mg-6.2Zn (Z6), Mg-6.2Zn-0.5Zr (ZK60), Mg-6.2Zn-0.5Zr-0.2Ca (ZKX600) and Mg-6.2Zn-0.5Zr-0.4Ag-0.2Ca (ZKQX6000) were prepared by induction melting in an argon atmosphere using a steel crucible. Table 1 summarizes the chemical compositions of these alloys in wt.% and at.%. The ingots were then remelted under a mixture of CO_2 and SF_6 and transferred into a preheated tundish held at 680–700 °C followed by twin roll casting. The roll gap was set at 1.8 mm and roll speed was 4 m/min. The cast sheets were then homogenized at 330 °C for 2 h and then hot rolled at 300 °C for three passes with a total reduction of 50%. The rolled sheet samples were then heat-treated at 400 °C for 30 min and quenched into cold water (T4) and finally aged at 160 °C for 0.5 to 1000 h in a silicone oil bath. The Vickers hardness was measured for all the samples with 10 individual indentations with a 0.5 kg load. Tensile properties were measured using flat tensile specimens with a gauge length of 12.5 mm, gauge thickness of 1 mm and gauge width of 5 mm at a strain rate of 6.4×10^{-4} s^{-1} along the rolling direction (RD). Stretch formability was evaluated by the limiting dome height (LDH) value obtained by the Erichsen cupping test (square-shaped specimen of size 50 mm × 50mm). The punch diameter and speed used were 20 mm and 0.1 mm s^{-1} respectively. Silicone oil was used as a lubricant. The crystallographic macrotexture of the alloys were analyzed on the midsection of the specimens by X-ray diffraction (XRD) using Cu Kα radiation with a measuring grid of 5° × 5° in both polar and azimuthal rotations of the specimen to a maximum tilt of 90º. The pole figure data analyses were done by using Labotex 3.0 software. Microstructure observations were performed using optical microscope (OM), electron back scattered diffraction (EBSD), transmission electron microscope (TEM) and three dimensional atom probe (3DAP). EBSD was carried out by using Carl Zeiss CrossBeam 1540EsB field-emission scanning electron microscope equipped with a HKL EBSD detector along the normal direction-rolling direction (ND-RD) plane of the samples. EBSD data analyses were performed using TSL OIM 7.0 software. TEM observations were conducted using FEI Tecnai T20 and Titan G^2 80-200 microscopes operating at 200 kV. TEM specimens were prepared using twin jet electro-polishing using a solution of 300 ml 2-butoxy ethanol, 15.9 g lithium chloride, 33.5 g of magnesium perchlorate in 1500 ml methanol at a temperature of ~ -45°C as well as ion-polishing using Gatan Precision Ion Polishing System (PIPS). Three dimensional atom probe

(3DAP) analyses were carried out with a locally built laser assisted wide angle atom probe using a femtosecond laser pulse at a wavelength of 343 nm [12]. Square bars with dimensions of ~0.5 × 0.5 × 15 mm^3 were cut from the bulk samples and electropolished to prepare sharp needle-like specimens for atom probe analyses. The 3DAP analyses were performed in an ultrahigh-vacuum condition (<1×10^{-8} Pa) at a temperature of 25 K.

5.3 Results

Figure 1 shows the variation in Vickers hardness values as a function of aging time. The as-rolled hardness of Z6 alloy is 75 ± 1 HV whereas ZK60, ZKX600 and ZKQX6000 alloys has the as-rolled hardness of 90 ± 2 HV. After a T4 treatment at 400°C for 30 min, the hardness decreases to 53 ± 1 HV for Z6 alloy, 65 ± 1 HV for ZK60 alloy, 66 ± 1 HV for ZKX600 alloy and 71 ± 1 HV for ZKQX6000 alloy. Upon artificial aging at 160ºC, the hardness starts to increase after 30 min of aging and all the alloys reach their peak hardness values at an aging time of 24 h. The peak-aged values are around 75 ± 2 HV for Z6 alloy, 80 ± 2 HV for ZK60 alloy, 83 ± 2 HV for ZKX600 alloy, and 89 ± 2 HV for ZKQX6000 alloy.

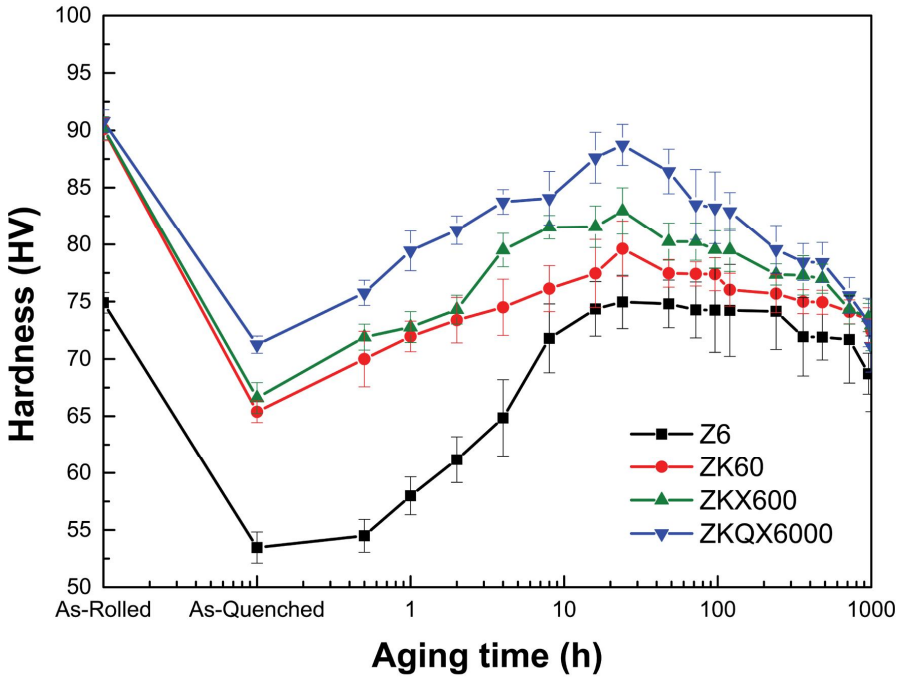

Figure 1: The age hardening response of the Z6, ZK60, ZKX600 and ZKQX6000 alloy at 160°C.

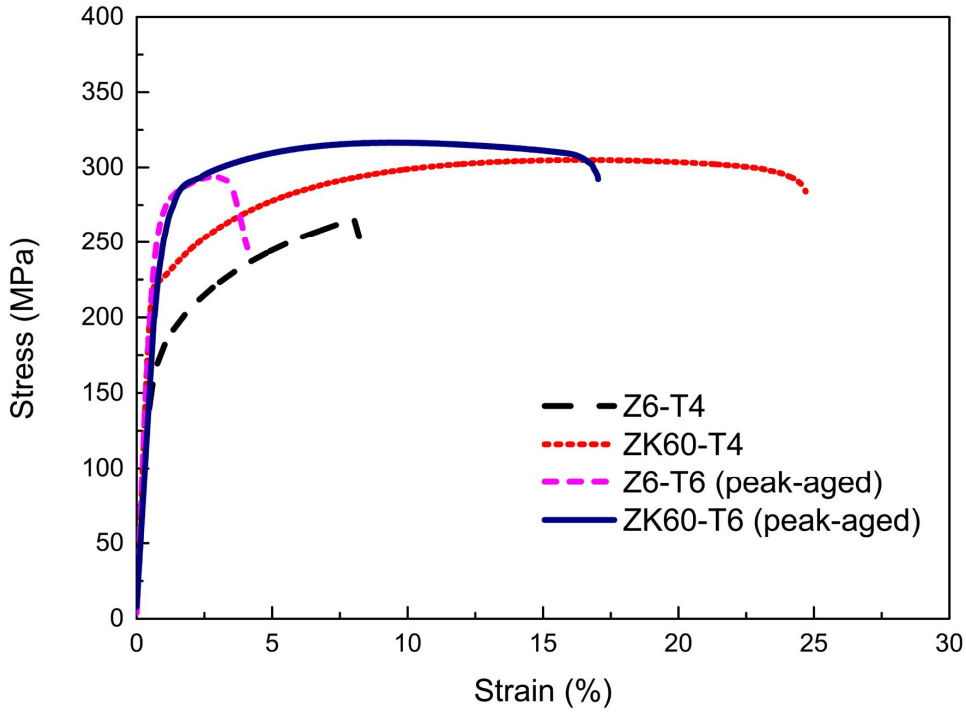

Figure 2: Tensile stress-strain curves of Z6 and ZK60 at T4 condition (400ºC for 30min) and T6 (peak-aged) condition.

Figure 2 shows the tensile stress–strain curves of Z6 and ZK60 alloys in T4 and peak-aged conditions. Table 2 summarizes the tensile properties of all the alloys in the present investigation. The T4 treated Z6 alloy shows a yield strength (0.2% offset strength), $\sigma_{ys,}$ of 163 MPa with elongation to failure of 8.2%. Upon peak aging, σ_{ys} of the Z6 alloy increases to 246 MPa at an expense of elongation to failure, 4.2%. ZK60 alloy shows a σ_{ys} of 220 MPa in the T4 condition with elongation to failure of 24.0%. Upon peak aging, σ_{ys} increased to 270 MPa and has an elongation to failure of 17.0%.

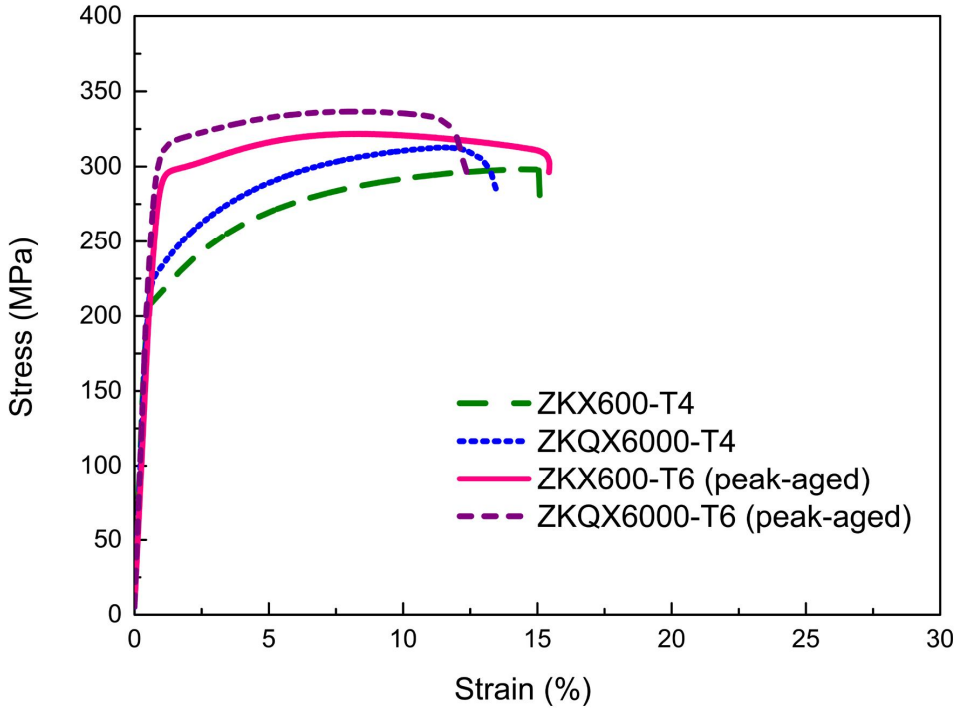

Figure 3: Tensile stress-strain curves of ZKX600 and ZKQX6000 at T4 condition (400ºC for 30min) and T6 (peak-aged) condition.

Figure 3 shows the tensile stress–strain curves of the ZKX600 and ZKQX6000 alloys in the T4 and peak-aged conditions. T4 treated ZKX600 and ZKQX6000 alloys show σ_{ys} of 210 MPa and 225 MPa with elongation to failure of 15.0% and 13.4%, respectively. Upon peak aging, σ_{ys} of ZKX600 alloy reaches 286 MPa, which is very close to that of the ZKQX6000 alloy, 300 MPa. The ZKX600 alloy also exhibits larger elongation to failure of 15.0% in comparison to ZKQX6000 alloy which shows 12.4% in the peak-aged condition.

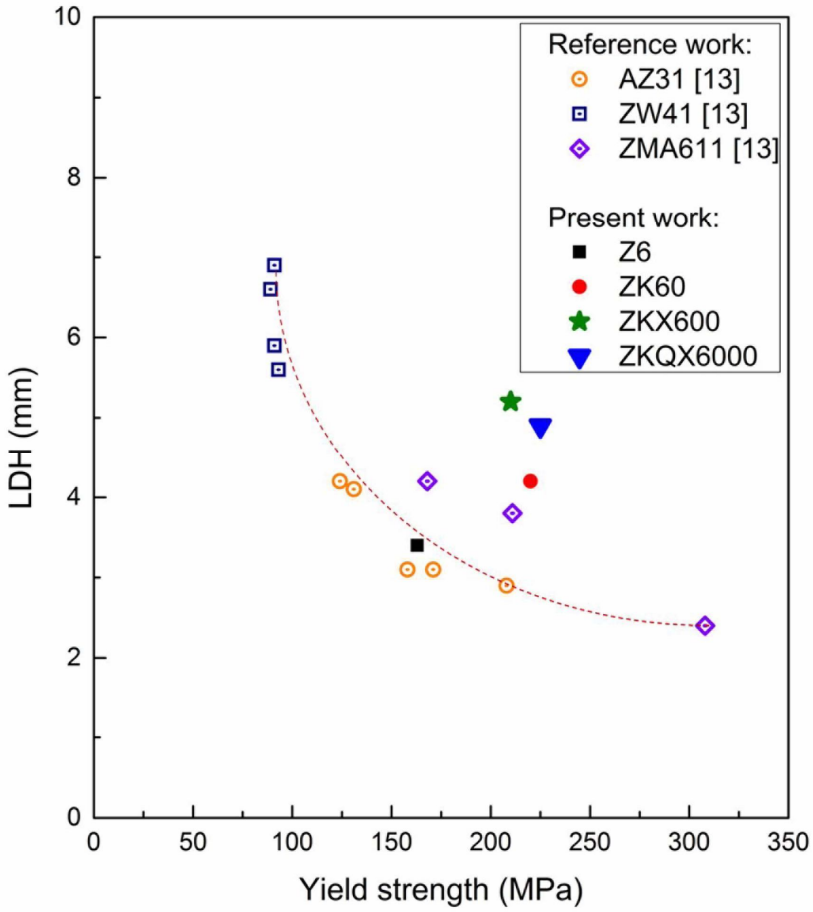

Figure 4: Plot of Erichsen cup tested LDH values as a function of tensile yield strength (T4 condition).

Figure 4 shows the LDH values measured by Erichsen cup test as a function of tensile yield strength (T4 condition). For comparison, the LDH values of other TRC and rolled Mg alloys are also shown [13]. Note that a larger punch diameter of 30 mm was used instead of 20 mm used in the present study for the Erichsen cup test in the reference [13]. The LDH values of Z6, ZK60, ZKX600 and ZKQX6000 alloys are 3.4, 4.2, 5.2 and 4.9 mm, respectively. While the LDH generally decreases with an increase in yield strength (Fig. 4), T4 treated ZK60, ZKX600 and ZKQX6000 alloys exhibits larger LDH values in spite of their higher strength in comparison to other TRC-HR alloys such as Mg-3Al-1Zn (AZ31) and Mg-6Zn-1Al-1Mn (ZMA611) alloys. Particularly, the ZKX600 alloy exhibits the highest LDH value among the alloys in the present study even without the addition of Ag.

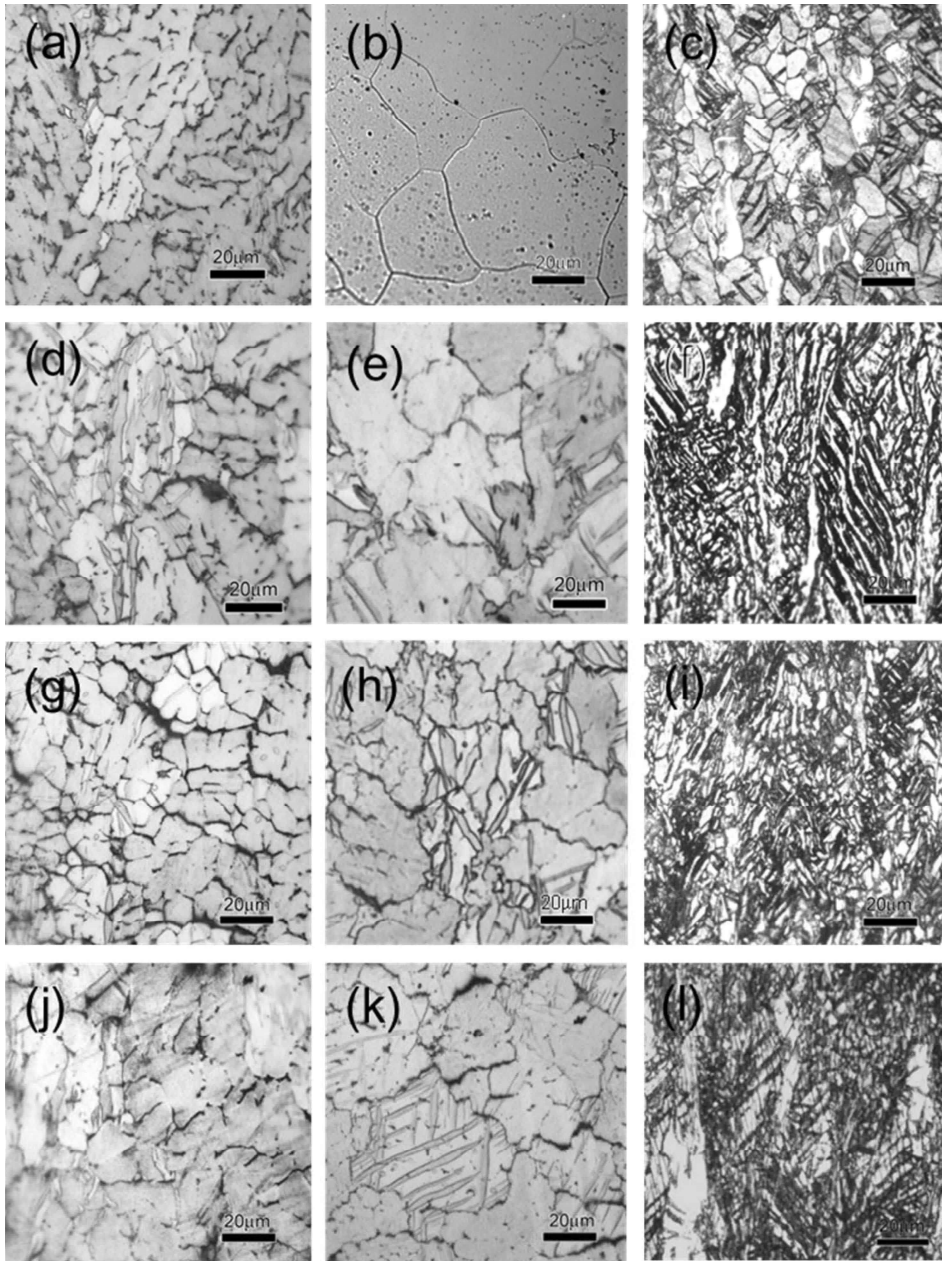

Figure 5: Optical micrographs of the alloys in various conditions; (a) As-TRC Z6, (b) homogenized Z6, (c) 3rd-pass- hot rolled Z6,(d) As-TRC ZK60, (e) homogenized ZK60, (f) 3rd-pass- hot rolled ZK60, (g) As-TRCZKX600, (h) homogenized ZKX600, (i) 3rd-pass- hot rolled ZKX600 (j) As-TRCZKQX6000, (k) homogenized ZKQX6000, (l) 3rd-pass- hot rolled ZKQX6000.

Figure 5 shows the optical microstructures of Z6, ZK60, ZKX600 and ZKX6000 alloys on cross sections perpendicular to the TD of the sheets. The as-TRC sheets of all the alloys have dendritic microstructure with twins in some grains (Fig. 5(a), (d), (g) and (j)). Upon homogenization treatment of Z6 alloy at 330ºC for 2h, the dendritic microstructure is broken completely and grains of ~50 μm size forms with no twins (Fig. 5(b)), whereas in ZK60, ZKX600 and ZKX6000 alloys, the dendritic structure is not broken completely and still twins could be observed in some of the grains (Fig. 5(e), (h) and (k)). After 3rd pass hot rolling there is reduction of grain size from around 50μm to ~20 μm in Z6 alloy. Most of the grains are dynamically recrystallized and some of them have twins inside them (Fig. 5(c)).ZK60, ZKX600 and ZKQX6000alloys show a mixture of fine recrystallized grains of around 1-4μm with elongated unrecrystallized grains of size greater than 20 μm containing twins (Fig. 5(f), (i) and (l)). Since there were more unrecrystallized regions in the ZK60, ZKX600 and ZKQX6000 alloys compared to Z6 alloy more twinning activity was observed in them.

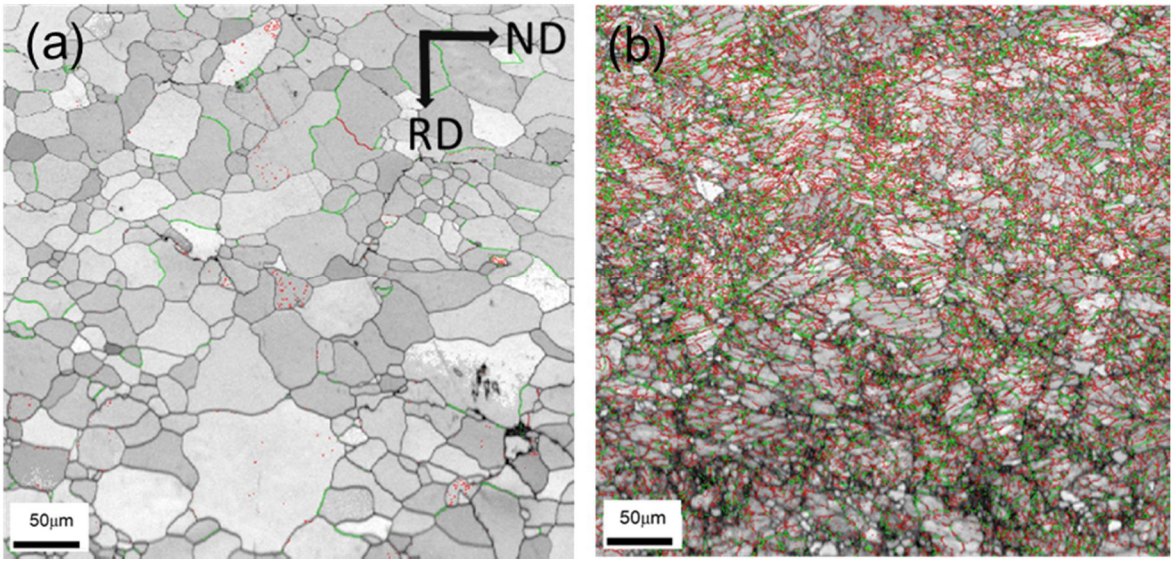

Figure 6: Image quality EBSD images of homogenized (a) Z6 and (b) ZK60 alloy showing misorientation boundaries below 15º. The red color and green color indicates the misorientations between 2-5º and 5-15º respectively.

Figure 6 shows the band contrast EBSD microstructure of Z6 (Fig. 6(a)) and ZK60 (Fig 6(b)) upon homogenization treatment at 330ºC for 2h. The red color line in the figure represents the boundaries having misorientation between 2-5º and green color represents the boundaries having misorientation between 5-15º. ZK60 alloy shows many low angle boundaries in the range of 2-15º compared to Z6 alloy. As per a recent theoretical study by Beyerlein et al it was shown that twin nucleation tends to be favored at low angle boundaries [14]. In the present study a greater twinning activity was observed in the Zr containing ZK60, ZKX600 and ZKQX6000 alloys compared to Z6 alloy after hot rolling. This could be related to higher number of low angle boundaries observed in the homogenized microstructure in the Zr containing alloys prior to hot rolling.

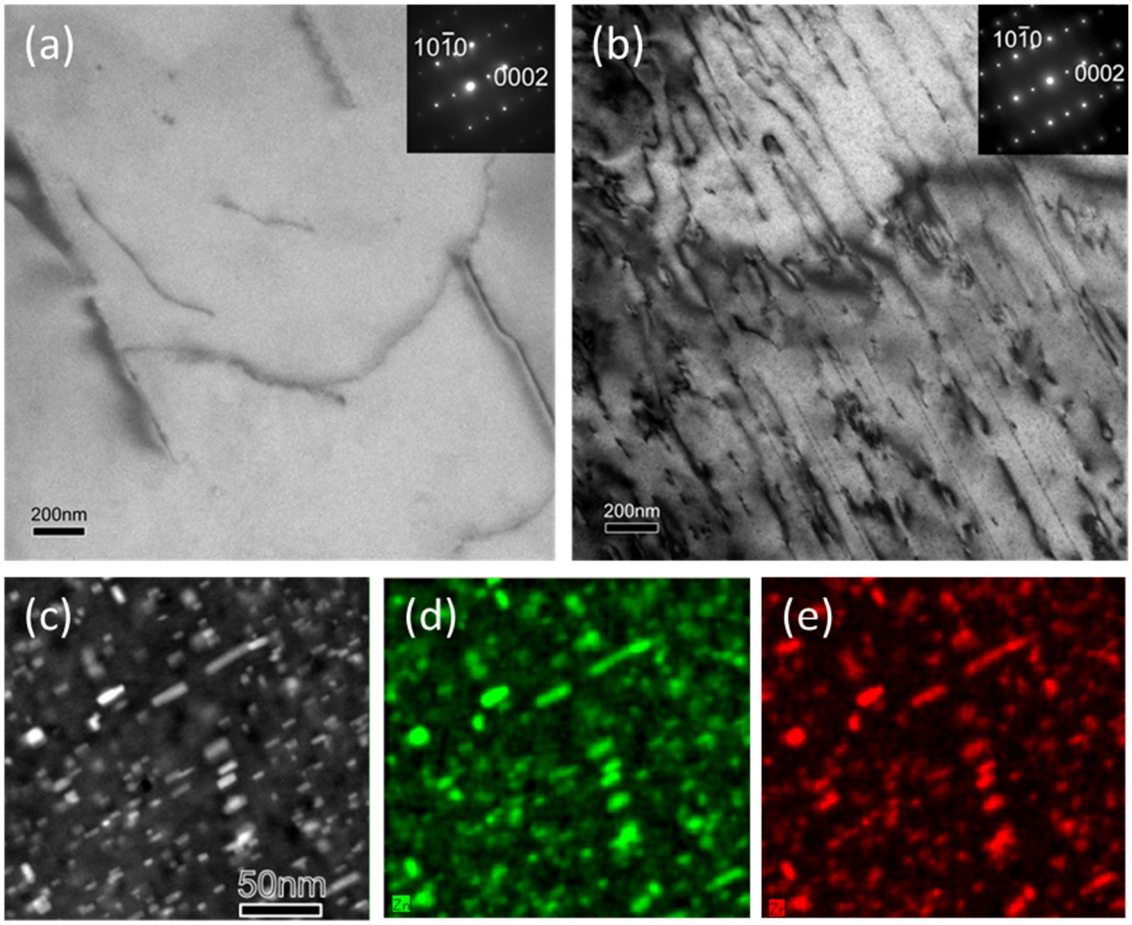

Figure 7: Bright field TEM images of homogenized (a) Z6 and (b) ZK60 alloy. (c) HAADF-STEM image of homogenized ZK60 alloy and corresponding EDS map of (d) Zn and (e) Zr. (Electron beam is approximately parallel to the <11$\bar{2}$0> direction).

The bright field TEM images of Z6 and ZK60 alloy homogenized at 330ºC for 2 h are shown in Figure 7 (a) and (b) respectively. The Z6 alloy had very few dislocations compared to ZK60 alloy which had a very high dislocation density. Another interesting feature of the ZK60 alloy is the presence of fine rod and plate like precipitates dispersed in the matrix. Figure 7(c) shows the high-angle annular dark-field (HAADF) scanning transmission electron microscopy (STEM) image of the fine precipitates found in ZK60 alloy. The precipitates have a size of 25 ± 21 nm in length and 8± 2 nm in width and are enriched with Zn and Zr as seen from the energy-dispersive X-ray spectroscopy (EDS) map of Zn (Fig. 7(d)) and Zr (Fig. 7(e)). Similar Mg(Zn,Zr) precipitates were also seen in our recent study on a heat treated ZK60 alloy [10].

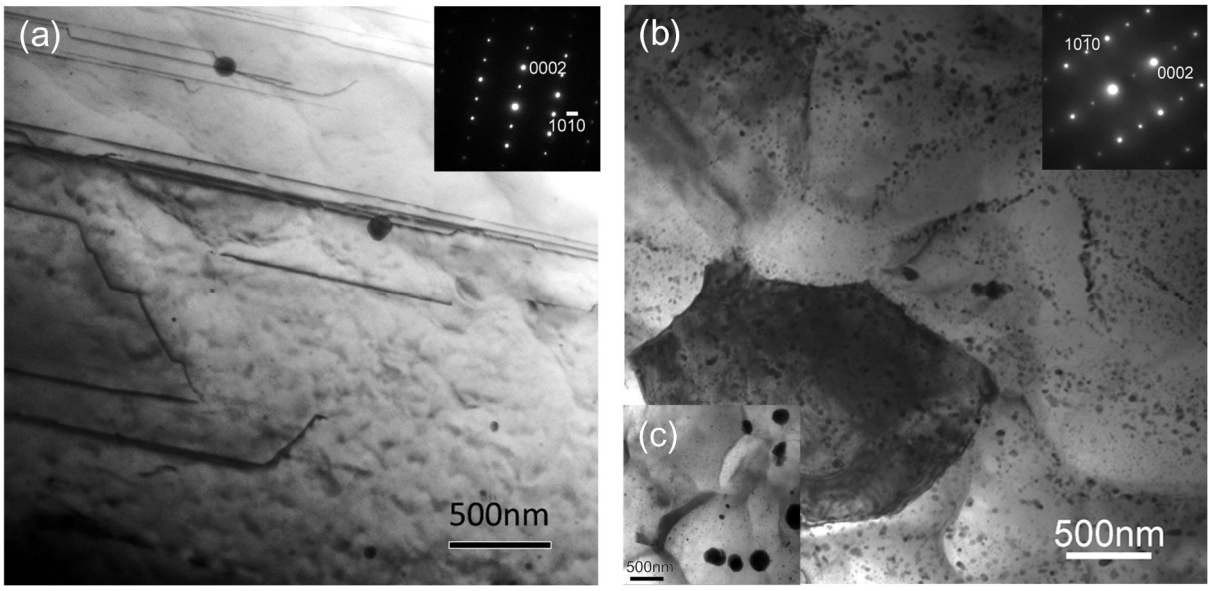

Figure 8: Bright field TEM images of homogenized (a) Z6 and (b) ZK60 alloy. (c) HAADF-STEM image of homogenized ZK60 alloy and corresponding EDS map of (d) Zn and (e) Zr. (Electron beam is approximately parallel to the <11$\bar{2}$0> direction).

The bright field TEM microstructure of the 3rd pass hot rolled Z6 alloy revealed few Mg-Zn particles of spherical shape with a size of ~100 nm (Fig. 8(a)), whereas the ZK60 alloy showed a very high density of fine spherical particles of Mg(Zn,Zr) of size ~25±20 nm distributed heterogeneously (Fig.8(b)) and a few large particles of size greater than 200 nm (Fig.8(c)). EDS analysis of the large particles showed a composition close to $Mg_7(Zn,Zr)_3$. The shapes of the fine Mg(Zn,Zr) particles becomes spherical upon hot

rolling as compared to their fine rod and plate like shape in the homogenized condition (Fig. 7(c)).

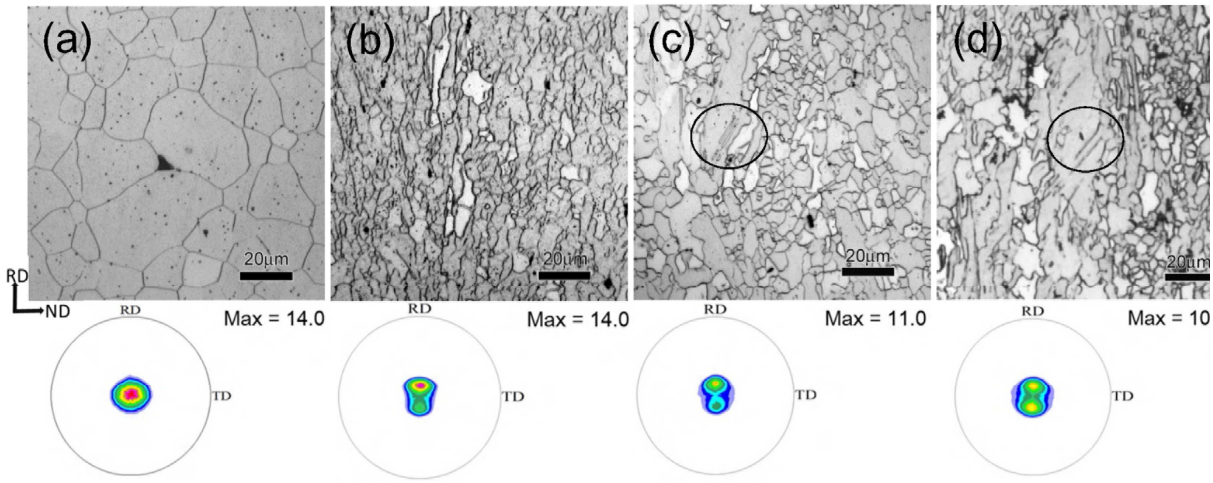

Figure 9: Optical microstructures with corresponding (0001) pole figures from the X-ray measurements of T4 condition (a) Z6, (b) ZK60, (c) ZKX600, (d) ZKQX6000 alloys.

Figures 9 (a-d) show the optical microstructures and (0001) X-ray pole figures of Z6, ZK60, ZKX600 and ZKQX6000 alloys in the T4 condition taken along the ND-RD plane. The Z6 alloy shows equiaxed recrystallized grains of 30.0 ± 10.0 μm with a strong basal texture in which the (0001) plane is parallel to the rolling plane (Fig. 9(a)). ZK60, ZKX600 and ZKQX6000 alloys show recrystallized grains of around 7.0 ± 3.0 μm in addition to the coarse unrecrystallized grains elongated along the rolling direction (Figs. 9(b-d)). The areal fraction of the unrecrystallized grains increases by the addition of Ag and Ca to the ZK60 alloy. The formation of twins within these grains as marked by black circles in Figures 9(c) and (d). Interestingly, the (0001) poles split along the RD in the ZK60, ZKX600 and ZKQX6000 alloys as shown in Fig. 9(b-d). The ZKX600 and ZKQX6000 alloys show relatively lower pole figure intensity compared to ZK60 alloy indicating weakening of the basal texture due to the additions of Ca and/or Ag.

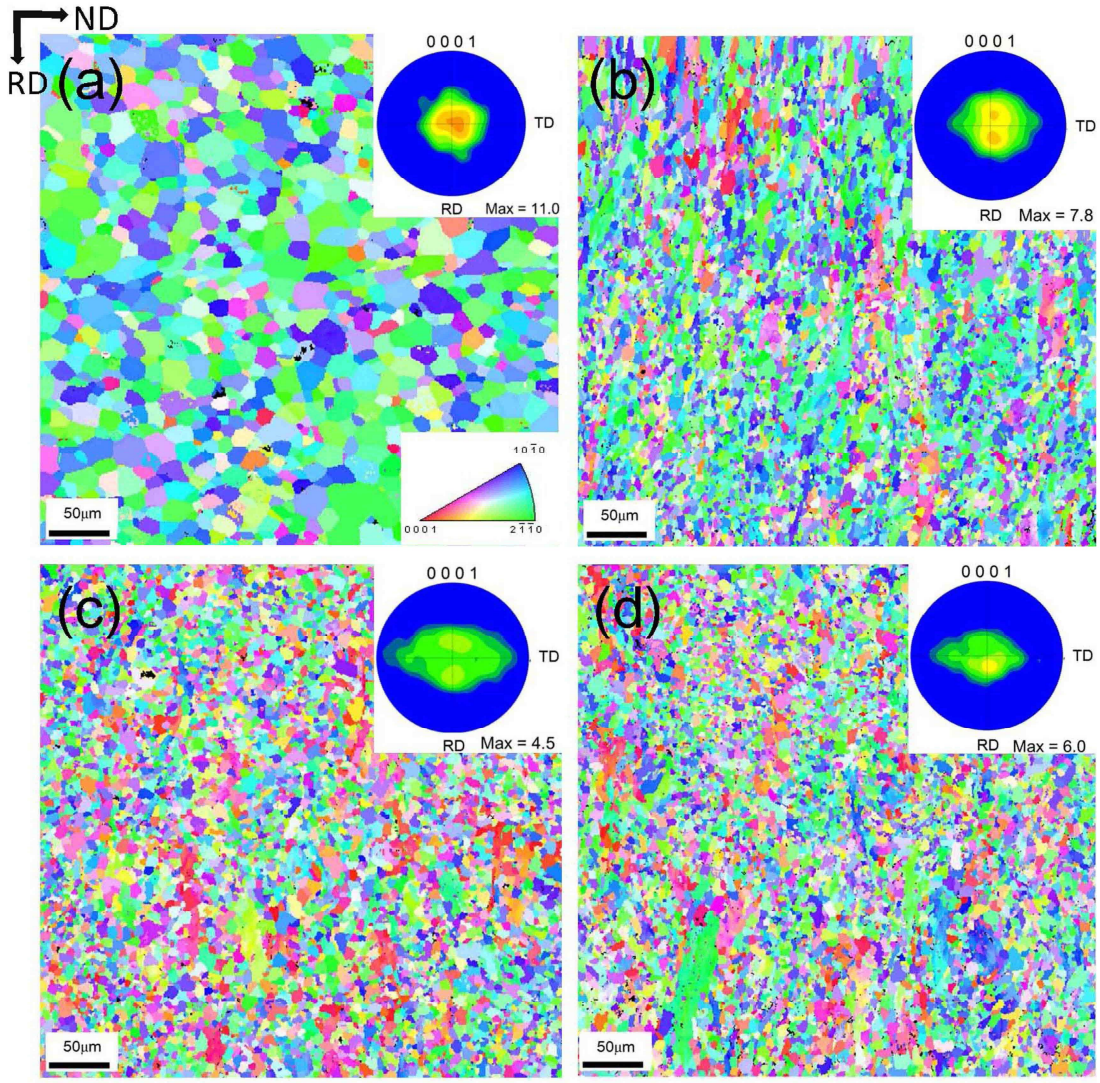

Figure 10: Inverse pole figure (IPF) map with EBSD (0001) pole figure of T4 condition (a) Z6 (b) ZK60 (c) ZKX600 (d) ZKQX6000 alloy.

Figure 10 (a-d) shows the inverse pole figure (IPF) map with EBSD pole figure from the (0001) plane of Z6, ZK60, ZKX600 and ZKQX6000 alloys after T4 treatment at 400ºC for 30 min. It shows that Z6 shows a strong basal texture (Fig. 10(a)). Upon addition of Zr to Z6 alloy, there is splitting of poles towards the RD and a slight decrease in the basal texture intensity (Fig. 10(b)) compared to Z6 alloy. The addition of Ca as well as combined addition of Ag and Ca to the ZK60 alloy causes further decrease in the basal texture intensity (Fig. 10(c), (d)). Thus there is good agreement in the trend shown by the pole figures of both the macrotexture and microtexture measurements done by X-ray and EBSD respectively.

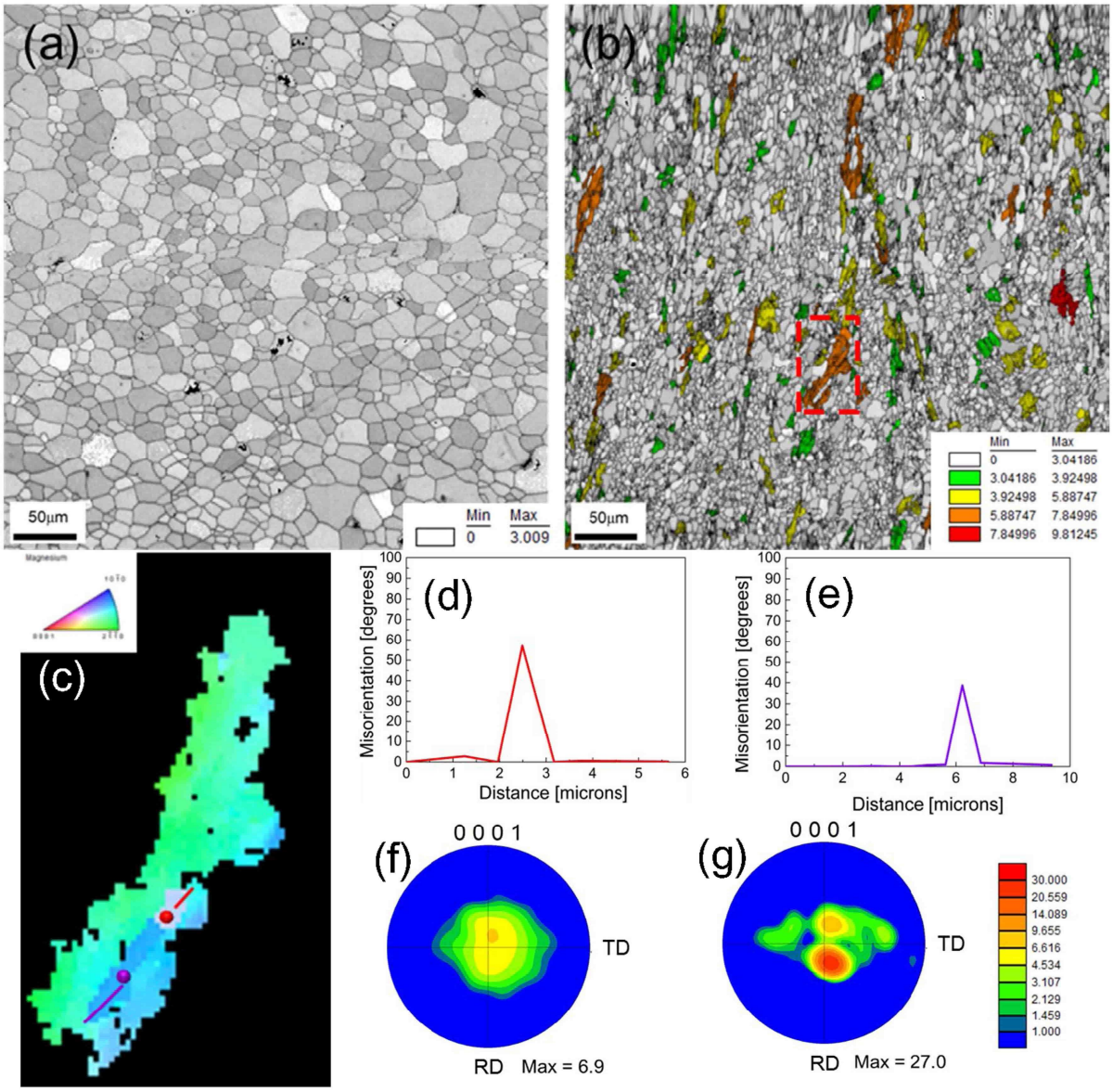

Figure 11: Image quality EBSD maps superimposed with grain orientation spread (GOS) map of T4 condition (a) Z6 and (b) ZK60 alloy, (c) IPF map of one of the representative unrecrystallized grain (marked by a red rectangle in (b)); (d) line profile of misorientation along the red line in (c) representing compression twin; (e) line profile of misorientation along the violet line in (c) representing double twin; (f,g) (0001) EBSD pole figure of recrystallized grains and unrecrystallized grains of the T4 condition ZK60 alloy respectively.

Figure 11 shows the image quality EBSD maps superimposed with grain orientation spread (GOS) maps of T4-treated Z6 ((Fig. 11(a)) and ZK60 alloys ((Fig. 11(b)). The GOS parameter, defined as the average misorientation between all pixels within a grain, helps to distinguish the deformed regions and recrystallized regions present in the microstructure [15]. A high value of misorientation spread in the microstructure implies a high geometrically necessary dislocation (GND) content corresponding to deformed regions whereas the recrystallized regions are characterized by low dislocation content having lower values of orientation spread. In this work, we have used a GOS value of 3.0º to separate the recrystallized and unrecrystallized grains in the ZK60 alloy. This is because the Z6 alloy has equiaxed recrystallized grains with a GOS value of less than 3.0º ((Fig. 10(a)). Alvi et al. has shown that a GOS value of 3.0º is successful in distinguishing the recrystallized and unrecrystallized deformed grains [15]. In Figure 11 (b), the grains having a GOS value larger than 3.0 are shown in color (color coded as per GOS intensity levels). Based on the GOS analysis, it is seen that the ZK60 alloy has unrecrystallized grain regions up to 10% in areal fraction. Figure 11 (c) shows one of the representative unrecrystallized grains in ZK60 alloy (marked by red color rectangle in Fig. 9(b)). Upon misorientation angle analysis along the lines marked by red and violet color in Fig. 11 (c), a ~56º compression twin (Fig. 11(d)) and a ~38º double twin (Fig. 11(e)) are present in a region marked by a red color and a violet color circles, respectively in Figure 11(c). The EBSD (0001) pole figures of the recrystallized grains and unrecrystallized grains of ZK60 alloy are shown in Fig. 11(f) and (g), respectively. The recrystallized grains show a slight tilting of basal poles with maximum intensity along the RD whereas the unrecrystallized grains have a splitting in the poles along the RD which could be due to the presence of double twins. In a report by Kim et al. it has been shown that the splitting of basal poles towards the RD tends to be induced when deformation bands consists of double twins [16].

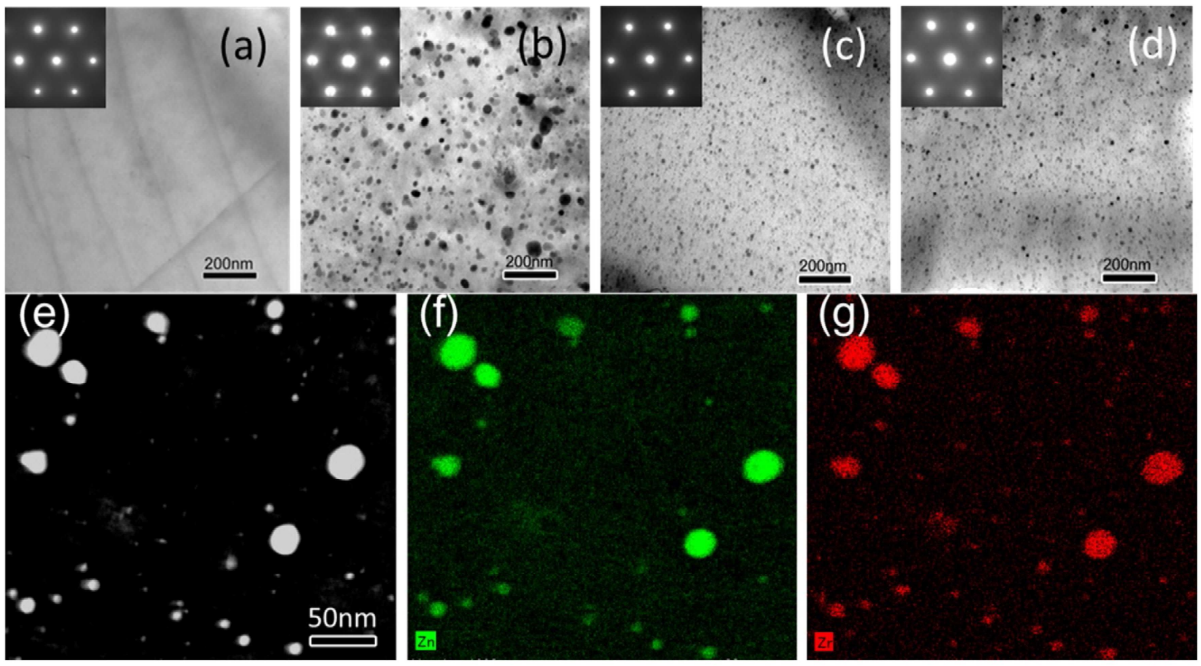

Figure 12: Bright field TEM images of T4 condition (400ºC for 30min) (a) Z6, (b) ZK60, (c) ZKX600, (d) ZKQX6000 alloy from the [0001] direction; (e) HAADF-STEM image of T4 condition ZK60 alloy and corresponding EDS map of (f) Zn and (g) Zr.

Figures 12 (a-d) show the bright field TEM images of Z6, ZK60, ZKX600 and ZKQX6000 alloys after T4 treatment. ZK60 alloy shows a dispersion of fine spherical precipitates of 25.0 ± 15.0 nm in size within the grains (Fig. 12(b)). However, the Z6 alloy does not show any fine spherical precipitates (Fig. 12(a)). Interestingly, the addition of Ca as well as combined additions of Ag and Ca to the ZK60 alloy further refines the size of the spherical precipitates to 12.0 ± 5.0 nm leading to an increase in the number density of precipitates (Figs. 12(c) and (d)). Figure 12(e) shows the high-angle annular dark-field scanning transmission electron microscopy (HAADF-STEM) image of T4 treated ZK60 alloy. The corresponding energy dispersive X-ray Spectroscopy (EDS) maps of Zn and Zr are shown in Figures 12(f) and (g), respectively. The fine precipitates are enriched with Zn and Zr. The absence of these precipitates in Z6 alloy (Fig. 12(a)) shows that addition of Zr promotes the formation of these fine Mg(Zn,Zr) precipitates in Zr containing alloys such as ZK60, ZKX600, and ZKQX6000.

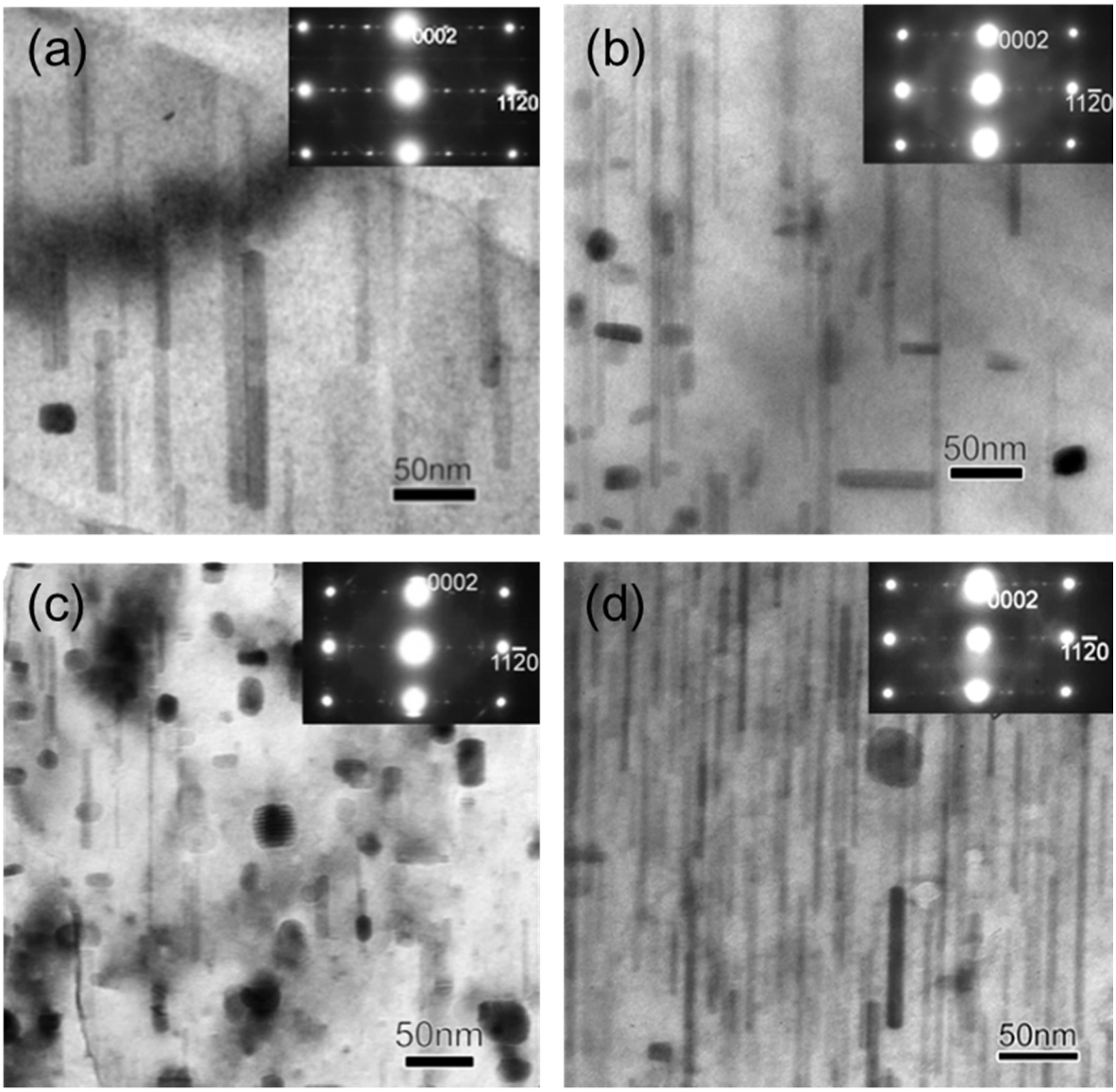

Figure 13: Bright field TEM images of peak-aged (a) Z6 (b) ZK60 (c) ZKX600 (d) ZKQX6000 alloy from the <10$\bar{1}$0> direction.

After peak aging (24 h) at 160°C, rod-like β'_1 precipitates and plate-like β'_2 precipitate are observed in all the alloys (Figs. 13(a-d)). The rod-like β'_1 precipitates grow along the [0001] direction (*c*-axis) of the matrix and the plate-like β'_2 precipitates lie on the (0001) plane of the matrix. The selected area electron diffraction (SAED) patterns indicate that the β'_1 precipitates have an orientation relationship of (0001) β'_1 //$(11\bar{2}0)_{Mg}$ and $[11\bar{2}0]\,\beta'_1$//$[0001]_{Mg}$ and the plate-like β'_2 precipitates have an orientation relationship of (0001) β'_2//$(0001)_{Mg}$ and $[11\bar{2}0]\,\beta'_2$//$[10\bar{1}0]_{Mg}$ as previously reported [9,17].

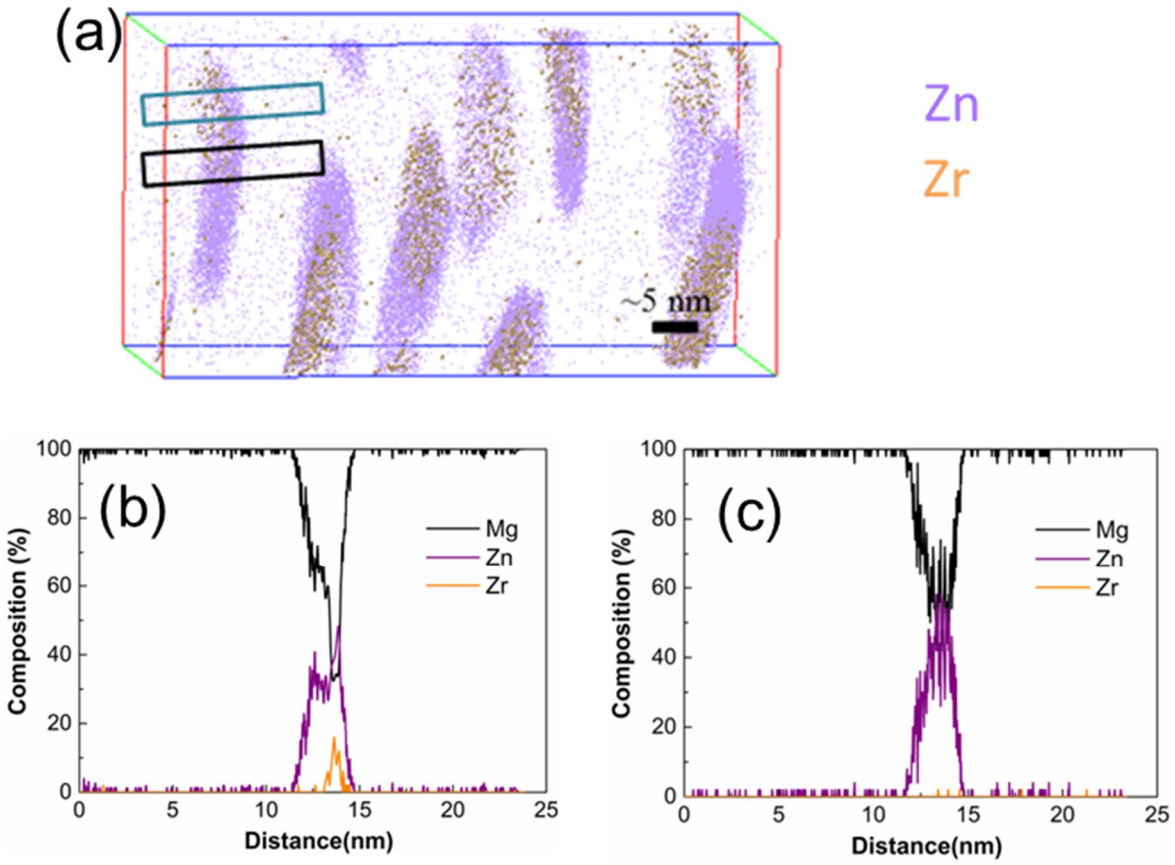

Figure 14: 3DAP map of peak-aged (a) ZK60 alloy; (b,c) the composition profile of the Zr- and Zn-rich regions of a selected β'_1-type precipitate indicated in (a) by a blue and black rectangle respectively.

Figure 14(a) shows the 3DAP map of peak-aged ZK60 alloy. It reveals that there is Zr-rich region at one of the ends of the β'_1 precipitates. The composition profiles of the Zr-rich and Zn-rich region of the precipitate marked by blue and black rectangles in Figure 14(a) are shown in Figures 14(b) and (c), respectively. The composition of the Zr-rich region is approximately Mg(Zn,Zr) and that of the Zn-rich region is ~MgZn. This indicates that the β'_1 precipitates grow along the [0001] direction from the Mg(Zn,Zr) precipitates present in the T4 condition. In our previous study of a peak-aged cast ZK60 alloy, we found similar results of Zr partitioning at one of the ends of the β'_1 precipitates [10].

5.4. Discussion

In this study, a comparative study of tensile properties and formability of TRC-HR Z6, ZK60, ZKX600 and ZKQX6000 alloys has been done by relating them with their respective microstructures and texture to understand the role of the microalloying elements.

5.4.1. Tensile properties and microstructure

As seen in Table 2, the addition of Zr to Z6 alloy causes an increment of more than 50 MPa in the tensile yield strength in the T4 condition. This can be attributed to the refinement of grain structure and the dispersion of the spherical Mg(Zn,Zr) precipitates. Watanabe et al., in their study on the effect of pre-strain on a ZK60 alloy reported that there is spheroidization of the precipitates on pre-straining [18]. In the present study, the spheroidization of the precipitates can also be attributed to the high amount of strain the sheets receive during the three-pass rolling to obtain the total reduction of 50%. By the addition of Ca and the combined additions of Ag and Ca to the ZK60 alloy, the Mg(Zn,Zr) precipitates are refined and their number density increases in the T4 condition (Figs. 12(c),(d)). The elongation to failure of the ZK60 alloy slightly decreases by the addition of Ca and Ag in the T4 condition probably because of the larger number of refined Mg(Zn,Zr) precipitates. The larger number of refined Mg(Zn,Zr) precipitates are more effective in retarding the recrystallization as seen from an increase in the areal fraction of the unrecrystallized regions of the ZKX600 and ZKQX6000 alloys than in the ZK60 alloy (Figs. 9(b-d)). Oh-ishi et al., in their study of an extruded Mg-6Zn-0.4Ag-0.2Ca-0.6Zr (wt.%) alloy, have also reported that the fine precipitates are effective for inhibiting dislocation motion and suppress the dynamic recrystallization leading to the formation of unrecrystallized coarse regions [9]. A recent study by Kim et al. on TRC-HR Mg-1Zn-1Ca and Mg-6Zn-1Ca (wt.%) alloys have reported tensile yield strengths of 154.9 MPa and 163.6 MPa respectively in their solution treated condition (T4) [19]. The present study shows tensile yield strength in the range of 210-225 MPa in the T4 condition in all the Zr containing alloys i.e., ZK60, ZKX600 and ZKQX6000. This shows that Zr is the principal element for the increment in yield strength.

Upon peak aging, among the four alloys studied in this work, the ZKQX6000 alloy shows the highest yield strength of 300 MPa followed by ZKX600 alloy which shows yield strength of ~290 MPa. The

increase in yield strength in ZKX600 and ZKQX6000 alloys is attributed to the refinement of β'_1 and β'_2 precipitates by Ca and Ag additions thus increasing the number density of precipitates [7,20]. Since the difference in the tensile yield strength between the Ag containing ZKQX6000 alloy and Ag-free ZKX600 alloy is only ~10MPa, the Ag-free ZKX600 alloy looks promising for industrial application.

5.4.2. Texture and formability

The addition of Zr to the binary Z6 alloy increases the LDH value from 3.4 to 4.2 mm. Comparison of XRD (0001) pole figures of T4 treated Z6 and ZK60 alloys shows that the Z6 alloy has a strong basal texture without any splitting tendency of the basal poles, whereas in ZK60 alloy basal poles shows tendency to split along the RD (Figs. 9(a), (b)). The splitting of basal poles along the RD in rolled magnesium alloys have been attributed to the formation of double twins in deformation bands and also due to operation of <c+a> slip [15,21]. Since double twin is observed in one of the unrecrystallized grains of ZK60 alloy (Fig. 6(e)), the splitting of basal poles along the RD in the present alloys is more likely to be as a result of double twinning. By the singular addition of Ca and the combined additions of Ag and Ca to the ZK60 alloy the LDH value further increases to 5.2 mm and 4.9 mm, respectively, from 4.2 mm. Thus the addition of Ca alone is sufficient for increasing the formability of the ZK60 alloy even without Ag. In a recent first-principles study by Yuasa et al., it was reported that plastic anisotropy tends to be reduced in Mg-Zn-Ca alloys due to the non-linear nature of the unstable stacking fault energy for the basal slip which gives rise to higher formability [22]. Experimental reports have also shown that the addition of Ca is beneficial for weakening texture and improvement in formability of binary Mg-Zn alloys [11,19,23]. The present work confirms that this is also the case for the ternary Mg-Zn-Zr alloys. Thus from the above results we can conclude that Ca is playing an important role in increasing the formability and that the addition of expensive Ag is not essential.

5.5. Summary

Twin roll cast and hot rolled Z6 alloys containing Zr, Ca, and Ag as microalloying elements shows tensile yield strength exceeding 300 MPa in the T6 (peak-aged) condition with reasonable formability in the T4 condition. The addition of Zr to the Z6 alloy stabilizes the fine Mg(Zn,Zr) particles which play a critical role in the recrystallization behavior. The addition of Ca to the ZK60 alloy is sufficient for weakening the basal texture and increasing the formability even without the addition of expensive Ag. Thus, the low-cost Ag-free ZKX600 alloy will be industrially promising as it shows equivalent mechanical properties to that of Ag-containing ZKQX6000 alloy.

Table 1. The nomenclatures and the nominal compositions of the alloys used in this work.

nomenclature	atomic %	mass %
Z6	Mg-2.4Zn-	Mg-6.2Zn
ZK60	Mg-2.4Zn-0.1Zr	Mg-6.2Zn-0.5Zr-
ZKX600	Mg-2.4Zn-0.1Zr-0.1Ca	Mg-6.2Zn-0.5Zr-0.2Ca
ZKQX6000	Mg-2.4Zn-0.1Zr-0.1Ca-0.1Ag	Mg-6.2Zn-0.5Zr-0.2Ca-0.4Ag

Table 2. Tensile properties of the investigated alloys in T4 and T6 (peak-aged) condition.

Alloy	T4 (400°C-30 min)			T6 (peak-aged)		
	σ_{ys} (MPa)	σ_{uts} (MPa)	ε_f (%)	σ_{ys} (MPa)	σ_{uts} (MPa)	ε_f (%)
Z6	163	264	8.2	246	294	4.2
ZK60	220	305	24.0	270	316	17.0
ZKX600	210	300	15.0	286	321	15.0
ZKQX6000	225	312	13.4	300	336	12.4

5.6. References

1. J. Bohlen, M.R. Nürnberg, J.W. Senn, D. Letzig, S.R. Agnew, Acta Mater. 55 (2007) 2101-2112.
2. L. Sturkey, J.B. Clark, J. Inst. Met. 88 (1959-1960) 177-181.
3. J.B. Clark, Acta Metall. 13 (1965) 1281-1289.
4. E.O. Hall, J. Inst. Met. 96 (1968) 21-27.
5. G. Mima, Y. Tanaka, Trans. Jpn. Inst. Met. 12 (1971) 71-75.
6. C.L. Mendis, K. Oh-ishi, K. Hono, Scr. Mater. 57 (2007) 485-488.
7. C.L. Mendis, K. Oh-ishi, Y. Kawamura, T. Honma, S. Kamado, K. Hono, Acta Mater. 57 (2009) 749-760.
8. C.L. Mendis, J.H. Bae, N.J. Kim, K. Hono, Scr. Mater. 64 (2011) 335-338.
9. K. Oh-ishi, C.L. Mendis, T. Honma, S. Kamado, T. Ohkubo, K. Hono, Acta Mater. 57 (2009) 5593-5604.
10. T. Bhattacharjee, C.L. Mendis, T.T. Sasaki, T. Ohkubo, K. Hono, Scr. Mater. 67 (2012) 967-970.
11. J.Y. Lee, Y.S. Yun, B.C. Suh, N.J. Kim, W.T. Kim, D.H. Kim, J. Alloys Comp. 589 (2014) 240-246.
12. K. Hono, T. Ohkubo, Y.M. Chen, M. Kodzuka, K. Oh-ishi, H. Sepehri-Amin, F. Li, T. Kinno, S. Tomiya, Y. Kanitani, Ultramicroscopy 111 (2011) 576-583.
13. D.H. Kang, D.W. Kim, S. Kim, G.T. Bae, K.H. Kim, N.J. Kim, Scr. Mater. 61 (2009) 768-771.
14. I.J. Beyerlein, R.J. McCabe, C.N. Tome, J. Mech. Phys. Solids 59 (2011) 988-1003.
15. M.H. Alvi, S. Cheong, H. Weiland, A.D. Rollett, Mater. Sci. Forum 467-470 (2004) 357-362.
16. K.H. Kim, B.C. Suh, J.H. Bae, M.S. Shim, S. Kim, N.J. Kim, Scr. Mater. 63 (2010) 716-720.
17. J. Gallot, R. Graf, Comptes. Rendus. Acad. Sci. 261 (1965) 728-731.
18. H. Watanabe, K. Moriwaki, T. Mukai, T. Ohsuna, K. Hiraga, K. Higashi, Mater. Trans. 44 (2003) 775-781.
19. D.W. Kim, B.C. Suh, M.S. Shim, J.H. Bae, D.H. Kim, N.J. Kim, Metall. Mater. Trans. A 44 (2013) 2950-2961.
20. T. Bhattacharjee, C.L. Mendis, K. Oh-ishi, T. Ohkubo, K. Hono, Mater. Sci. Eng. A 575 (2013)

231-240.

21. R. Cottam, J. Robson, G. Lorimer, B. Davis, Mater. Sci. Eng. A 485 (2008) 375-382.
22. M. Yuasa, M. Hayashi, M. Mabuchi, Y. Chino, Acta Mater. 65 (2014) 207-214.
23. Y. Chino, T. Ueda, Y. Otomatsu, K. Sassa, X. Huang, K. Suzuki, M. Mabuchi, Mater. Trans. 52 (2011) 1477-1482.

Chapter 6. Summary and Conclusions

A brief summary of the works described in chapters 2-5 are described below:

Chapter 2: The effect of Ag and Ca additions on the age hardening response of Mg-Zn alloys

In this work, the effect of sole and combined additions of Ag and Ca in enhancing the age hardening response in a Mg-2.4Zn (at.%) alloy was studied by systematic microstructure investigations using transmission electron microscopy (TEM) and three dimensional atom probe (3DAP). In the early aging stage of a Mg-2.4Zn-0.1Ag-0.1Ca (at.%) alloy at 160°C, Zn-rich Guinier Preston (G.P.) zones form with Ag and Ca enrichment. Further aging lead to the formation of fine β'_1 precipitates with Ag and Ca enrichment. We confirmed that the G.P. zones do not form in the Mg-2.4Zn (at.%) binary alloy at 160ºC, but form after a prolonged aging at 70ºC. This suggests that the combined addition of Ag and Ca shifts the metastable solvus for the G.P. zones to a higher temperature, thereby making it possible to form G.P. zones even at the artificial aging temperature of 160°C. Since G.P. zones act as nucleation sites for the β'_1 precipitates, the peak-aged microstructure is refined substantially by the addition of Ag and Ca which causes the enhanced age hardening response.

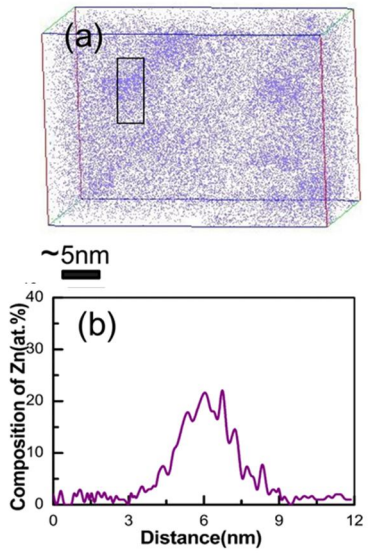

Fig 1. Figure 5: 3DAP map of Zn for the Z6 alloy aged at 70°C for (a) 100 h (b) the composition profile of Zn for the G.P. zone

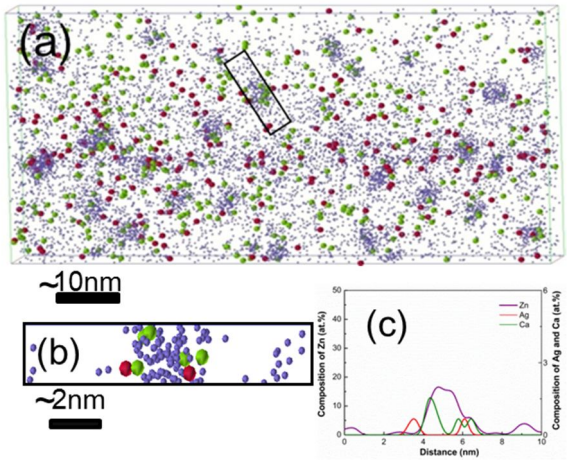

Fig. 2. 3DAP map of Zn, Ag and Ca for the ZQX600 alloy aged at 160°C for (a) 30 min (b) selected G.P. zone as marked in (a); (c) composition profile of Zn, Ag and Ca of the selected G.P. zone.

This work was done to characterize the nature of the fine precipitates that appear at a relatively high temperature (350°C), in a Mg-6.2Zn-0.6Zr (ZK60) alloy, to understand the nature of the precipitates that largely influence wrought microstructures. This work showed that the Zr in Mg alloys, along with its role as a grain refiner, has the additional role of stabilizing the metastable β'_1 $MgZn_2$ phase by forming the Mg(Zn,Zr) phase when heat treated at an elevated temperature. The present study confirmed that such fine precipitates formed at high temperature are a feature of the Mg-Zn-Zr ternary system. When the alloy is artificially aged at 160ºC, the β'_1-precipitate grows in the [0001] direction from the Mg(Zn,Zr) particles. The structure of the Mg(Zn,Zr) is exactly the same as that of β'_1, indicating that Zr partitioning occurs only at elevated temperature due to the sluggish diffusion of Zr.

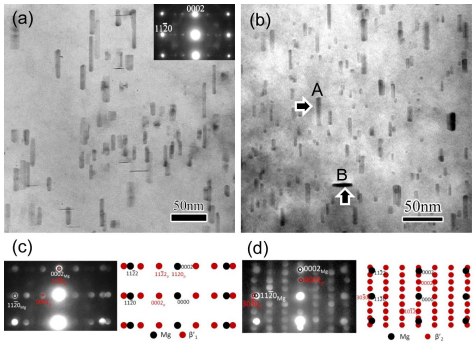

Fig. 3. TEM bright field image of the 350ºC heat treated ZK60 alloy for (a) 10 h and (b) 100 h from the <10$\bar{1}$0> direction; MBED and its simulated representation of (c) β'_1 precipitate and (d) β'_2 precipitate

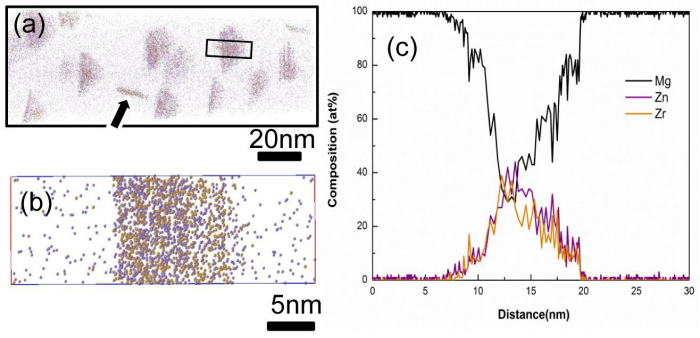

Fig. 4. 3DAP map of (a) 350ºC heat treated ZK60 alloy for 10 h (b) a selected section of a β'_1 type precipitate (c) composition profile of the the selected precipitate

Chapter 4: Effect of Zr on the microstructure and mechanical properties of an extruded Mg-Zn alloy

This work showed the effect of the Mg(Zn,Zr) precipitate on an extruded Mg-6.2Zn-0.6Zr (ZK60) alloy on its microstructure and mechanical properties by comparing it with an extruded binary Mg-6.2Zn (Z6) alloy. The results showed that the formation of fine Mg(Zn,Zr) precipitates play a critical role in dynamic recrystallization during extrusion by giving rise to the bimodal microstructure in ZK60 alloy which caused an increment of 92 MPa in tensile yield strength of ZK60 alloy compared to Z6 alloy in the extruded condition. The present extruded Z6 alloy showed a tensile yield strength of 162 MPa which is similar to the Zr-free Mg-6Zn-0.4Ag-0.2Ca alloy by Oh-ishi et al.[1] which had a tensile yield strength of 153 MPa. This result showed that addition of Ag and Ca without Zr to binary Mg-Zn alloy is not effective in increasing the as-extruded tensile yield strength. Once these Mg(Zn,Zr) precipitates are stabilized, only then the effect of Ca and Ag for the refinement of these precipitates is effective to further increase the strength of ZK60 alloy in the as-extruded condition. Thus this work showed that the addition of Zr to Mg-6.2Zn helps to attain a tensile yield strength of above 250 MPa when extruded by the stabilization of the β'_1-$MgZn_2$ precipitates. Upon peak aging of the ZK60 alloy at 160ºC for 72 h, the tensile yield strength could be further enhanced to 275MPa due to the increase in the aspect ratio of the β'_1 precipitates compared to the Mg(Zn,Zr) precipitates in the as-extruded condition.

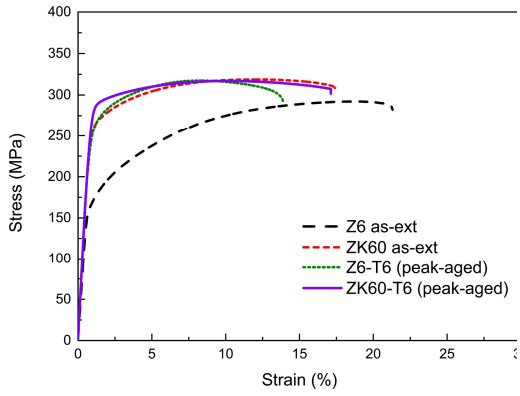

Fig. 5. Tensile stress-strain curves of Z6 and ZK60 in as-extruded condition and T6 (peak-aged) condition.

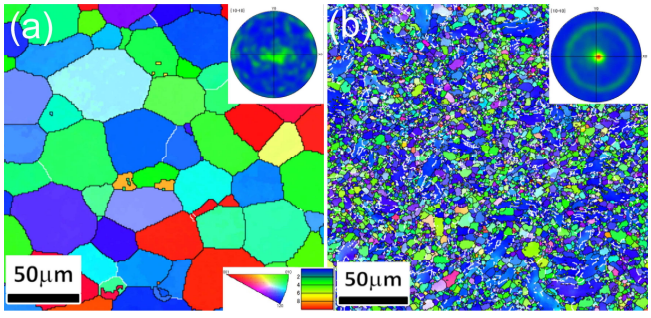

Fig. 6. EBSD map of as as-extruded (a) Z6 and (b) ZK60 alloy. The observed plane is normal to extrusion direction.

1. K Oh-ishi, CL Mendis, T Homma, S Kamado, T Ohkubo, K Hono, Acta Mater. 2009; 57: 5593.

Chapter 5: Effect of Zr, Ca and Ag on the mechanical properties and texture of twin roll cast- hot rolled Mg-Zn alloys

In this work we investigated the microstructure and mechanical properties of twin roll cast and hot rolled (TRC-HR) Mg-6.2Zn (wt.%) (Z6), Mg-6.2Zn-0.5Zr (wt.%) (ZK60), Mg-6.2Zn-0.5Zr-0.2Ca (wt.%) (ZKX600), and Mg-6.2Zn-0.2Ca-0.5Zr-0.4Ag (wt.%) (ZKQX6000) alloys in order to understand the effect of individual microalloying elements on the mechanical properties and texture of TRC-HR sheets. This work showed that TRC-HR Ag-free ZKX600 alloy showed tensile yield strength of 286 MPa in the T6 condition which is very close to that of Ag-containing ZKQX6000 alloy which showed a tensile yield strength of 300 MPa in the T6 condition. The formability of ZKX600 and ZKQX6000 alloy in the T4 condition also did not show any large variation. In summary, the addition of Zr to the TRC-HR Z6 alloy stabilizes the fine Mg(Zn,Zr) particles which play a critical role in the recrystallization behavior. This is similar to that seen in the extruded ZK60 alloy. Addition of Ca to the ZK60 alloy is sufficient for weakening the basal texture and increasing the formability even without the addition of expensive Ag. Thus this work showed that the low-cost Ag-free ZKX600 TRC-HR alloy is a promising low-cost high strength formable alloy for industrial applications.

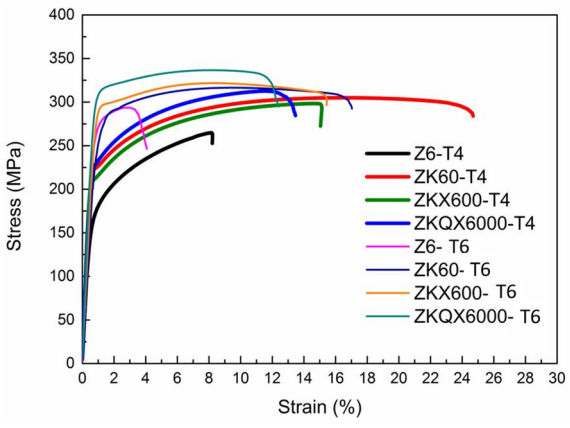

Fig. 7. Tensile stress-strain curves of Z6, ZK60, ZKX600 and ZKQX6000 at T4 condition (400ºC for 30min) and T6 (peak-aged) condition.

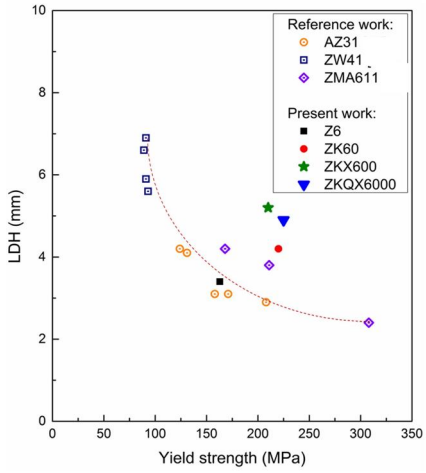

Fig.8. Plot of Erichsen cup tested LDH values as a function of tensile yield strength (T4 condition).

APPENDIX 1

Contingency table analysis

Contingency tables are used for determining the co-segregation and anti-segregation behaviour of the elements in a volume containing different phases. In other words this statistical analysis helps us to know whether there is tendency to cluster between elements or not for a given data set.

The contingency table can be regarded as a two-dimensional frequency distribution of elements. The correlation between two specified elements is determined by comparison of the the numbers of composition blocks containing high or low concentrations of two elements with those which are expected from a random distribution.

The general form of a two-dimensional *r*×*c* contingency table is shown in Table 1 shown below

Table 1 General form of a two-dimensional *r*×*c* contingency table [1]

		Experimentally observed values						Calculated Random values					
	Columns	(Variable B)						(Variable B)					
		0	1	*	c	Total		0	1	*	c	Total
Rows	0	n_{11}	n_{12}	*	n_{1c}	n_{1*}	0	e_{11}	e_{12}	*	e_{1c}	e_{1*}
Variable A	1	n_{21}	n_{22}	*	n_{2c}	n_{2*}	1	e_{21}	e_{22}	*	e_{2c}	e_{2*}
	*	*	*	*	*	*	*	*	*	*	*	*
	r	n_{r1}	n_{r2}	*	n_{rc}	n_{r*}	r	e_{r1}	e_{r2}	*	e_{rc}	e_{r*}
	Total	n_{*1}	n_{*2}	*	n_{*c}	n_{**}	Total	e_{*1}	e_{*2}	*	e_{*c}	e_{**}

In this two part table, r is the number of rows and c is the number of columns. The first part contains the experimentally observed values of the number of blocks of data that contain specific numbers of A and B atoms and the second part contains the calculated random values. n_{ij} represents the number of observations in the i^{th} category of the row (first variable) and the j^{th} category of the column (second variable).

The random value estimates of the expected frequencies is given by [1], $e_{ij} = \frac{n_{i*} n_{*j}}{n_{**}}$,

n_{**} is the total number of observations. The row and column marginal totals are $n_{i*} = \sum_{j=0}^{c} n_{ij}$ and $n_{*j} = \sum_{r=0}^{r} n_{ij}$ respectively.

The X^2 statistic can be evaluated from the contingency table by the following equation [1]

$$X^2 = \sum_{i=0}^{r} \sum_{j=0}^{c} \frac{(n_{ij} - e_{ij})^2}{e_{ij}}$$

The test of null hypothesis, which tests whether there is tendency to segregation between atoms or not is done by comparison of the probability of the X^2 statistic with the tabulated values of the χ^2 distribution for a specified number of degrees of freedom.

Co-segregation or anti-segregation tendency is evaluated by comparing the experimental observed values and their estimated random values, as shown in Table 2. If the number of experimental observations is higher than their estimates in blocks that contain high A and high B contents then it suggests a co- segregation tendency between the two elements. The opposite behaviour indicates an anti-segregation tendency between the two elements [1].

Table 2. Table showing the (a) co-segregation and (b) anti-segregation tendency [1]

(a)	Co-segregation						(b)	Anti-segregation					
	Columns	(Variable B)						Columns	(Variable B)				
		0	1	2	3	4			0	1	2	3	4
Rows	0	+	+	-	-	-	Rows	0	-	-	+	+	+
Variable A	1	+	-	-	-	+	Variable A	1	-	+	+	+	-
	2	-	-	-	+	+		2	+	+	+	-	-
	3	-	-	+	+	-		3	+	+	-	-	+
	4	-	+	+	-	-		4	+	-	-	+	+

References

[1] MK Miller, Atom probe tomography, Kluwer Academic/Plenum Press, New York, NY, 2000